A Study on Signal Integrity Improvement and Common-Mode Noise Suppression of Differential Transmission Lines for High-Speed PCB Layout

March, 2020

Chenyu Wang

Graduate School of
Natural Science and Technology
(Doctoral Course)
OKAYAMA UNIVERSITY

A Study on Signal Integrity Improvement and Common-Mode Noise Suppression of Differential Transmission Lines for High-Speed PCB Layout

Printed in Japan

Abstract

Electromagnetic devices have experienced remarkable progress in terms of their high performance, multiple functions, downsizing, and light-weight trend. This progress has mainly been brought about by higher-speed processing, lower voltage operation, and higher component density in the printed circuit boards (PCBs). However, transmission lines design on PCBs will be one of the bottlenecks in today's Gbps transmission due to the effect of electromagnetic compatibility (EMC) and signal integrity (SI) issues.

This thesis focuses on the differential transmission lines commonly used in high-speed signal transmission on PCBs such as USB3.0 (5.0 Gbps), SATA3 (6.0 Gbps), and PCI Express Rev.3.0 (8.0 Gbps). Due to the demand for higher density and smaller size of the PCB, the differential transmission line, which should be originally symmetrical, becomes asymmetrical, causing deterioration of SI and generation of common-mode noise. This common-mode noise is one of the significant factors of electromagnetic interference (EMI). Therefore, this thesis solves the following problems that can occur in high-speed differential transmission lines.

(A) common-mode noise generated at a bend of the differential transmission lines.

(B) differential skew caused by different effective relative permittivity around each line of differential transmission lines.

(C) differential mode crosstalk between adjacent differential pairs.

The main objective of this thesis is to elucidate the mechanism of EMC and SI issues of (A), (B), and (C), and it is to propose a design of high SI and low common-mode noise transmission lines. The author believes that the knowledge obtained by solving these problems will be useful for PCB wiring design to realize next-generation high-speed transmission and high-density mounting.

Chapter 2 examines a tightly coupled asymmetric tapered tightly bend structure to reduce (A). That is a proposal from our research group, which adjusts the length of the asymmetric taper to compensate for the path difference at a bend of the differential transmission lines and suppress the common-mode noise generation from the differential-to-common mode conversion. This thesis (assuming as high-density wiring) proposed a tightly coupled asymmetrically tapered bend that limits the bend structure within the area of the conventional bend and its design methodology. First, a geometrical path difference of the asymmetric taper part was defined, the setting of the taper formation conditions and the calculation formula of the structural parameter was derived. Furthermore, by reducing the line width and line separation of the tightly coupled bend, the geometric path difference and the effective path difference were matched, and it was shown that the characteristics as designed were obtained. Then, using 3D electromagnetic simulation and measurement evaluated the 45 degree-angle bend formed based on our design methodology and found that the differential-to-common mode conversion was decreased by almost 20 dB and maintain its transmission characteristics compared to those of the conventional bend.

In Chapter 3, to reduce (B), a mesh ground structure that does not affect the differential skew and characteristic impedance of the differential line was investigated. In general, the angle between the differential lines and the meshed ground in a flexible printed circuit (FPC) board is 45° and the differential lines are placed symmetrically to the pattern of the meshed ground. When the design emphasizes symmetry in this manner, the interval between the adjacent differential transmission lines becomes dependent on the pitch of the meshed ground, making it difficult to set an arbitrary wiring interval, which results in lower packaging density. On the other hand, if this symmetry is ignored, the effect on a differential skew and characteristic impedance cannot be ignored. This thesis, first, focuses on the angle between the trace of the differential lines and the meshed ground plane and investigates the angle dependence of the differential skew, taking into account phase delay between two lines with propagation to find low differential skew at the angle other than 45°. A simple model was proposed for reducing the calculation time but is found to be able to evaluate the angle dependence of the differential skew at a similar accuracy to the 3D electromagnetic simulation. As a result, it is found that the differential skew does not depend on the position of the differential lines to the meshed ground and keeps a comparatively small value at the angle between 30° and 40°. And, the differential skew and characteristic impedance are not affected by the position of the differential transmission lines relative to the pattern of the meshed ground when the rotation angle is around 30° by measure for FPC test boards. As a result, it is found that the rotated meshed ground makes the phase difference between the two lines irregular at each mesh pitch to keep the differential skew small. Therefore, this thesis also proposed a randomly shifting mesh position, and the same effect also can be obtained.

In Chapter 4 examined the introduction of a periodic structure into both outsides of a differential pair to reduce (C). The effect of its crosstalk reduction was evaluated, and the reduction mechanism was clarified. Furthermore, by focusing only on the differential mode, the mechanism of crosstalk that occurs in adjacent differential pairs having the periodic structure is considered by combining mode analysis, multiconductor transmission line theory, and weak coupling theory. Specifically, to explain the differential mode crosstalk mechanism of a 5-conductor transmission line, the concept of the odd- and even-mode differential mode was introduced. The crosstalk theory of a 3-conductor coupled transmission line was applied to this, and the differential mode crosstalk between adjacent differential pairs was formulated. The validity of the formula was shown by comparing it with the results of a 3D electromagnetic simulation. Also, the mechanism of reducing the differential mode crosstalk of the periodic structure was investigated from the characteristic impedance, effective relative permittivity, and mode coupling of the even- the odd-mode in the differential modes. In the differential pair having two periodic structures, it was found that the effective relative permittivity of the even- and odd-mode could be matched, and as a result, far-end crosstalk could be reduced to 0 theoretically.

Finally, Chapter 5 concludes this thesis with a summary of the key points.

概要

電子機器は高性能，多機能，小型，軽量など様々な観点から開発が近年進められている．この開発の進展にはプリント回路基板 (Printed Circuit Boards : PCBs) における高速信号処理，低電圧動作，高密度実装が大いに貢献している．ただし，電磁環境両立性 (Electromagnetic Compatibility : EMC) と信号完全性 (Signal Integrity : SI) の問題により PCB 上の伝送線路は，Gbps 伝送のボトルネックの 1 つになっている．

本論文では，USB3.0 (5.0 Gbps)，SATA 3 (6.0 Gbps) と PCI Express Rev.3.0 (8.0 Gbps) など PCB 上の高速信号伝送で一般に用いられる差動伝送線路を対象とする．PCB への一層の高密度化や小型化の要求により本来対称であるべき差動伝送線路が非対称となり，SI の劣化やコモンモードノイズ発生が引き起こされる．このコモンモードノイズは，電磁干渉 (Electromagnetic Interference : EMI) の要因の 1 つである．したがって，本論文では，高速差動伝送線路において現実に起こりうる以下の問題の解決を行う．

(A) 差動伝送線路の屈曲部で生じるコモンモードノイズ．

(B) 差動伝送線路の各線が受ける実効比誘電率が異なるによって引き起こされる差動スキュー．

(C) 隣接する差動ペア間で生じるディファレンシャルモードクロストーク．

本論文の目的は,（A）,（B），および（C）における EMC および SI の問題のメカニズムを解明し，SI を維持しつつコモンモードノイズ発生の少ない伝送線路の構造を提案することである．これらの問題を解決することで得られた知見は次世代の高速伝送と高密度実装を実現する PCB の配線設計に役立つと考えている．

本論文は 5 章構成で第 2 章以降は以下の通りである．第 2 章では,（A）の低減を実現するため，非対称テーパ付密結合屈曲構造について検討している．これは我々の研究グループで提案したもので，非対称テーパの長さを調整することにより，差動線路の屈曲部で生じる経路差を補償することでディファレンシャルモードからコモンモードへのモード変換によるコモンモードノイズ発生を抑える．本論文では，高密度実装を前提に通常の屈曲部の範囲内に収める非対称テーパ付密結合屈曲構造とその設計方法を提案した．まず，非対称テーパ部の幾何的な経路差を定義し，テーパ形成条件の設定と構造パラメータ計算式の導出を行った．さらに，密結合屈曲部の線幅と線路間隔を減らすことにより，幾何的な経路差と実効的な経路差を一致させ，設計通りの特性が得られることを示した．そして，設計方法に基づいて形成した 45° の屈曲構造を評価し，通常の屈曲構造と比較して伝送特性は変わらず，ディファレンシャルモードからコモンモードへのモード変換が 20 dB 抑制できることを 3 次元電磁界シミュレーションと実測により示した．

第 3 章では，（B）を低減させるため，差動線路に対して差動スキューや特性インピーダンスに影響を与えないメッシュグラウンド構造を調べた．フレキシブルプリント回路 (Flexible Printed Circuit : FPC) 基板では通常，メッシュグラウンドを差動配線に対して 45° 回転し，その交差位置を差動配線の対称軸上に配置するが，このように対称性を重視すると，隣接差動配線の間隔はメッシュグラウンドのメッシュピッチに依存し，任意の配線間隔にすることが困難となり，実装密度を下げることにつながる．一方，この対称性を無視すると差動スキューや特性インピーダンスに与える影響が無視できない．本論文では，まず，差動配線とメッシュグラウンドのなす角度に着目し，45° ではない別の角度で差動スキューが低減するか，差動配線の 2 本の線路における伝搬に伴う位相変化量の差から差動スキューの角度依存性を調べた．その際計算量を減らす目的で簡易モデルを提案し，3 次元電磁界シミュレーションに近い精度で差動スキューの角度依存性の評価ができることを示した．そして，差動配線とメッシュグラウンドのなす角度を 30° と 40° の間にすることで，差動スキューが差動配線とメッシュグラウンドの位置にほとんど依存せず，その値も比較的小さくなることを明らかにした．また，角度を 30° にした試作基板により，差動配線に屈曲がある場合も差動スキューを小さくでき，特性インピーダンスの位置依存性もほとんどないことを確認した．そして，その低減メカニズムを調べたところと位相差をランダムにしたことに起因することが分かり，メッシュグラウンドを回転させるのではなく，メッシュ位置をランダムにシフトさせることでも同じ効果が得られることを示した．

第 4 章では，（C）の低減を実現するため，差動ペアの両方の外側への周期構造の導入を検討した．このクロストーク低減の効果を評価し，その低減メカニズムを明らかにした．さらに，ディファレンシャルモードのみに着目することで，周期構造を持つ隣接する差動ペアで発生するクロストークのメカニズムをモード解析，多導体伝送線路理論および弱結合理論を組み合わせて考察した．具体的は，5 導体伝送線路のディファレンシャルモードクロストークのメカニズムを説明するために，奇モードと偶モードのディファレンシャルモードの概念を導入し，3 導体結合伝送線路のクロストーク理論をこれにあてはめ，隣接差動ペア間のディファレンシャルモードクロストークを定式化した．3 次元電磁界シミュレーション結果と比較することで計算式の妥当性を示し，さらに，ディファレンシャルモードにおいて偶モードと奇モードの特性インピーダンス，実効比誘電率およびモード結合から周期構造のディファレンシャルモードクロストークの低減メカニズムを調べ，2 組の周期構造を持つ差動ペアでは，偶奇モードの実効比誘電率を一致させることができ，その結果遠端クロストークを理論的には 0 にできることを明らかにした．

最後に，第 5 章では，本研究で得られた知見をまとめた．

Acknowledgments

This thesis is a summary of my doctoral study in Electronic and Information Systems Engineering, Okayama University. I am grateful to a large number of people who have directly and indirectly helped me finish this work.

First of all, I would like to express my deep gratitude to Professor Yoshitaka Toyota, my supervisor, who has granted me the chance to start this research, and has given me innumerable advices and unrelenting encouragement. Thanks are extended to Professor Kazuhiro Uehara and Professor Kazuhiro Fujimori who have given me much precious guidance on the course of this research. I am also deeply grateful to Assistant Professor Kengo Iokibe for his significant comments, advices, and delightful discussions which inspired many of the ideas in this thesis. I am also indebted to Professor Yasuyuki Nogami for his helpful comments and great insight. My appreciation goes to Dr. Tetsushi Watanabe in Industrial Technology Center of Okayama Prefecture who gives me constructive opinions.

I am also grateful to all present and past members of Optical and Electromagnetic Waves Laboratory, Okayama University. I particularity thank the following members, who did much of the technical work and helped me overcome the difficulties encountered in my studies: Mr. Shohei Kan, Mr. Keita Takariki, Mr. Islam Md Ashraful, Mr. Hiroaki Takeda, Mr. Ryota Irishika, Mr. Yuhei Osaki. I also appreciate the excellent secretarial services provided by Ms. Midori Ohnishi and Ms. Yumiko Kurooka.

Finally, I would like to dedicate this thesis to my wife and my parents, Ms. Xin Guan, Ms. Yuhua Wang, and Mr. Dekuan Wang, in appreciation of their generous support and continuous encouragement.

Contents

List of Figures

List of Tables

Chapter 1

General Introduction

1.1 Background

Today, the progress of modern electronics technology plays a significant role in the industry and people's daily lives. Electronic products such as tablet PC and smartphones have experienced remarkable progress in terms of their high performance, multiple functions, downsizing, and light-weight trend. This progress has mainly been brought about by higher-speed processing, lower voltage operation, and higher component density in the printed circuit boards (PCBs). However, these trends are followed to increase the complexity and cost of trace layout and chip placement [1], and it should make serious considerations of electromagnetic compatibility (EMC) and signal integrity (SI) issues [2, 3].

EMC includes electromagnetic interference (EMI) and Electromagnetic Susceptibility (EMS). The so-called EMI, it is necessary to minimize undesirable electromagnetic radiated and conducted emissions from electronic devices that might affect other devices and the device itself. And, EMS, it is necessary to raise the ability of the electronic devices not to be affected by the surrounding electromagnetic environment in the process of performing due functions. At the same time, various organizations are actively formulating relevant regulations for regulation, such as the Voluntary Control Council for Interference by Information Technology Equipment (VCCI), the Federal Communications Commission (FCC), and the Comite European de Normalisation Electrotechnique (CENELEC), etc., which highlights the importance and urgency of EMC related issues.

SI refers to the quality of a signal transmitted between a driver and a receiver for the proper functioning of the circuit system. SI design has got significant development in recent years and grown into an area covering many critical aspects in high-speed digital circuit design, including signal propagation on transmission lines (loss, reflection, crosstalk, and skew, etc.), characterization of parasitics and discontinuities, power integrity (PI), and so on. However, with the continuous increase of signal propagation speed, frequency, and circuit density, as well as the decrease of electronic products form factor, and logic level, nowadays it is increasingly critical to ensure quality SI design for high-speed transmission. Otherwise, electronics may fail to function correctly.

Accordingly, EMC and SI become more and more important design factors in high-speed PCBs. In especial, in today's high-speed transmission lines in PCBs, are usually not electrically short anymore, and thus, need to be analyzed and designed using a multi-conductor transmission line theory [4, 5]. Effects previously considered to be negligible in low-speed transmission designs can become primary design issues with the increase of signal propagation speed, and the decrease of electronic products form factors, such as frequency-dependent losses, imbalance, and mode conversion, and so on. At the same time, high data bandwidth demand for next-generation high-performance computing (100+ Gbps), cloud communication/computing (50+ Gbps), and client devices (20+ Gbps) [6]. Transmission lines design on PCBs will be one of the bottlenecks to achieve such high data bandwidth.

1.2 Motivation

The differential signaling has become a popular choice in today's multigigabit transmission due to its high immunity to noise, low crosstalk, and low EMI conferred by its symmetrical properties. For example, PCI Express interfaces between boards inside the personal computer and SATA interfaces between the hard disk and the main-board, also, the display with HDMI, and other peripheral devices with USB, and so on. To support differential signaling in PCBs, the differential transmission lines are required. That is, concerning the PCB ground reference drive both signal traces, and differential signaling implies that signals in two signal traces with equal magnitudes with a 180° phase difference between the two, as shown in Fig. 1.1.

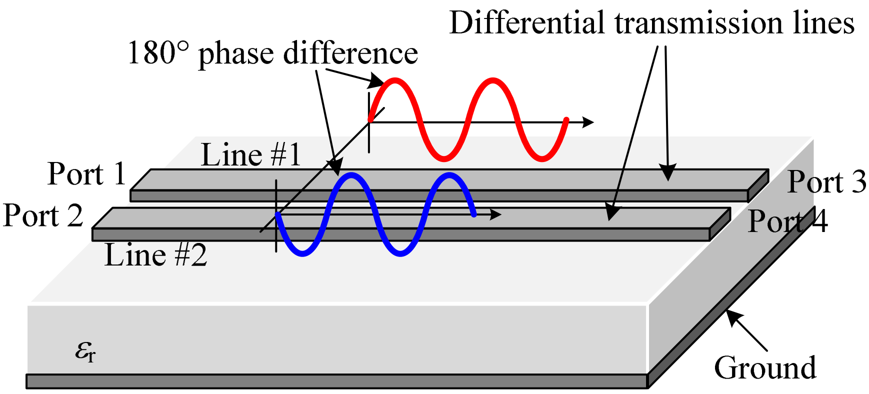

Figure 1.1 Symmetric differential transmission lines.

While differential transmission lines additional signal quality and allows longer traces to be used than the traditional single-ended transmission line [7, 8], as PCBs become increasingly dense and compact, the limited PCB space prevents symmetrical differential transmission line layouts, there are some EMC and SI issues that are not easily apparent [9–11]. A significant amount of common-mode noise can be created when the length of the two traces in the differential pair is slightly different, or the differential signals have small amounts of in-pair skew, or if the rise/fall times are somewhat different [12]. This common-mode noise is one of the significant factors of EMI [13–16]. Potential common-mode noise due to imperfect differential transmission lines layouts on PCBs could affect SI through mode conversion or crosstalk, as discussed earlier. Thus, these nonideal situations need to be carefully considered in high-speed differential signaling transmission. In this paper, we have studied the following nonideal situations:

(A) common-mode noise generated at a bend of the differential transmission lines.

(B) differential skew caused by different effective relative permittivity around each line of differential transmission lines.

(C) differential mode crosstalk between adjacent differential pairs.

The main objective of this thesis is to elucidate the mechanism of EMC and SI issues of (A), (B), and (C), and it is to propose a design of high SI and low common-mode noise transmission lines. If (A), (B), and (C) are ideally achieved, we believe that it is meaningful to design next-generation high-speed PCBs by utilizing the development and improvement of the high-speed signal transmission.

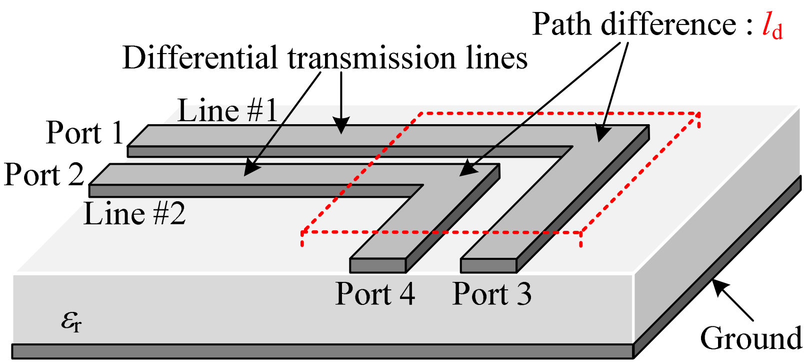

Figure 1.2 Differential transmission lines with bending discontinuity.

First, about issues of (A), as shown in Fig. 1.2 : Virtually every PCBs design will exhibit bends in some or all the transmission lines. The path difference l_d from the bend of the differential transmission lines causes the propagation time difference of time-domain transmission and the output phase difference will not exhibit ± 180° between Line #1 and Line #2, which leads to converts differential-mode signals into common-mode signals. That is known as differential-to-common mode conversion. This differential-to-common mode conversion can cause serious common-mode noise issues and degrade SI [17–21]. In [22–24], various common-mode suppression filters can be used to suppress induced common-mode noise of differential transmission lines. For example, the common-mode suppression filters with defected ground structures. However, defected ground structures can degrade the SI by causing discontinuities in the current return paths and degrade wiring density by their bulky size, also limited common-mode suppression bandwidth. Therefore, several researchers have proposed various techniques to suppress the differential-to-common mode conversion caused by bend on differential transmission lines without common-mode suppression filters. In [18], the compensation capacitance in an inner line of of the bent coupled lines was proposed by using a square patch for right-angle bends and a fan-shaped patch for 45-degree-angle bends to suppress the differential-to-common-mode conversion. In [25], the bend differential transmission lines using a compensation inductance is proposed to suppress the differential-to-common-mode conversion. The bend differential transmission lines using the compensation inductance can then be implemented by the bend differential transmission line using the short-circuited coupled line. Although capacitance and inductance compensation methods can effectively suppress the common-mode noise with proper adjusting capacitance and inductance values, the physical size of both capacitance and inductance structures in the bending area is too large, which led to and the reflection of an inner line will be increased obviously and wiring density deterioration. In [27,28], proposed bend differential transmission lines with the slow-wave structure. The slow-wave structures can reduce the phase velocity of the short inner line, thus decrease the propagation time difference with that of the long outer line. The surface mount device capacitor were used for compensation capacitance of the asymmetric coupled lines inner lines to reduce the common-mode noise [29]. Although the common-mode noise has a significant reduction with surface mount device capacitor compensation, yet the useful operating bandwidth of differential-to-common mode conversion and differential-mode transmission will be limited in the low-frequency band; also, vias and capacitors will increase the manufacturing cost. In [30–33], the differential transmission lines using a tightly coupled symmetrically tapered bend was proposed to suppress the differential-to-common mode conversion by decrease the path difference. Although the tightly coupled bend can suppress differential-to-common mode conversion by the tightly coupled bend shortens the path difference, but it always remains. Also, it has a higher differential-mode reflected compared with the case of the tightly coupled bend.

Next, about issues of (B) : There is known a problem with the differential skew, such as PCBs are generally constructed with various glass fibers saturated in epoxy resin. Since relative permittivity of the glass fibers is about 6 and relative permittivity of the epoxy resin is about 3, the distribution of the epoxy resin and the glass cloth around each differential transmission line causes a phase difference that leads to a differential skew, which leads to differential-to-common mode conversion. In high-speed signal transmissions, differential skew induced by the glass cloth is one of the important factors that cause the deterioration of signal quality [34, 35]. The glass cloth effects can be accurately modeled directly with 3D electromagnetic analysis by using a detailed description of weave geometry and resin filling as demonstrated in [36–40]. This approach is accurate when the geometry and composite material properties are properly defined. The periodic changes

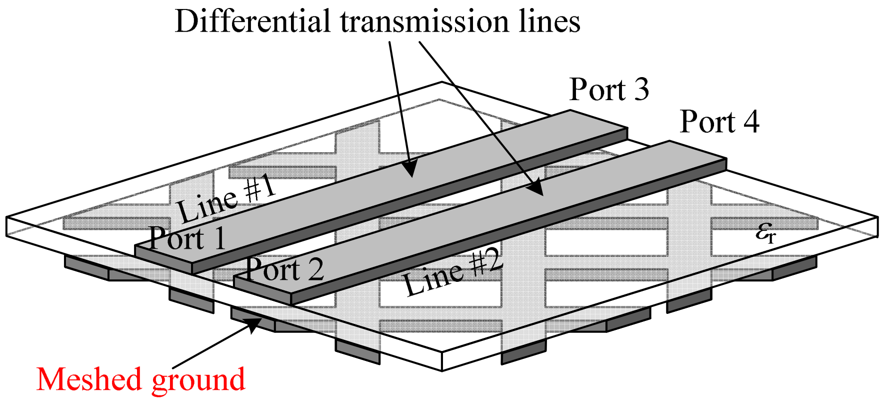

Figure 1.3 Asymmetry of differential transmission lines over a meshed ground plane in FPCs causes differential skew and characteristic impedance changes.

in dielectric properties along the line can be accounted for with concatenation of T-line segments with different parameters as suggested in [41] or by periodic loading of the transmission line model as done in [42]. However, these approaches have the process of geometry description laborious or analysis time is relatively long. Also, these approaches cannot be used for statistical analysis of interconnects running at different locations and angles concerning the fiber lattice. It has been reported that the differential skew is mitigated when the angle between the trace of the differential transmission lines and the thread of the glass cloth is around 10° [43]. To the author' best knowledge, the angle dependence between 10° and 45° and the optimum angle have not been investigated yet.

On the other hand, in recent years, flexible printed circuit (FPC) boards have been increasingly used in electronic devices as electronic devices become smaller and lighter. The dielectric of an FPC is very thin, and the characteristic impedance of its differential transmission lines is lower than the designated value, so the ground (i.e., the return path of the differential transmission lines) is formed into a mesh structure to increase the characteristic impedance without changing the line width, as shown in Fig. 1.3. In general, the meshed ground is rotated by 45° relative to the differential transmission lines. The ground is also arranged such that the intersection position of the meshes are on the axis of symmetry of the differential transmission lines [44, 45]. When the design emphasizes symmetry in this manner, the interval between the adjacent differential transmission lines becomes dependent on the pitch of the meshed ground, making it difficult to set an arbitrary wiring interval. Considering the characteristic impedance, it is necessary to make the mesh pitch rough to cope with the thinning of the dielectric, which results in lower packaging density. To improve the wiring density, the structure of the mesh must be changed; to do so, the wiring design of the lines must be redone first. Also, it is challenging to arrange the lines and the meshed ground completely symmetrically in actual production. If the two are even slightly asymmetrical, the characteristic impedance changes [46], causing mode conversion and differential skew [47]. The effect of line position on the effective characteristic impedance of a single-ended transmission line has been investigated in detail using full-wave simulation. When the angle between the wiring and the meshed ground (i.e., the rotation angle) is 0 or 45°, the characteristic impedance is heavily affected by the arrangement, but the effect is slight in the range of 10 to 40°, and around 22.5°, the effective characteristic impedance is unaffected by the wiring position [46]. However, To the author' best knowledge, when the differential transmission lines are wired on the mesh ground, the position dependency of the differential skew and the characteristic impedance have not been investigated yet.

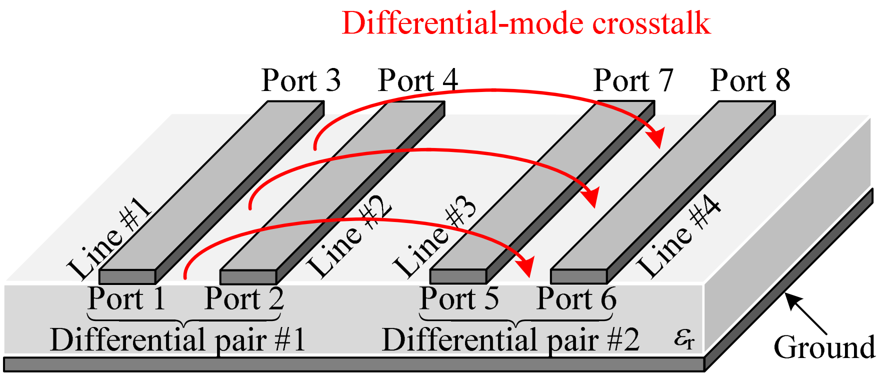

Figure 1.4 Differential-mode crosstalk between adjacent conventional differential pairs.

Finally, about issues of (C), as shown in Fig. 1.4 : In dense circuits, crosstalk is one of the most critical SI and EMI issues [11, 48, 49, 58] and has already become one of the dominant limiting factors for achieving a high-speed transmission. Theoretical and discussions for the crosstalk mechanism through the magnetic or electrical coupling have been well investigated [2,50–52]. Various approaches and design rules or recommendations have been explored in the literature and established to help reduce the effects of crosstalk between adjacent coupled lines so far [53–57]. However, there are few approaches and theories about suppressing differential-mode crosstalk between neighboring differential pairs so far. When more than two differential pairs run in parallel, a line is mainly coupled to the adjacent line because all the lines are parallel and in a fixed order. Accordingly, the two lines that constitute a differential pair are subjected to differential-mode crosstalk, which cannot be canceled out by differential signaling. As the spacing between two neighboring differential pairs is reduced and the rise times of digital signals become shorter, crosstalk becomes a more severe problem, strongly influencing the reliability and SI of the system. It generates additional delays, skews, jitters, or false switching of digital logic, degrading the noise margin and the timing margin of the system [11, 58]. In [59], putting a guard trace (guard trace should be necessarily via-grounded) between the adjacent differential pairs to help prevent or minimize the effects of crosstalk. However, these guard trace structures can reduce wiring density. Also, vias will increase the manufacturing cost. A twisted differential line structure was proposed in [60]. It is difficult to apply next-generation high-speed signal transmission because this structure is too complicated.

1.3 Outline

Figure 1.5 shows the flow of the discussion in this thesis, which is organized as follows.

Chapter 2 described a tightly coupled asymmetrically tapered bend to suppress common mode noise due to differential-to-common mode conversion caused by bend discontinuity in a pair of differential lines [61–64]. That is a proposal from our research group, which adjusts the length of the asymmetric taper to compensate for the path difference at a bend of the differential transmission lines and suppress the common-mode noise generation from the differential-to-common mode conversion. This thesis (assuming as high-density wiring) proposed a tightly coupled asymmetrically tapered bend that limits the bend structure within the area of the conventional bend and its design methodology. First, a geometrical path difference of the asymmetric taper part was defined, the setting of the taper formation conditions and the calculation formula of the structural parameter was derived. Furthermore, by reducing the line width and line separation of the tightly coupled bend, the geometric path difference and the effective path difference were matched, and it was shown that the characteristics as designed were obtained. We also using full-wave simulation and measurement evaluated the 45 degree-angle bend formed based on our design methodology and found that the methodology helps improve differential-to-common mode conversion and maintain its transmission characteristics compared to those of the conventional bend.

Chapter 3 described two mesh ground structures that do not affect the differential skew and characteristic impedance of the differential line. This thesis, first, focuses on the angle between the trace of the differential lines and the meshed ground plane and investigates the angle dependence of the differential skew, taking into account phase delay between two lines with propagation to find low differential skew at the angle other than 45°. A simple model [65, 66, 68] was proposed for reducing the calculation time but is found to be able to evaluate the angle dependence of the differential skew at a similar accuracy to the 3D electromagnetic simulation. As a result, it is found that the differential skew does not depend on the position of the differential lines to the meshed ground and keeps a comparatively small value at the angle between 30° and 40°. And, the differential skew and characteristic impedance are not affected by the position of the differential transmission lines relative to the pattern of the meshed ground when the rotation angle is around 30° by measure for FPC test boards. We also built two sets of FPC test boards. Our first set of test boards were built to examine differential skew, characteristic impedance, and transmission characteristics. Our second set of FPC test boards were built to evaluate the transmission characteristics of the differential transmission lines, including bending, to test the feasibility of high-density mounting. As a result, it is found that the rotated meshed ground makes the phase difference between the two lines irregular at each mesh pitch to keep the differential skew small. Therefore, this thesis also proposed a randomly shifting mesh position, and evaluate the differential skew and characteristic impedance by the different position of the differential transmission lines.

Chapter 4 described the achievement of crosstalk reduction by introducing a periodic structure into both outsides of a differential pair, and their propagation characteristics were evaluated [77, 78]. In this chapter, we focus only on the differential mode, and the mechanisms of crosstalk occurring in adjacent differential pairs with the periodic structure were investigated by combining modal analysis, multi-conductor transmission line theory, and the simplifying assumptions of weak coupling. For discussion differential-mode crosstalk of the 5-conductor transmission line, we proposed the concept of odd- and even-mode differential modes by referring to [58]. According to the classical coupled transmission line theory, we can use the approximate solution of [79, 80] and equate near- and far-end differential-mode crosstalk to the mixed-mode S parameters. From the formula of this thesis, near-end differential-mode crosstalk and far-end differential-mode crosstalk are analyzed. The author has also compared them with full-wave simulation results.

Chapter 5 concludes this thesis with a summary of the key points.

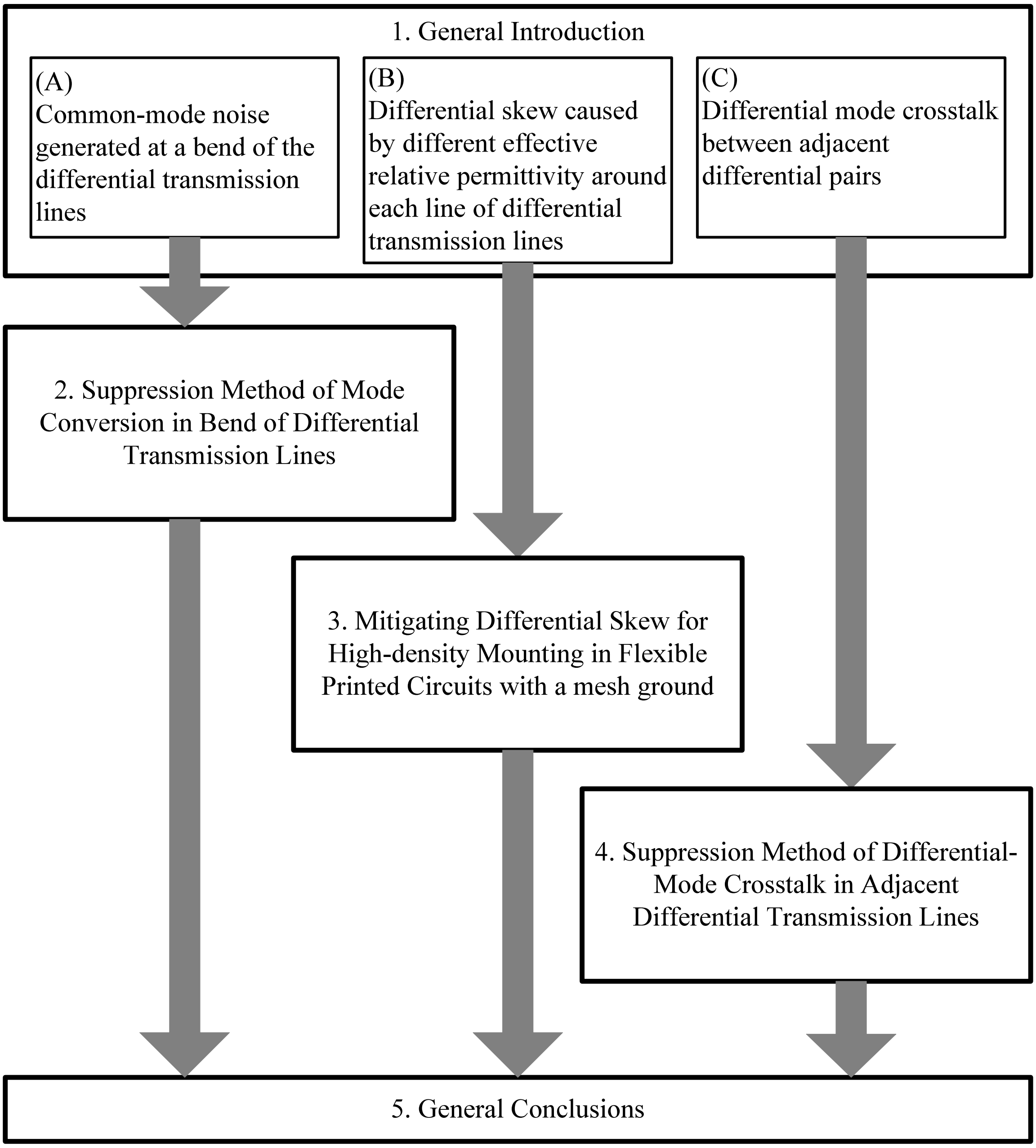

Figure 1.5 Chapter flows of this thesis

Chapter 2

Suppression Method of Mode Conversion in Bend of Differential Transmission Lines

2.1 Introduction

The differential signaling scheme has become required in high-speed digital systems due to its high immunity to noise, low crosstalk, and low EMI conferred, and it is generally used to high-speed interconnector interface, such as PCI Express, USB3.0, HDMI, and so on. For differential signaling on printed circuit boards (PCBs), a pair of coupled transmission lines are used. However, as PCBs become increasingly dense and compact, making symmetrical differential transmission line layout impossible in the limited PCBs space. For example, there can be a path difference between the inner and outer lines of differential transmission lines with asymmetrical layouts, such as those with bend discontinuities, as shown in Fig. 2.1(a). Thus, the output phase difference (in Ports 3 and 4) between Line #1 and Line #2 may not maintain a constant at 180°. The path difference causes mode conversion from the differential-to-common mode, and this conversion can cause serious common-mode noise issues and degrade signal integrity (SI) [6, 18]. In recent years, several researchers have proposed various methods to suppress the differential-to-common mode conversion caused by differential transmission lines bend structures. For example, the compensation capacitance in the inner line was proposed by using a square patch for right-angle bend, and a fan-shaped patch for 45-degree-angle bend [18], using the short-circuited coupled line for compensation inductance [25], using a slow-wave structure scheme [27, 28], the surface mount device capacitors were used for compensation capacitance of the asymmetric coupled lines inner lines [29], etc. These proposed structures can suppress the differential-to-common mode conversion. However, these bend structures have protruding structures reduced wiring density and larger differential-mode reflection than the conventional bend structure. As the progress of modern technology has led to an increasing tendency toward higher speed, high-density. Therefore, these proposed

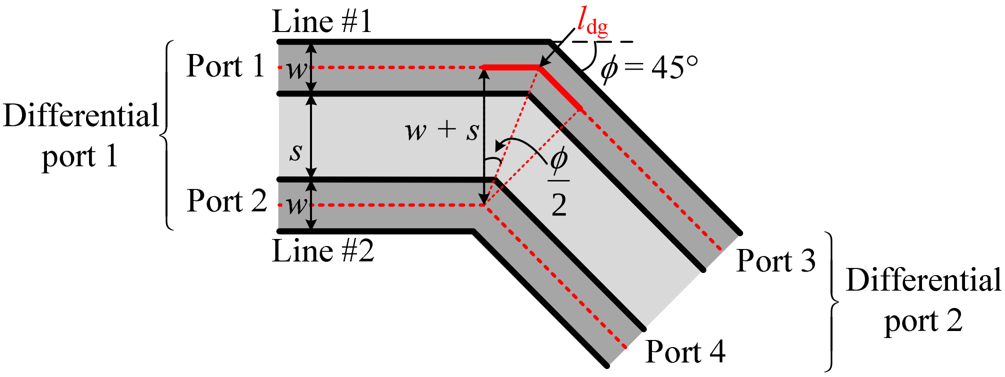

(a) Conventional bend

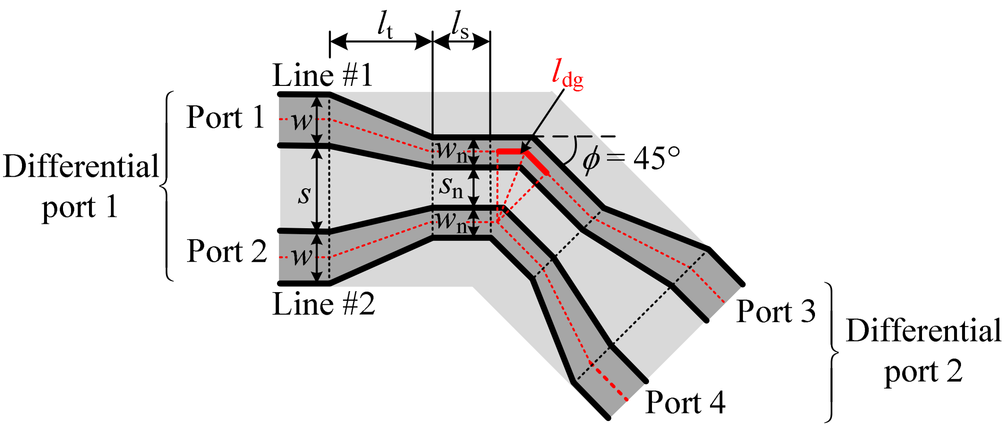

(b) Tightly coupled symmetrically tapered bend

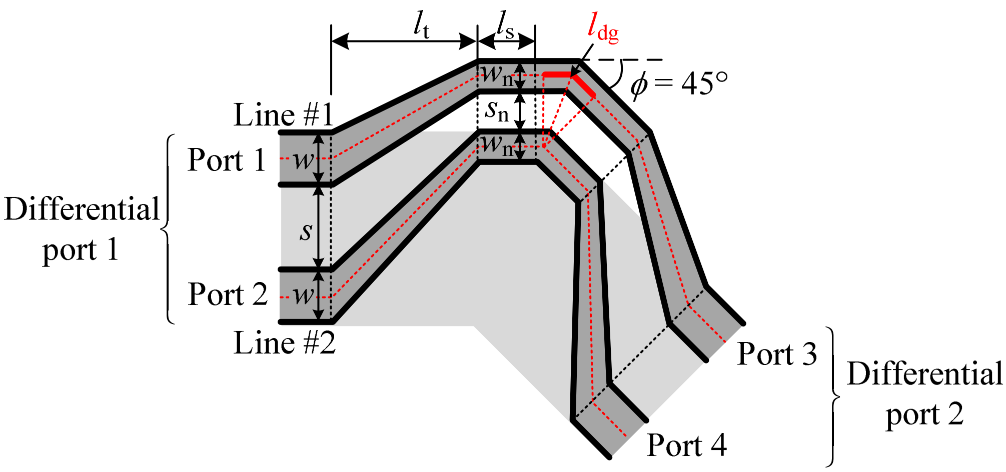

(c) Tightly coupled asymmetrically tapered bend

Figure 2.1 Conventional bend and previously proposed structures for reducing path difference..

structures are difficult to apply to the next generation of miniaturized high-speed PCBs.

In this thesis, we focus on suppressing the differential-to-common mode conversion by decrease the path difference. In keeping the differential-mode characteristic impedance

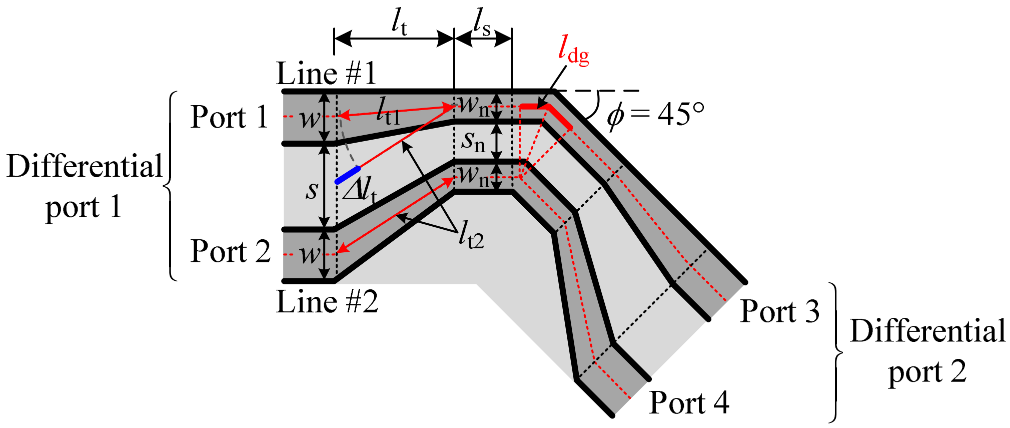

Figure 2.2 Tightly coupled asymmetrically tapered bend for high-density wiring treated in this thesis.

constant, tightly coupled differential transmission lines make the path difference shorter by decrease the linewidth and the line separation, while the narrow linewidth increases propagation loss due to the skin effect. In [30–33], a tightly coupled symmetrically tapered bend shown in Fig. 2.1(b) has been proposed to simultaneously realize lower propagation loss due to weakly coupled straight lines and lower differential-to-common mode conversion due to the tightly coupled bend area. However, the tightly coupled bend shortens the path difference, but it remains.

To compensate for the remaining path difference in the tightly coupled bend, we previously proposed a tightly coupled asymmetrically tapered bend to suppress the differential-to-common mode conversion [61,62], as shown in Fig. 2.1(c). The concept of the proposed bend is to compensate for the path difference remained in the bend by introducing the asymmetric tapers. As shown in Fig. 2.1(c), the total taper length of Line #1 is set shorter than that of Line #2, and the path difference of tightly coupled bend can be disappeared by adjusting the length of the asymmetrically tapered. However, the proposed bend structure was not limited within the area of the conventional bend, which also can degrade high-density wiring on PCBs. In [62], the geometrical path difference is substituted for the effective path difference. But in practice, an additional correction (the geometrical path difference set to a negative value [62]) is required to make the effective path difference vanish. In this chapter, we investigate the effective path difference vanishes by reducing the linewidth and the line separation in tightly coupled bend.

In this chapter, first, as shown in Fig. 2.2, the author proposes to suppress the differential-to-common mode conversion in 45-degree-angle bend by the tightly coupled asymmetrically tapered bend for high-density wiring in [63,64]. Next, we investigated the essential design methodology of our tightly coupled asymmetrically tapered bend to limit it within the area of the conventional bend as a light gray area (Fig. 2.2) and clarified its required constraint conditions. And, the relationship of the differential-to-common mode conversion with the effective path difference is discussed based on the results obtained from the full-wave simulation. Finally, the new bend structure formed based on our design methodology is evaluated using the results obtained by not only the full-wave simulation but also the measurement.

2.2 Mode Conversion Prediction Using Path Difference of Bend

This section, first, explains the parameters necessary for evaluating transmission characteristics and describes the relationship of the differential-to-common mode conversion with the effective path difference l_{d}. Next, we defined the geometrical path difference l_{dg} is substituted for the effective path difference l_{d} for facilitating this chapter discussion. Finally, the author explains the suppression method of the differential-to-common mode conversion using the proposed bend structure.

2.2.1 Differential-to-Common Mode Conversion

Scattering parameters (S parameters) greatly assist in the design, analysis, simulation, and measurement of the transmission lines. And, a mixed-mode S parameter makes it easier to analyze the differential transmission lines. We can by converting a single-

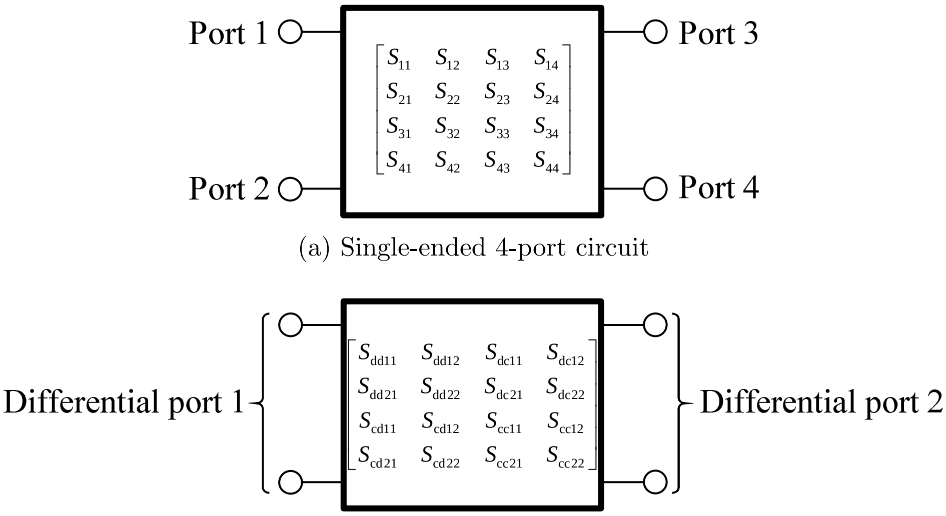

(a) Single-ended 4-port circuit

(b) Conceptual diagram of mixed-mode 2-port

Figure 2.3 Two ways to represent differential circuits.

ended four-port network (Fig 2.3(a)) into a differential two-port network (Fig 2.3(b)) via mixed-mode S parameters [73]. The response of a four-port network to common and differential input signals can be characterized using two-port mixed-mode S parameters. The single-ended ports 1 and 2 can be combined into a differential port 1 via mixed-mode S parameters. Also, the single-ended ports 3 and 4 can be combined into a further differential port 2 in the same way, and the corresponding differential and common-mode responses are measured on all of the ports. We analyzed the differential-mode propagation of bent differential transmission lines in terms:

- forward differential-to-common mode conversion (S_{cd21})
- backward differential-to-common mode conversion (S_{cd11})
- differential-mode reflection coefficient (S_{dd11})
- differential-mode transmission coefficient (S_{dd21})

This thesis focuses on analyzing that S_{cd21} because it occupies a dominant in the differential-to-common mode conversion. In mixed-mode S parameters, $|S_{\mathrm{cd21}}|$ can be expressed with single-ended four-port S parameters as follows:

$$|S_{\mathrm{cd21}}| = \frac{1}{2}|S_{31} - S_{24} + S_{41} - S_{32}|. \tag{2.1}$$

In Eq, (2.1), $|S_{31} - S_{42}|/2$ and $|S_{41} - S_{32}|/2$ correspond to mode conversion caused by the phase difference and the crosstalk, respectively. The magnitude of mode conversion due to the phase difference is dominant in $|S_{\mathrm{cd21}}|$ [62]. Therefore, we use the approximation, which usually holds for differential transmission lines, to simplify the calculation. $|S_{\mathrm{cd21}}|$ can be rewritten,

$$|S_{\mathrm{cd21}}| \cong \frac{1}{2}|S_{31} - S_{24}|. \tag{2.2}$$

Then, it is explained that the amount of differential-to-common mode conversion $|S_{\mathrm{cd21}}|$ greatly depends on the phase difference generated by the effective path difference l_{d} of the differential transmission lines. An equation that can easily give the mode conversion amount from l_{d}. In the bend structure shown in Fig. 2.1(a), Line #1 is longer than Line #2 by $l_{\mathrm{d}}/2$, and Line #2 is shorter than Line #1 by $l_{\mathrm{d}}/2$. Using the wave equation, each standard S parameter can be expressed by the following equation,

$$S_{31} = \exp\left[j\omega t - j\beta\left(l + \frac{l_{\mathrm{d}}}{2}\right)\right] \tag{2.3}$$

$$S_{42} = \exp\left[j\omega t - j\beta\left(l - \frac{l_{\mathrm{d}}}{2}\right)\right] \tag{2.4}$$

where β is wave number and given as $\beta = \omega\sqrt{\varepsilon_{\mathrm{reff}}}/c = 2\pi f\sqrt{\varepsilon_{\mathrm{reff}}}/c$, c is the speed of light.

Here, when Eqs, (2.3) and (2.4) are substituted into Eq. (2.2) and rearranged, the differential mode of the input port becomes the common mode of the output port. The amount of the forward differential-to-common mode conversion $|S_{\mathrm{cd21}}|$ is obtained assuming no propagation loss by the following derivation:

$$|S_{\mathrm{cd21}}| \cong \left|\sin\left(\frac{\pi\sqrt{\varepsilon_{\mathrm{reff}}}\,f\,l_{\mathrm{d}}}{c}\right)\right|. \tag{2.5}$$

Approximation in Eq, (2.5) is valid as long as $c/(\pi\sqrt{\varepsilon_{\mathrm{reff}}}) \ll f|l_{\mathrm{d}}|$ is satisfied. It is found from Eq, (2.5) that the differential-to-common-mode conversion is proportional to both frequency f and l_{d}.

2.2.2 Suppression Method of Mode Conversion using Proposed Bend

The $|S_{\mathrm{cd21}}|$ is strongly related to the effective path difference l_{d}, as can be seen from Eq, (2.5), but it is challenging to define apparently. In [62, 64], the geometrical path difference l_{dg} is substituted for the effective path difference for facilitating this chapter discussion. First, as shown in Figs. 2.1 and 2.2, the structural parameters of three different bend structures as following:

- w : line width
- s : separation between differential transmission lines
- w_{n} : line width of tightly coupled bend
- s_{n} : separation between differential transmission lines of tightly coupled bend
- l_{t} : taper length
- l_{t1} : taper's center-line length of Line #1
- l_{t2} : taper's center-line length of Line #2
- l_{s} : length of straight part between taper and tightly coupled bend
- l_{dg} : geometrical path difference
- $\mathit{\Delta} l_{\mathrm{t}}$: compensation amount

The geometrical path difference l_{dg} is defined as the subtraction of the center-line length of Line #1 from that of Line #2 as a red dashed line, and continue to use it in this paper. The figures also show the geometrical path difference of three types of bends depending on the bend angle ϕ. First, the geometrical path difference, which is represented as a short red solid line of the conventional bend shown in Fig. 2.1(a) is given as

$$l_{\mathrm{dg}} = 2(w+s)\tan\left(\frac{\phi}{2}\right). \tag{2.6}$$

Next, the geometrical path difference of the tightly coupled symmetrically tapered bend shown in Fig. 2.1(b) is given as

$$l_{\mathrm{dg}} = 2(s_{\mathrm{n}}+w_{\mathrm{n}})\tan\left(\frac{\phi}{2}\right). \tag{2.7}$$

When it has the bend angle ϕ in the same way as the conventional bend. Equation 2.7 indicates that the tightly coupled symmetrically tapered bend shortens the path difference because $w_n < w$ and $s_n < s$, but the path difference of $2(s_n + w_n)\tan(\phi/2)$ still remains.

Finally, our tightly coupled bend with asymmetric tapers shown in Fig. 2.2 has oblique tapers that can compensate for l_{dg} that remains in the tightly coupled symmetrically tapered bend. Extending the taper of Line #2 and shortening the taper of Line #1, therefore, results in the compensation amount $\Delta l_t = l_{t2}$ - l_{t1}, which is represented as a short blue solid line, where l_{t1} and l_{t2} are the taper's center-line lengths of Lines #1 and #2, respectively. Therefore, l_{dg} of our tightly coupled asymmetrically tapered bend shown in Fig. 2.2 is given as

$$l_{dg} = 2\left\{(w_n + s_n)\tan\left(\frac{\phi}{2}\right) - \Delta l_t\right\}. \tag{2.8}$$

Consequently, the total geometrical path difference vanish when the taper of Line #2 is longer by $2(s_n + w_n)\tan(\phi/2)$ than that of Line #1, that is, $\Delta l_t = 2(s_n + w_n)\tan(\phi/2)$.

Although we defined the geometrical path difference l_{dg} for each bend structure. However, the reader should be aware of the limitations of this geometrical path difference to realize when and if the structure parameters need to be revised.

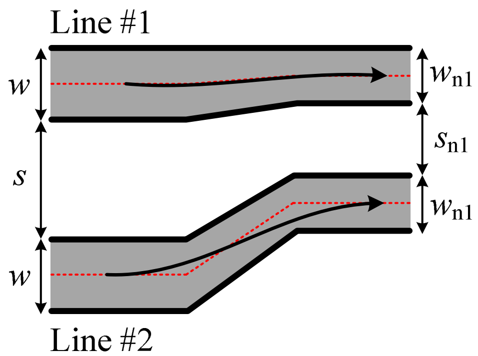

(a) Big difference

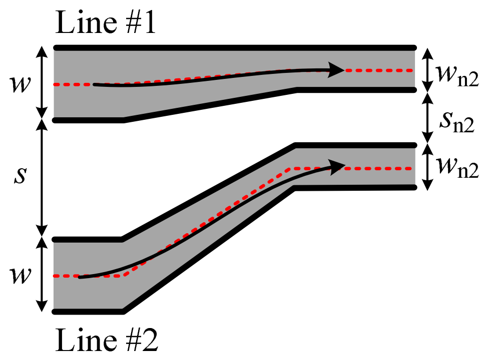

(b) Small difference

Figure 2.4 Geometric path and effective path ($w_{n2}<w_{n1}$, $s_{n2}<s_{n1}$).

There is one empirically conjectured effect that is worth noting. As shown in Fig. 2.2, we can easily observe that the degree of change in the taper part of Line #2 is more intense than that of Line #1. The signal flow in an asymmetrically tapered structure will flow in such a manner that they will deviate from the expected delay based on the center-line length. In Fig. 2.4(a), consider the arrow line, which might be a component of the signal. Since the signal cut both corners in the taper of Line #2, that component of the signal will arrive at the destination slightly earlier than expected, as described in [58]. So we know that in the differential transmission lines with asymmetrically tapered structure, the effective path difference may be slightly different than expected. And, this effect has been seen in the full-wave simulation and measurement [61–64]. Since our design methodology is based on the geometrical path length, in practice, an additional correction is required to make the effective path difference vanish.

To correction path difference of asymmetrically tapered to achieve equal Line #1 and Line #2 path length can be used l_{dg} of the tightly coupled asymmetrically tapered bend is set to a negative value. Thus the effective path difference l_{d} can disappear [61, 62]. However, the amount of this negative value is difficult to determine, and excessive compensation will lead to an increase in S_{cd21}. Therefore, while minimizing S_{cd21}, we also need to ensure that there is no excessive compensation to improve the efficiency of the design of the proposed bend structure.

As shown in Fig. 2.4(b), we can imagine that the signal flow in an asymmetrically tapered structure will flow in such a manner that they will close to the expected path (center-line length), when $w_{\mathrm{n2}} < w_{\mathrm{n1}}$ and $s_{\mathrm{n2}} < s_{\mathrm{n1}}$. Therefore, in this thesis, we reduce the difference between the geometric path difference and the effective path difference by reducing the line width w_{n} and line separation s_{n} of the tightly coupled bend, as described later.

2.3 Design Methodology of Proposed Bend for High-density Mounting

Figure 2.2 shows the tightly coupled asymmetrically tapered bend for high-density wiring treated in this chapter. In this section, we proposed the design methodology of our bend structure to limit it within the area of the conventional bend as a light gray area. Figure 2.5 shows our design methodology of the new bend structure for high-density wiring. By using this design flows, we can easily and quickly design our proposed structure, and this method is suitable for the wiring bend angles commonly used in PCBs design. It should be noted that our design method is based on the geometric path difference l_{dg} of 0.

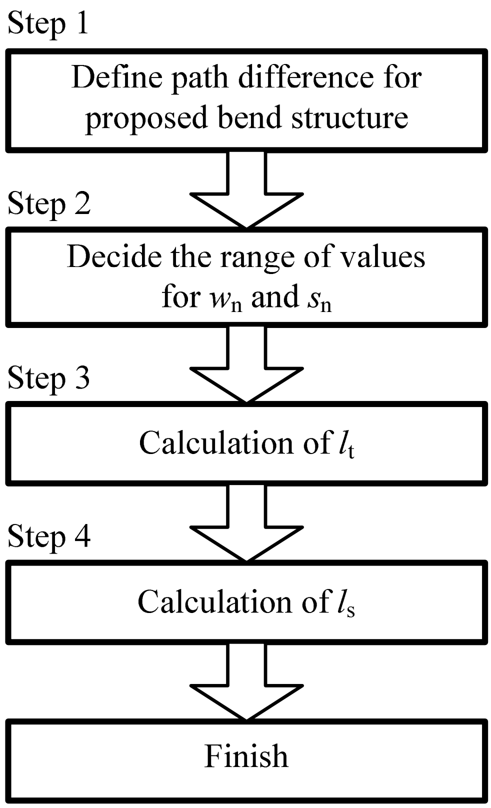

Figure 2.5 Design flows for tightly coupled asymmetrically tapered bend.

We defined geometrical path difference l_{dg} for the proposed bend structure in the previous section. Initially, l_{dg} is set to 0. Next, a range of values for w_{n} and s_{n} are defined when the geometrical path difference l_{dg} is 0. Although w_{n} and s_{n} are respectively different from w and s, it is possible and essential to maintaining the same value of differential-mode characteristic impedance as the line trace. In addition, we previous clarified that our bend structure could reduce the difference between the geometrical path difference l_{dg} and the effective path difference l_{d} by adjusting w_{n} and s_{n} of the tightly coupled bend.

Therefore, when designing the proposed structure, choose as small as possible w_n and s_n. Then, according to the determined w_n and s_n, we can obtain the computing method of the taper length l_t of the proposed bend structure to limit the bend within the area of the conventional bend. Finally, according to necessary constraint conditions of the length of the straight part l_s between taper and tightly coupled bend to set l_s, otherwise, it will have an adverse effect on S_{cd21}.

2.3.1 Range of Values for w_n and s_n

Figure 2.6 shows the asymmetrically tapered enlarged view of Fig. 2.2. Now, we describe our design methodology, which is determined geometrically from the bend structure. As shown in Fig. 2.6, l_a is the auxiliary condition for our design methodology, as

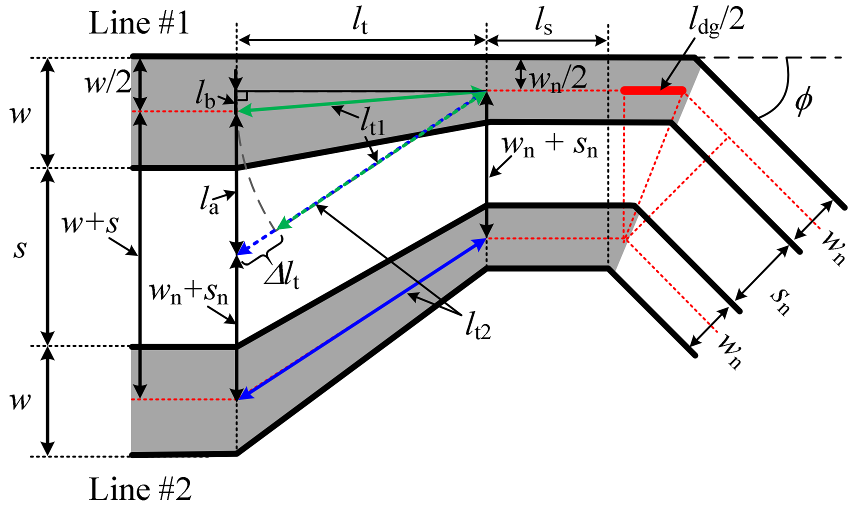

Figure 2.6 Asymmetrically tapered area enlarged the view of new bend structure.

follows

$$l_\mathrm{a} = (w + s) - (w_\mathrm{n} + s_\mathrm{n}), \tag{2.9}$$

and, Fig. 2.6 shows the case in which the outer side of Line #1 is just coincident with that of the conventional bend, l_b is a required constraint condition. l_b as follows

$$l_\mathrm{b} = \frac{w - w_\mathrm{n}}{2} \tag{2.10}$$

Next, a range of values for m_n and s_n are defined is explained when the geometrical path difference l_dg is 0.

In Fig. 2.6, there are three sides (l_t1, l_t2, and l_a) form a triangle. Thus, the length of one side must be greater than the difference between the lengths of the other two sides due to the conditions for the establishment of triangles, so the range that Δl_{t} can take is given by

$$\Delta l_{\mathrm{t}} < l_{\mathrm{a}} \tag{2.11}$$

Here, for asymmetric taper, $\Delta l_{\mathrm{t}}>0$.

Substituting $\Delta l_{\mathrm{t}} = l_{\mathrm{t2}}$ - l_{t1} and (2.9) into Eq. (2.11) get the following equation

$$(w_{\mathrm{n}} + s_{\mathrm{n}})\tan(\frac{\phi}{2}) - \frac{l_{\mathrm{dg}}}{2} < (w + s) - (w_{\mathrm{n}} + s_{\mathrm{n}}) \tag{2.12}$$

Here, the geometric path difference $l_{\mathrm{dg}} = 0$ is a condition, and from $w_{\mathrm{n}}>0$ and $s_{\mathrm{n}}>0$, the Eq. (2.12) can be rewritten

$$w_{\mathrm{n}} + s_{\mathrm{n}} < \frac{(w + s)}{1 + \tan(\frac{\phi}{2})} \tag{2.13}$$

Eq. (2.13) is a taper forming condition. In other words, to form a taper that the geometric path difference $l_{\mathrm{dg}} = 0$, the line width w_{n} and the line spacing s_{n} must satisfy Eq. (2.13). In addition, we previous clarified that our bend structure could reduce the difference between the geometrical path difference l_{dg} and the effective path difference l_{d} by adjusting w_{n} and s_{n} of the tightly coupled bend. Therefore, when designing the proposed structure, choose as small as possible w_{n} and s_{n}.

2.3.2 Taper Length l_{t} for Dense Traces

Here, as shown in Fig. 2.6, the calculation of the length l_{t} of the asymmetric taper when the case in which the outer side of Line #1 is just coincident with that of the conventional bend will be explained.

In Fig. 2.6, there are two right-angled triangles, one consisting of l_{t1}, l_{t}, and l_{b}, and the other consisting of l_{t2}, l_{t}, and (l_{a}+l_{b}). Therefore, there are the following formulas

$$l_{\mathrm{t1}}^2 = l_{\mathrm{t}}^2 + l_{\mathrm{b}}^2 \tag{2.14}$$

$$l_{\mathrm{t2}}^2 = l_{\mathrm{t}}^2 + (l_{\mathrm{a}} + l_{\mathrm{b}})^2 \tag{2.15}$$

Substituting Eqs. (2.9), (2.10), (2.14), and (2.15) into $\Delta l_{\mathrm{t}} = l_{\mathrm{t2}}$ - l_{t1} get the following equation

$$l_{\mathrm{t}} = \sqrt{\left[\frac{((w - w_{\mathrm{n}}) + (s - s_{\mathrm{n}}))(2(w - w_{\mathrm{n}}) + (s - s_{\mathrm{n}})) - \Delta l_{\mathrm{t}}^2}{2\Delta l_{\mathrm{t}}}\right]^2 - \frac{(w - w_{\mathrm{n}})^2}{4}}. \tag{2.16}$$

Using Eq. (2.16) to calculate l_{t} of the proposed structure can be it placed in the area of the conventional bend structure as not to affect the wiring density.

2.3.3 Straight Part l_s between Taper and Tightly Coupled Bend

In keeping the differential-mode characteristic impedance constant, make the path difference of bend area shorter by reducing linewidth and line separation and called the tightly coupled differential transmission lines, while the narrow linewidth and too long l_s increases propagation loss due to the skin effect [62]. However, in Fig. 2.7, too short l_s causes to increase the electromagnetic coupling of the taper area on Line #2 (as red arrows), which leads to new imbalance due to change of impedance and propagation constants. Thus, it leads to affect the suppress amount of S_{cd21} and differential-mode propagation characteristics of tightly coupled asymmetrically tapered bend. The most important thing in the design of l_s is to properly choose a l_p upon comprehensive consideration of the differential-to-common mode conversion and differential-mode propagation characteristics.

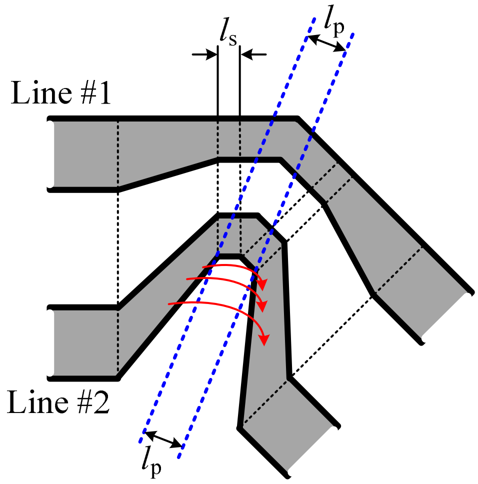

Figure 2.7 Imbalance caused by too small l_s.

For single-ended lines, the general guidelines expressed by the 3 w (line separation is 3 times the line width) rule are known because the crosstalk (electromagnetic coupling) can be made sufficiently small. In this paper, for simplicity, the length of the l_s does not adversely affect the differential-to-common mode conversion and the differential-mode propagation characteristics. Therefore, $l_p \geq 3w$ is the optimal condition here. Its effectiveness has been proved in [63]. There is room for consideration in the calculation of l_p adopted here. This is a topic for the future.

2.4 Evaluation of Mode Conversion in New Bend Structures

In this section, first, we were using our design methodology to determine the structural parameters of w_{n}, s_{n}, l_{t}, and l_{s}. And, these determined parameters used in Section 2.5 for the fabrication test board and measurement. Then, we validated the new bend structure formed based on our design methodology by full-wave simulation using a commercial simulator, ANSYS HFSS. And, this section discusses full-wave simulation results obtained under the assumption of no material loss, so that explains the impact of w_{n} and s_{n} on the forward differential-to-common mode conversion.

2.4.1 New Bend Structures Based on Proposed Methodology

The structural and electrical parameters are summarized in Table 2.1. The dielectric constant of the glass epoxy ε_{r} is 4.4, and the thickness h is 300 μm. The thickness of the metal used as a perfect conductor t is 35 μm. The differential-mode characteristic impedance Z_{d} was set to 100 Ω by using the ANSYS 2D Extractor for the cross-section stripline structure shown in Fig. 2.8.

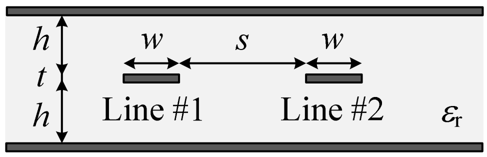

Figure 2.8 Cross-sectional view of symmetric stripline.

Table 2.1 Structural and electrical parameters of stripline.

Item	Value	Unit
ε_{r}	4.4	-
h	300	μm
t	35	μm

Figure 2.9 shows the relationship between the line width and line separation in terms of the differential-mode characteristic impedance. The thick black solid lines indicate the relationship based on the differential-mode characteristic impedance of 100 Ω. The black dot A indicates the case of the conventional bend and the common-mode characteristic impedances of 27.6 Ω. According to values of w and s of the conventional bend brought into Eq. (2.13), we can get the upper range of values for w_{n} and s_{n} of the tightly coupled bend. And, according to the rules of the manufacturer of this test board, the thinnest wiring width is 0.07 mm. Therefore, we can get the range of values for w_{n} and s_{n}, as shown

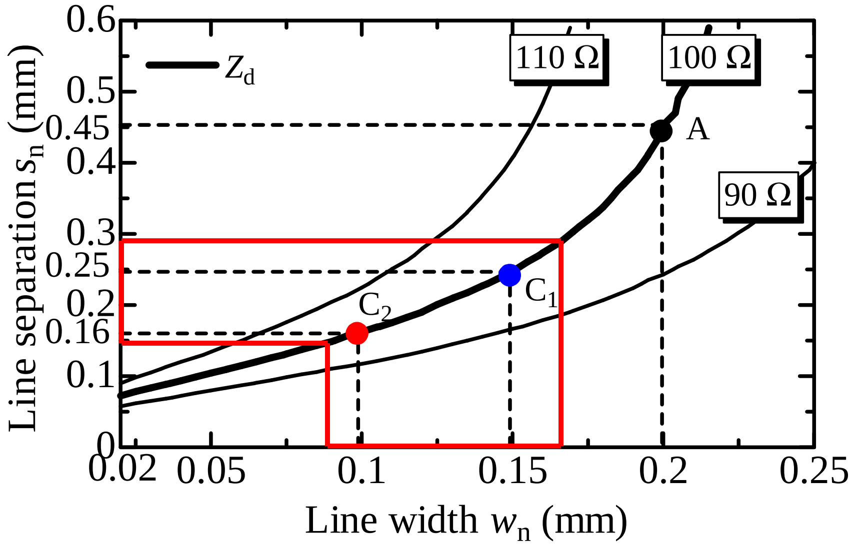

Figure 2.9 Relationship between line width and line separation for differential-mode characteristic impedances of 100 Ω.

in Fig. 2.9, the area surrounded by the red line. The blue dot and red dot indicate the cases of the tightly coupled bends with different sets of w_n and s_n. To investigate the impact of w_n and s_n on the differential-to-common mode conversion, one set of them is close to the upper limit of the value range, and the other chooses the smaller values within the range. The blue dot and red dot correspond to the tightly coupled part of the tightly coupled asymmetrically tapered bend C_1(same as the tightly coupled symmetrically tapered bend B) and the tightly coupled asymmetrically tapered bend C_2, as shown in Table 2.2. Next, using the determined values of w, s, w_n, and s_n into Eq. (2.16), we can calculate the l_t of bend C_1 and Bend C_2, respectively. Finally, l_s is obtained according to the design rules mentioned earlier.

Table 2.2 Structural parameters of bends for evaluating the impact of w_n and s_n on the differential-to-common mode conversion (unit in mm).

Item	A	B	C_1	C_2
w	0.2	0.2	0.2	0.2
s	0.45	0.45	0.45	0.45
w_n	-	0.15	0.15	0.1
s_n	-	0.25	0.25	0.16
l_t	-	0.15	0.15	0.83
l_s	-	0.5	0.5	0.5
l_{dg}	0.54	0.33	0	0

Although the tightly coupled part of bends C_1 and C_2 were designed so that the differential-mode characteristic impedance is equal to 100 Ω, the common-mode characteristic impedance was not controlled. The common-mode characteristic impedances in the tightly coupled part of bends C_1 and C_2 are 33.7 and 42 Ω, respectively.

2.4.2 Evaluation of Our Bend Structures from Differential-to-Common Mode Conversion

We evaluated the impact of w_n and s_n on the differential-to-common mode conversion of the new bend structure formed based on our design methodology by full-wave simulation for four types of 45-degree-angle bend structures of which the structural parameters are listed in Table 2.2.

Table 2.3 Simulation conditions.

Port conditions	
Port type	Waveport
Differential-mode impedance	100 Ω
Common-mode impedance	25 Ω
Solution setup	
Solution frequency	20 GHz
Max. delta S	0.02
Frequency sweep	
Sweep type	Interpolating
Start ∼ Stop	0.1 ∼ 20 (GHz)
Step size	0.1 GHz
Material	
Dielectric	FR-4 ε_r=4.4
Lines, GND	Perfect conductor

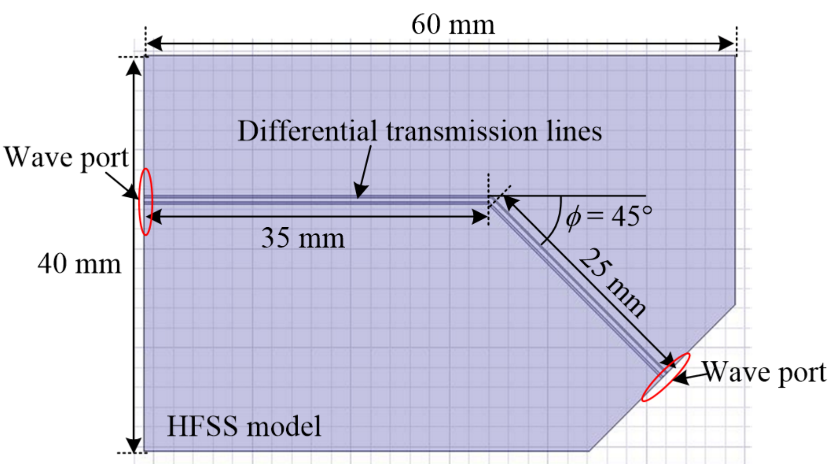

Figure 2.10 Top view of a full-wave simulation.

In the full-wave simulation, as shown in Table 2.3, two differential ports were set as wave ports with the port impedances of the differential mode of 100 Ω and the common mode of 25 Ω. The max delta S parameter represents the criterion for convergence and the solution frequency was set to 0.02 and 20 GHz, respectively. The frequencies ranging from 0.1 to 20 GHz. The dielectric constant of FR-4 ε_r is 4.4 (no material loss) and the metal used a perfect conductor. Figure 2.10 shows the HFSS model. The length of coupled straight lines from the differential port 1 to the bend region is 35 mm and the one from the differential port 2 to the bend region is 25 mm. The dimension of the dielectric is 60 mm × 40 mm.

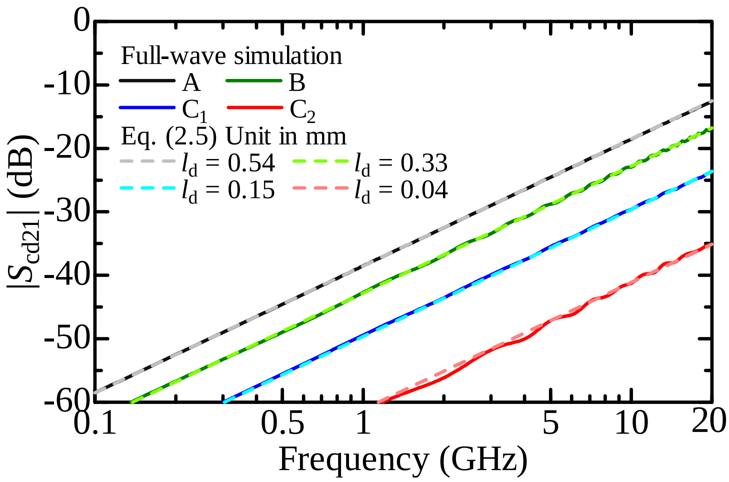

(a) Forward differential-to-common mode conversion

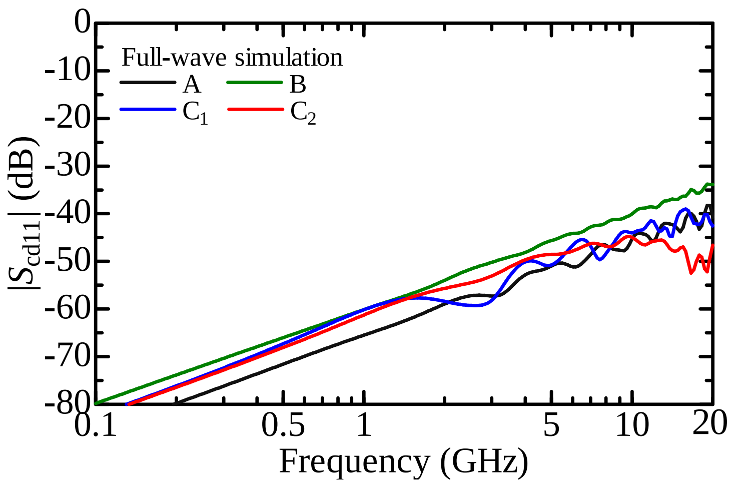

(b) Backward differential-to-common mode conversion

Figure 2.11 Comparison of differential-to-common mode conversion.

Figure 2.17(a) shows the forward differential-to-common mode conversion coefficient $|S_{\mathrm{cd21}}|$, and we found that the oblique tapers provide smaller $|S_{\mathrm{cd21}}|$ than that of symmetrically tapered bend B so that our new bend structures can compensate for the remaining l_{d} in the tightly coupled bend. Figure 2.17(a) includes the dashed lines obtained by re-

Table 2.4 Comparison of geometrical path difference and effective path difference (unit in mm).

Item	A	B	C_1	C_2
l_{dg}	0.54	0.33	0	0
l_d	0.54	0.33	0.15	0.04

placing the geometrical path difference l_{dg} with the effective path difference l_d in Eq. (2.5). The values of the geometrical path difference l_{dg} and the effective path difference l_d are summarized in Table 2.4. The magnitude of $|S_{cd21}|$ in bend C_2 was smallest, though all the geometrical path difference l_{dg} of bends C_1 and C_2 were set to 0. This is because the geometrical path difference l_{dg} becomes less different than the effective path difference l_d with decreasing w_n and s_n, and the effective path difference l_d of the smallest bend C_2 is almost equal to 0, as shown in Table 2.4. Then, it found that $|S_{cd21}|$ was decreased by almost 20 dB compared to that of the conventional bend. For next-generation high-speed interfaces, the challenging specifications are $|S_{cd21}| <$ -30 dB when frequency below 15 GHz [6]. However, proposed bend C_2 can be below -30 dB until to 20 GHz.

As a result, for the design methodology of our tightly coupled asymmetrically tapered bend, if we want to get a lower the forward differential-to-common mode conversion coefficient $|S_{cd21}|$, choose as small as possible w_n and s_n.

Next, Fig. 2.17(b) first shows the backward differential-to-common mode conversion. It is seen from this figure that the backward differential-to-common mode conversion of bends A, B, and C are below -30 dB until to 20 GHz. This means that the forward differential-to-common mode conversion occupies a dominant in the differential-to-common mode conversion.

2.4.3 Evaluation of Our Bend Structures from Viewpoint of Differential Mode

Let us now evaluate the new proposed bend structure from the viewpoint of the differential mode.

Figure 2.12(a) first shows the differential-mode reflection coefficients. It is seen from this figure that the differential mode reflection coefficients of bends A, B, and C are below -30 dB until to 20 GHz. This is because that the tapers can maintain the differential-mode characteristic impedance at around 100 Ω, as shown in Fig. 2.9. And, the differential-mode reflection coefficients is small enough. Thus it does not affect the differential-mode transmission coefficients.

Next, the differential-mode transmission coefficients for all the bends are compared in Fig. 2.12(b), which demonstrates that $|S_{dd21}|$ influences the differential-mode transmission coefficient, but it's not very big. The magnitude of $|S_{dd21}|$ in bend C_2 was almost unity (0 dB) compare to the other bends.

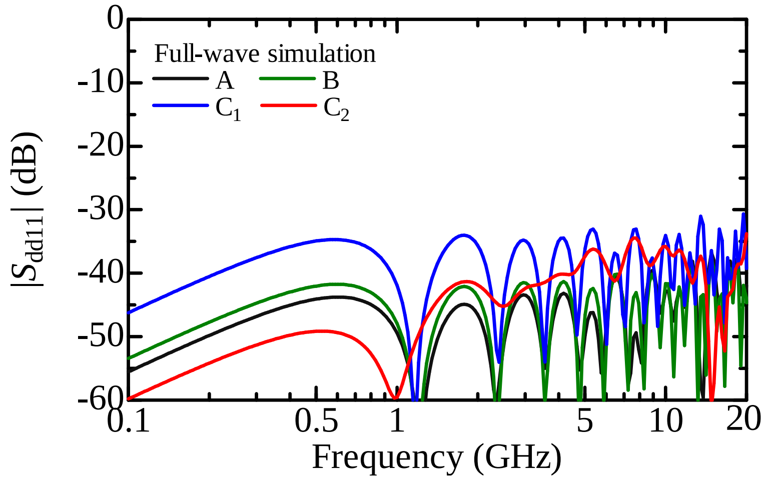

(a) Differential-mode reflection coefficient

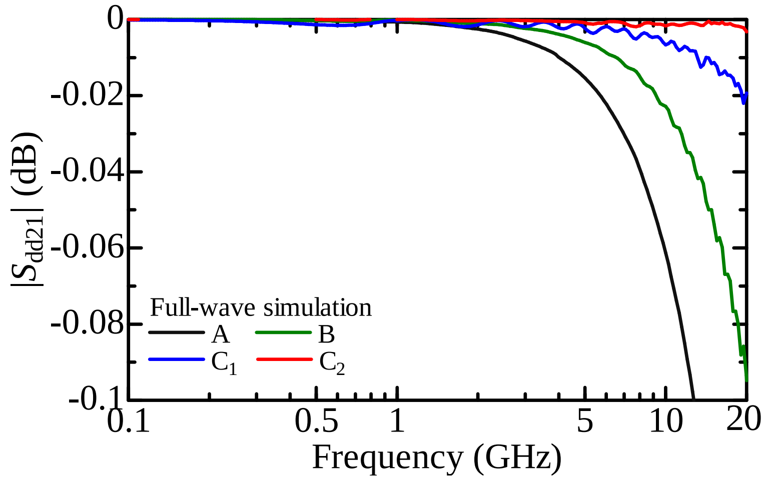

(b) Differential-mode transmission coefficient

Figure 2.12 Comparison of differential-mode characteristics.

And, the transmission characteristics of the proposed bend are evaluated from the viewpoint of the phase. Here, we focused on the group delay obtained from the phase characteristics of S_{dd21}. If this group delay is larger than that of the conventional bend and waveform distortion occurs during transmission, so the SI deteriorates, and it cannot be used as a line for signal transmission.

The following equation expresses the group delay time T_{g} in terms of the derivative of the phase characteristics $\angle S_{\mathrm{dd21}}$ with respect to frequency.

$$T_{\mathrm{g}} = -\frac{1}{2\pi}\frac{d\angle S_{\mathrm{dd21}}}{df}, \tag{2.17}$$

The group delay time obtained by Eq. (2.17) is shown in Fig. 2.13. These results show that T_{g} for when the proposed bend has almost the same characteristics as the conventional bend has. As a result, the proposed bend structure takes the smallest distortion in the output waveform, and the signal can be successfully transmitted.

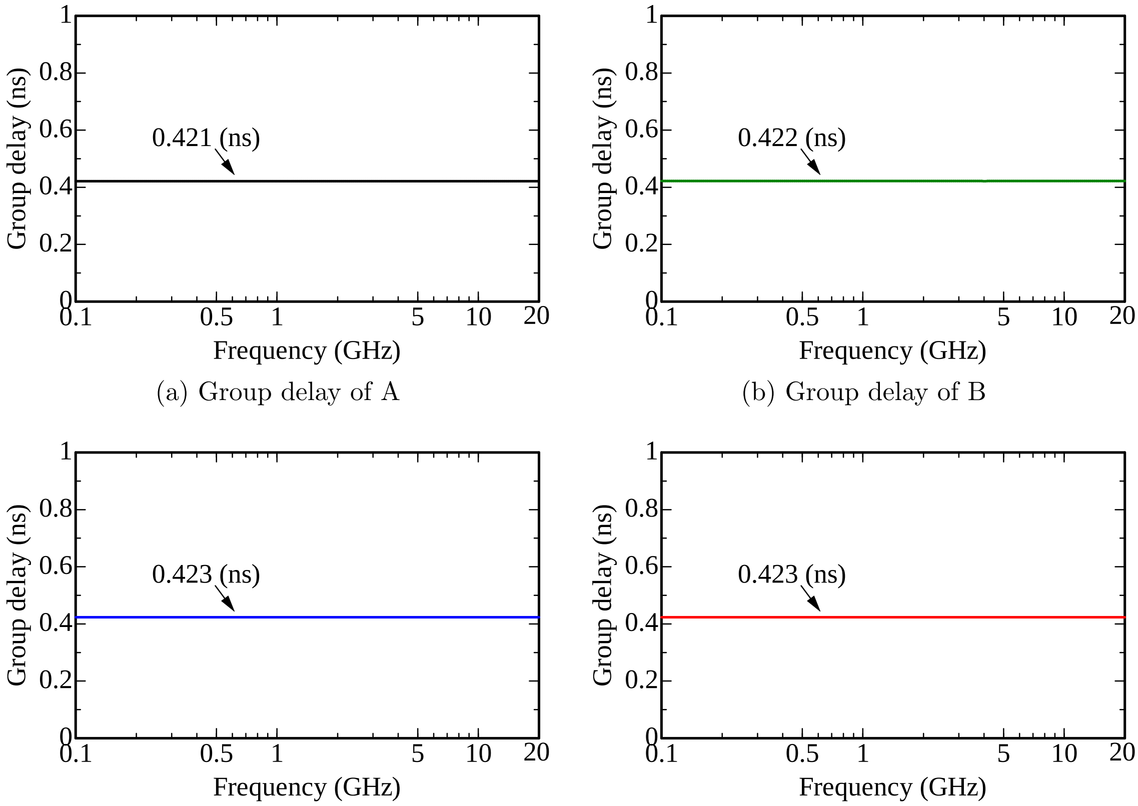

(a) Group delay of A

(b) Group delay of B

(c) Group delay of C_1

(d) Group delay of C_2

Figure 2.13 Comparison of group delay.

This means that bend C_2 great suppresses differential-to-common mode conversion and had no effect on differential-mode transmission characteristics.

2.5 Fabrication of New Bend Structures and Evaluation by Measurement

In this section, the bends with the same structural parameters (bends A, C_1, and C_2) from the previous discussion were fabricated, and the differential-to-common mode conversion and differential-mode characteristics were evaluated through full-wave simulation and measurement.

2.5.1 Fabrication of Proposed Bend and Evaluation by Measurement

Table 2.5 summarizes the common structural and electrical parameters. To compare with measurement, dielectric loss $\tan\delta$ and copper conductivity σ were taken into account in full-wave simulation. The differential-mode characteristic impedance Z_{d} was set to 100

Ω the same as before.

Figure 2.14 shows the test board used in the actual measurement of the fabricated test board and Fig. 2.14(a) shows the layer structure and Fig. 2.14(b) shows the ACP probe pad structure. In Fig. 2.14(a), each layer configuration is assumed to be used in electronic equipment, and copper is used as the conductor. The glass epoxy material was used between the layers. The stripline structure used through-hole signal vias. The lengths of coupled straight lines from the differential ports 1 and 2 to the bend region are 35mm and 25 mm, respectively. And the proposed structure was applied to the bend region.

Table 2.5 Common structural and electrical parameters.

Item	Value	Unit
ε_{r}	4.4	-
$\tan\delta$	0.02	-
σ	5.8×10^{7}	-
h	300	μm
t	35	μm
Z_{d}	100	Ω

Table 2.6 Equipment and model number used for test board measurement.

Item	Manufacturer	Model Number
ACP Probe	Cascade Microtech	GSGSG-200(JG22K，KL2HK)
Network Analyzer	KEYSIGHT	E5071C

Table 2.7 Test board measurement conditions.

Condition	Value
Start frequency (GHz)	0.1
Stop frequency (GHz)	20
Points (pt)	1601

To obtain mixed-mode S parameters, an 4-port measurement was carried out using a vector network analyzer (VNA) and a pair of 200-μm-pitched GSGSG microprobes. Table 2.6 shows the equipment and model numbers used. Table 2.7 shows the test board measurement conditions. The measured data were plotted below 20 GHz due to the measurement limit of the vector network analyzer. This vector network analyzer (VNA) and a pair of 200-μm-pitched GSGSG microprobes will also be used in Chapters 3 and 4.

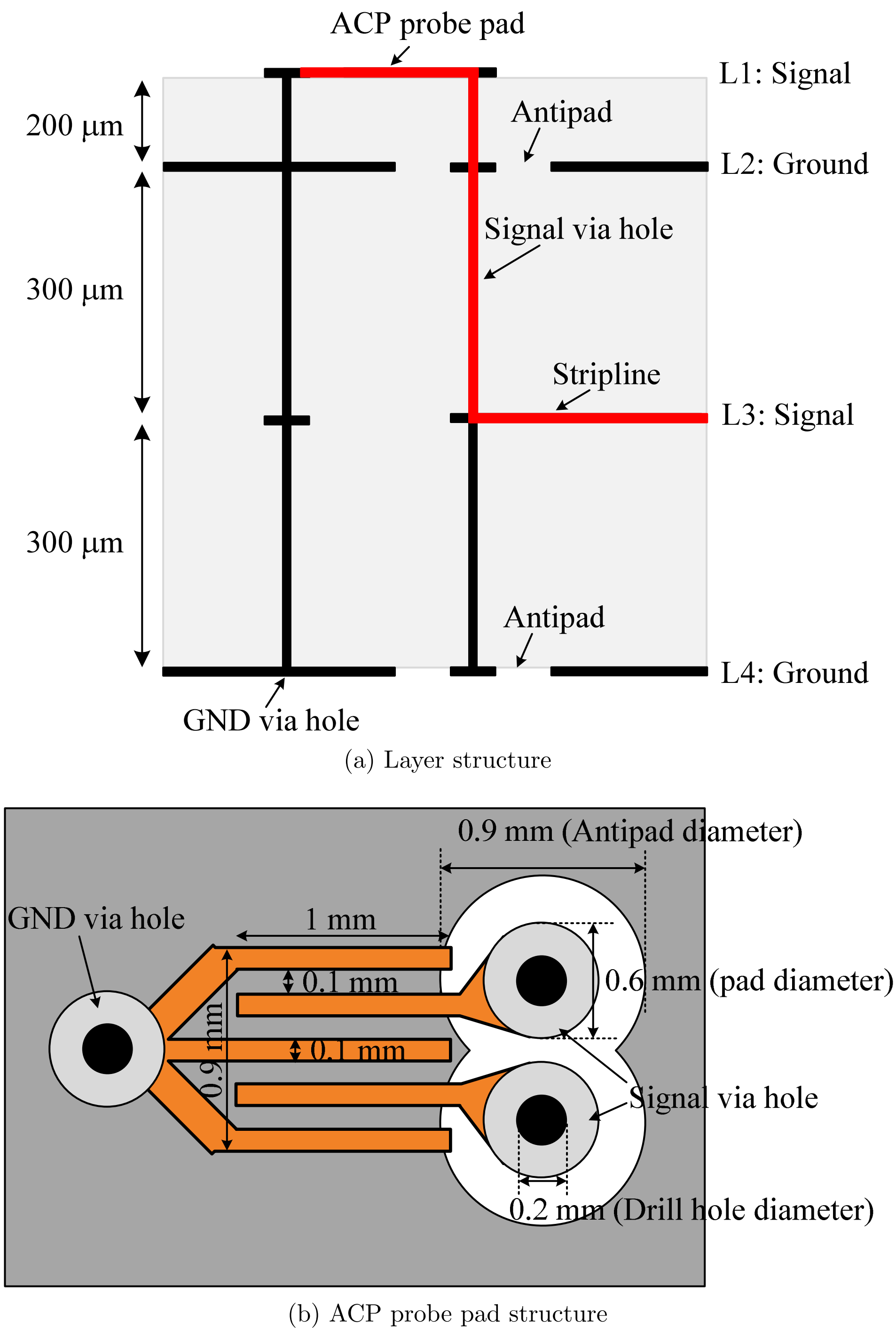

Figure 2.14 Layer structure and stripline bend structure.

To compare with measurement, dielectric loss tanδ and copper conductivity σ were taken into account in full-wave simulation, as shown in Table 2.8. And, the probe pads and the through-hole signal vias (using the same size as the design drawing, as shown in Fig. 2.14(b)) added on two-terminal of differential transmission lines. Each port was set as lumped ports with the port impedances of the differential mode of 100 Ω and the

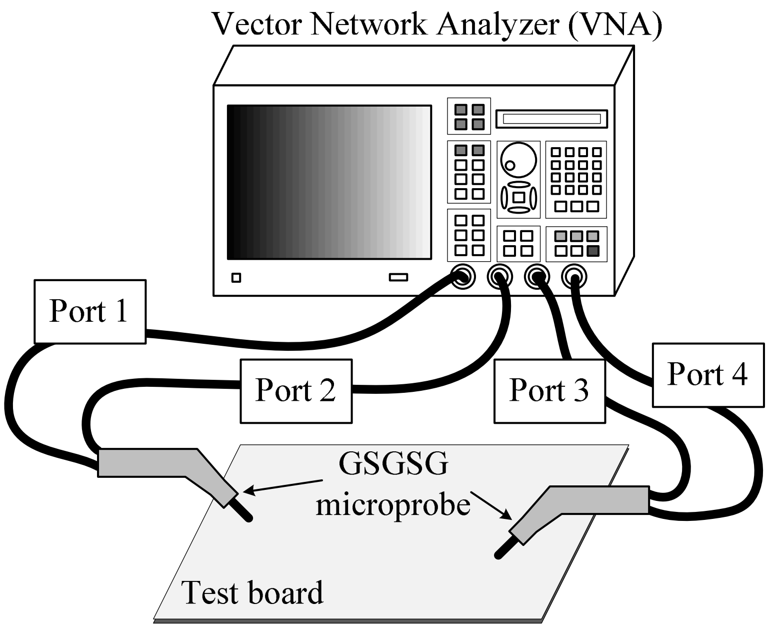

Figure 2.15 System layout for measuring.

common mode of 25 Ω. Figure 2.16 shows the full-wave simulation added two probe pad to compare with the measurement. The length of coupled straight lines from the differential port 1 to the bend region is 35 mm and the one from the differential port 2 to the bend region is 25 mm. The dimension of the dielectric is 75 mm × 40 mm.

Table 2.8 Simulation conditions.

Port conditions	
Port type	Lumpedport
Differential-mode impedance	100 Ω
Common-mode impedance	25 Ω
Solution setup	
Solution frequency	20 GHz
Max. delta S	0.02
Frequency sweep	
Sweep type	Interpolating
Start ∼ Stop	0.1 ∼ 20 (GHz)
Step size	0.1 GHz
Material	
Dielectric	FR-4 ε_r=4.4/tanδ=0.02
Lines, GND	Copper σ=5.8×10^7

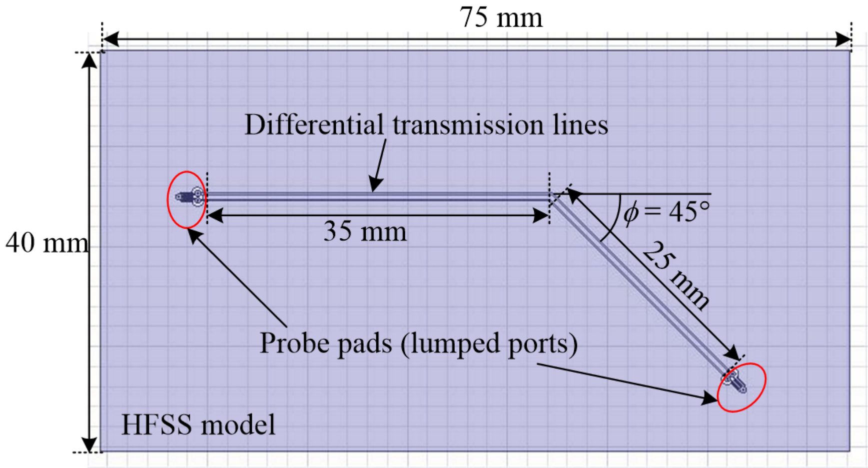

Figure 2.16 Full-wave simulation added two probe pad to compare with the measurement.

2.5.2 Evaluation of Our Bend Structures from measurement

Figure 2.17(a) shows the forward differential-to-common mode conversion $|S_{\mathrm{cd21}}|$ as a function of frequency concerning bends A, C_1, and C_2, and the solid lines indicate the measurement results. On the other hand, the broken lines indicate the full-wave simulation

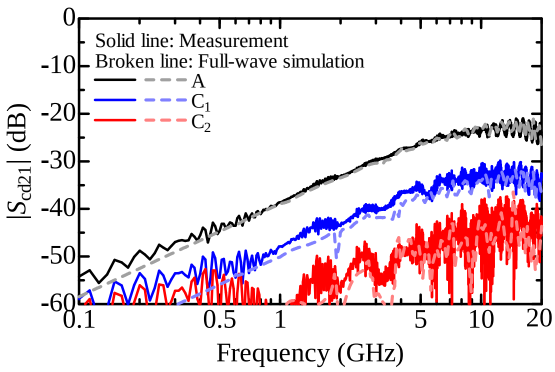

(a) Forward differential-to-common mode conversion

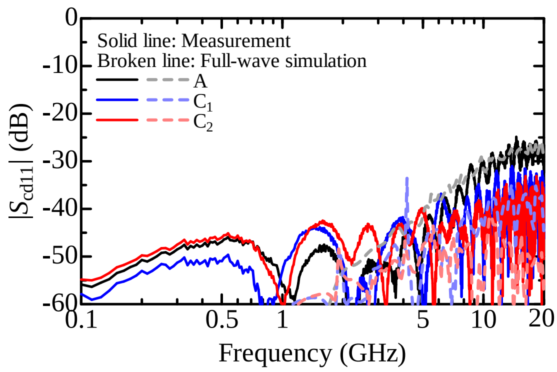

(b) Backward differential-to-common mode conversion

Figure 2.17 Comparison of differential-to-common mode conversion.

results. As a result, it is found that the results obtained from the full-wave simulation are almost in agreement with measurement. Here, we have observed multiple reflections at high frequencies. This is because the impedance of the probe pads (including through-hole signal vias) is not the same as the differential transmission lines. But, these results are sufficient to confirm that reduces the difference between the geometric path difference and the effective path difference by reducing the line width w_{n} and line separation s_{n} of the tightly coupled bend. And, the forward differential-to-common mode conversion $|S_{\mathrm{cd21}}|$

of bend C_2 was decreased by approximately 20 dB compared to bend A.

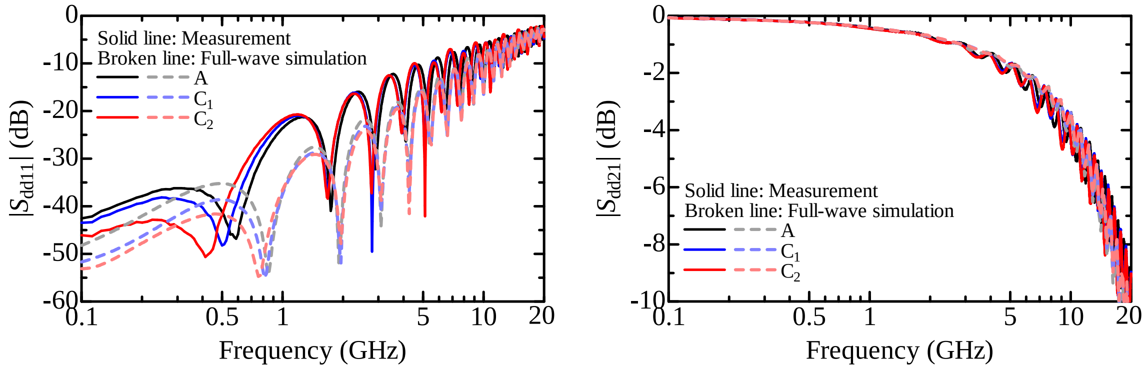

(a) Differential-mode reflection coefficient (b) Differential-mode transmission coefficient

Figure 2.18 Comparison of differential-mode characteristics.

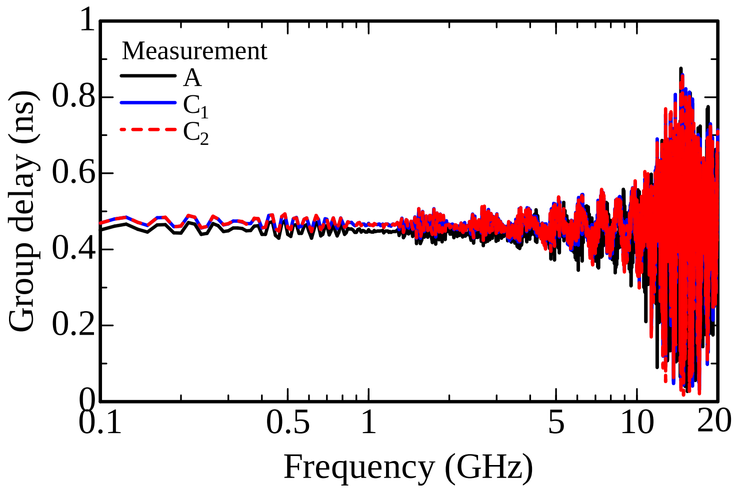

Figure 2.19 Comparison of group delay obtained by measurement.

Next, Fig. 2.17(b) shows the backward differential-to-common mode conversion $|S_{\mathrm{cd11}}|$ as a function of frequency. The backward differential-to-common mode conversion of bends C_1 and C_2 is smaller compare to bend A in full-wave simulation. And, the measurement results show the same characteristics in over 5 GHz. This means that our bend structures produce a smaller amount of differential-to-common mode conversion than bend A.

Then, as shown in Fig. 2.18(a), the differential-mode reflection $|S_{\mathrm{dd11}}|$ of bends C_1 and C_2 is lower compare to bend A below 1 GHz, whether it's measurement or full-wave simulation. This means that our bend structure will not affect the differential-mode reflection $|S_{\mathrm{dd11}}|$ of the conventional bend. The increase of $|S_{\mathrm{dd11}}|$ at higher frequencies results from the effect of the probe pads.

The last is the differential-mode transmission coefficient, as shown in Fig. 2.18(b). As a result, it is found that the results obtained from the full-wave simulation are almost in agreement with measurement, and the bends C_1 and C_2 are comparable with bend A.

And, the group delay time obtained by Eq. (2.17) is shown in Figs. 2.19. These results show that T_g for when the proposed bend has almost the same characteristics as the conventional bend has. As a result, the proposed bend structure takes the smallest distortion in the output waveform when frequency below 5 GHz. The increase of distortion in the output waveform at higher frequencies results from the effect of the probe pads.

This means that the proposed bend greatly suppresses differential-to-common mode conversion and has almost the same transmission characteristics as the conventional bend has.

2.5.3 Comparison with Bend Structures Using Various Compensation Methods

Various methods have been proposed for compensating for mode conversion due to the bend of the differential line. Here are some of them : 1) The right-angle bend differential transmission lines with compensation capacitance implemented as open stubs, as shown in Fig. 2.20(b) [26]. 2) The right-angle bend differential transmission lines using a short-circuited coupled line, as shown in Fig. 2.22(b) [25]. 3) Common practical routing scheme using a small detour for the inner trace of coupled bends, as shown in Fig. 2.24(b) [18]. 4) Right-angle bend differential transmission lines with slow-wave sections, as shown in Fig. 2.26(b) [27]. 5) Round-corner bends, as shown in Fig. 2.28(b). We applied the proposed tightly-coupled bend structure with the asymmetric taper to the bends described in these papers according to the design procedure shown in this thesis and compared the characteristics by 3D electromagnetic simulation.

In terms of the high-density wiring, the proposed bend structure is clearly superior, as as shown in Figs. 2.20(c), 2.22(c), 2.24(c), 2.26(c), and 2.28(c). From this, it can be seen that these structures were designed to don't think about high-density wiring in general and focusing only on the reduction of the amount of the differential-to-common mode conversion.

Regarding the propagation characteristics, we first confirmed whether the characteristics described in these papers could be reproduced by 3D electromagnetic simulation. Although the details of the spectrum dips and peaks do not always match, the levels and trends were reproduced, so this was used for comparison.

Figs. 2.20 to 2.28 show the comparison between the mode conversion amount (Forward and backward differential-to-common mode conversion) and the propagation characteristics (Differential-mode reflection and transmission coefficient) with the conventional bend structures and proposed bend in this thesis by 3D electromagnetic simulation. As can be seen from these results, the proposed structures in each paper have improved characteristics compared to the conventional bend structures, but the proposed bend structures are equivalent or superior.

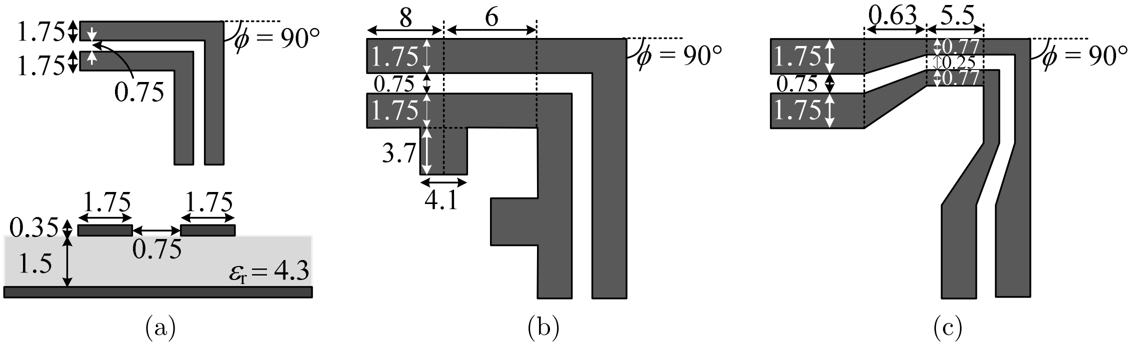

Figure 2.20 Physical structures of various bend differential transmission lines and the cross-sectional view (unit in mm). (a) Right-angle bends. (b) Right-angle bend differential transmission lines with compensation capacitance implemented. (c) Proposed bend in this thesis.

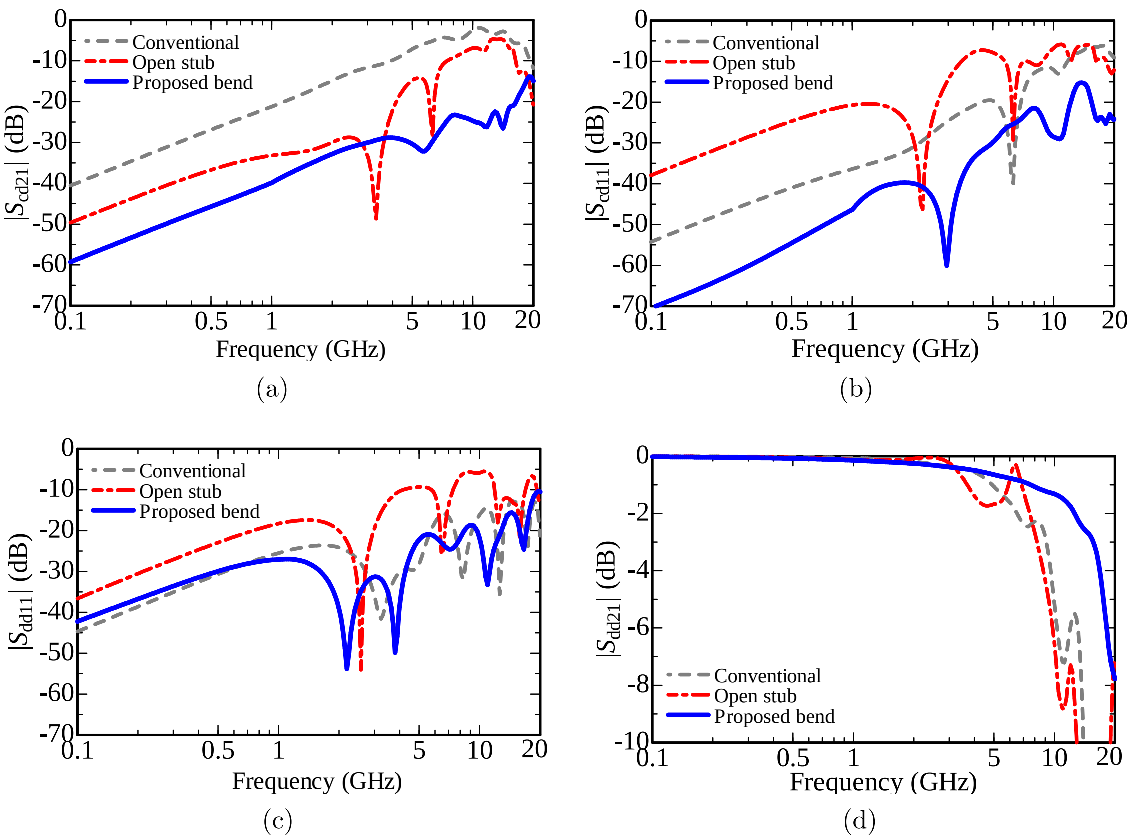

Figure 2.21 Simulation results for bend structures of Fig. 2.20. (a) Forward differential-to-common mode conversion. (b) Backward differential-to-common mode conversion. (c) Differential-mode reflection coefficient. (d) Differential-mode transmission coefficient.

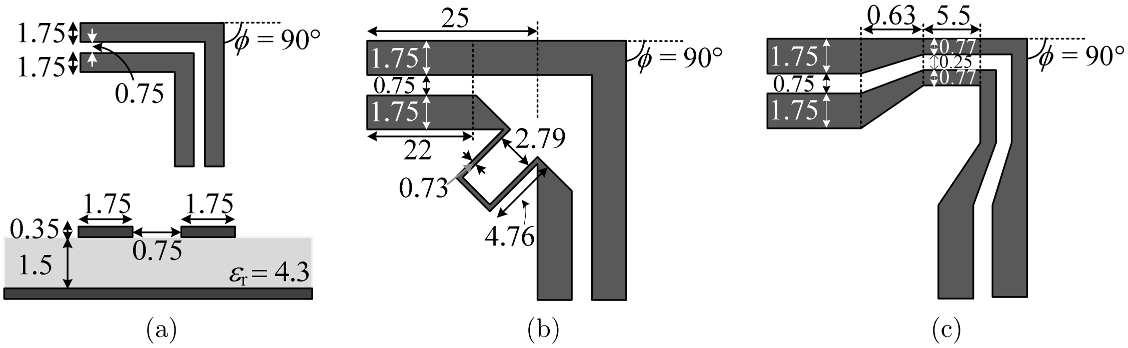

Figure 2.22 Physical structures of various bend differential transmission lines and the cross-sectional view (unit in mm). (a) Right-angle bends. (b) Right-angle bend differential transmission lines using short-circuited coupled line. (c) Proposed bend in this thesis.

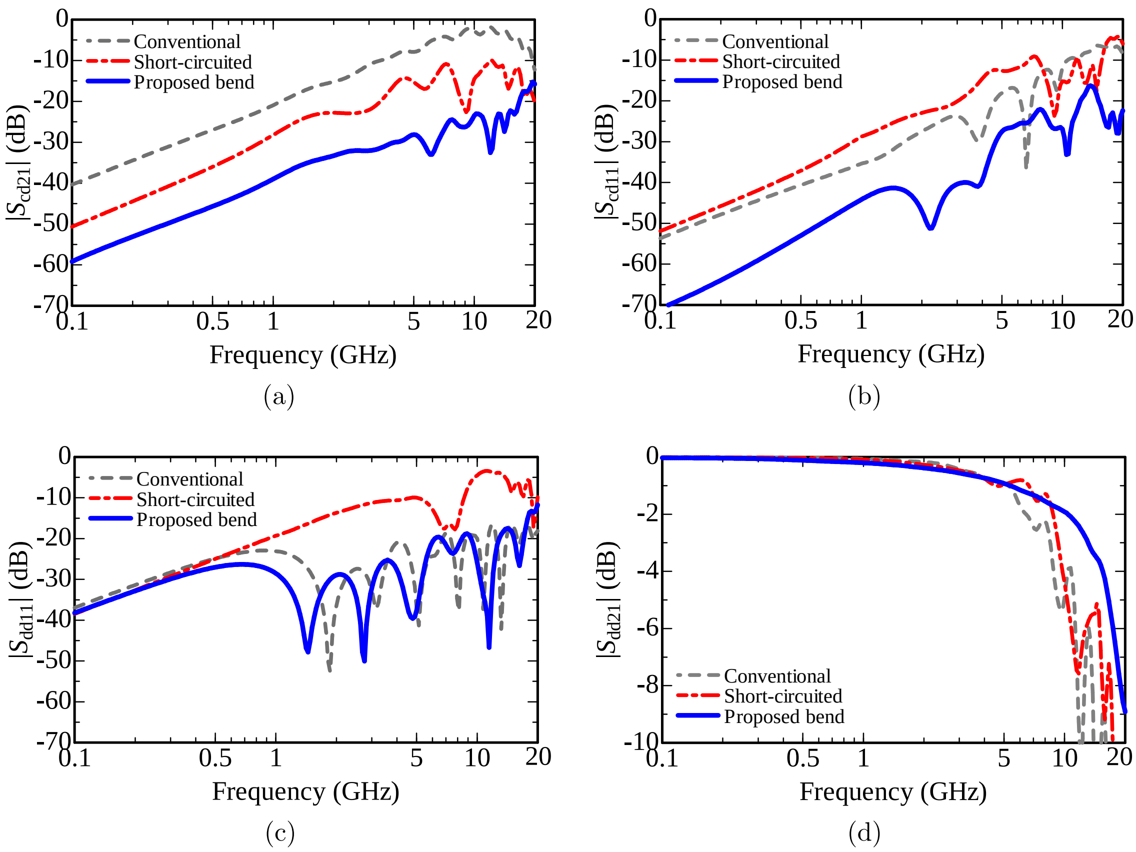

Figure 2.23 Simulation results for bend structures of Fig. 2.22. (a) Forward differential-to-common mode conversion. (b) Backward differential-to-common mode conversion. (c) Differential-mode reflection coefficient. (d) Differential-mode transmission coefficient.

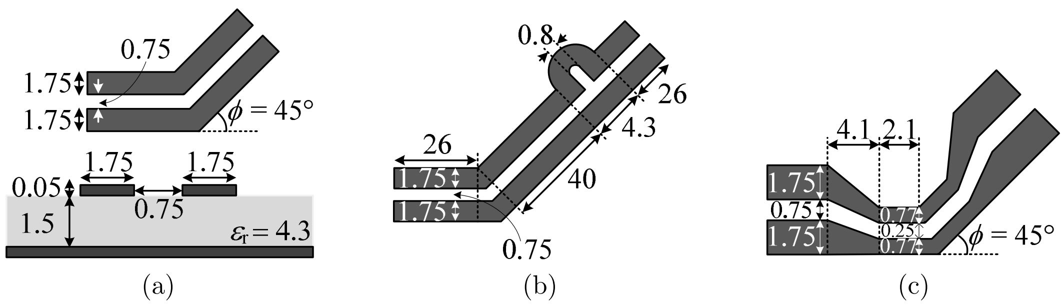

Figure 2.24 Physical structures of various bend differential transmission lines and the cross-sectional view (unit in mm). (a) 45-degree-angle bends. (b) Common practical routing scheme using a small detour. (c) Proposed bend in this thesis.

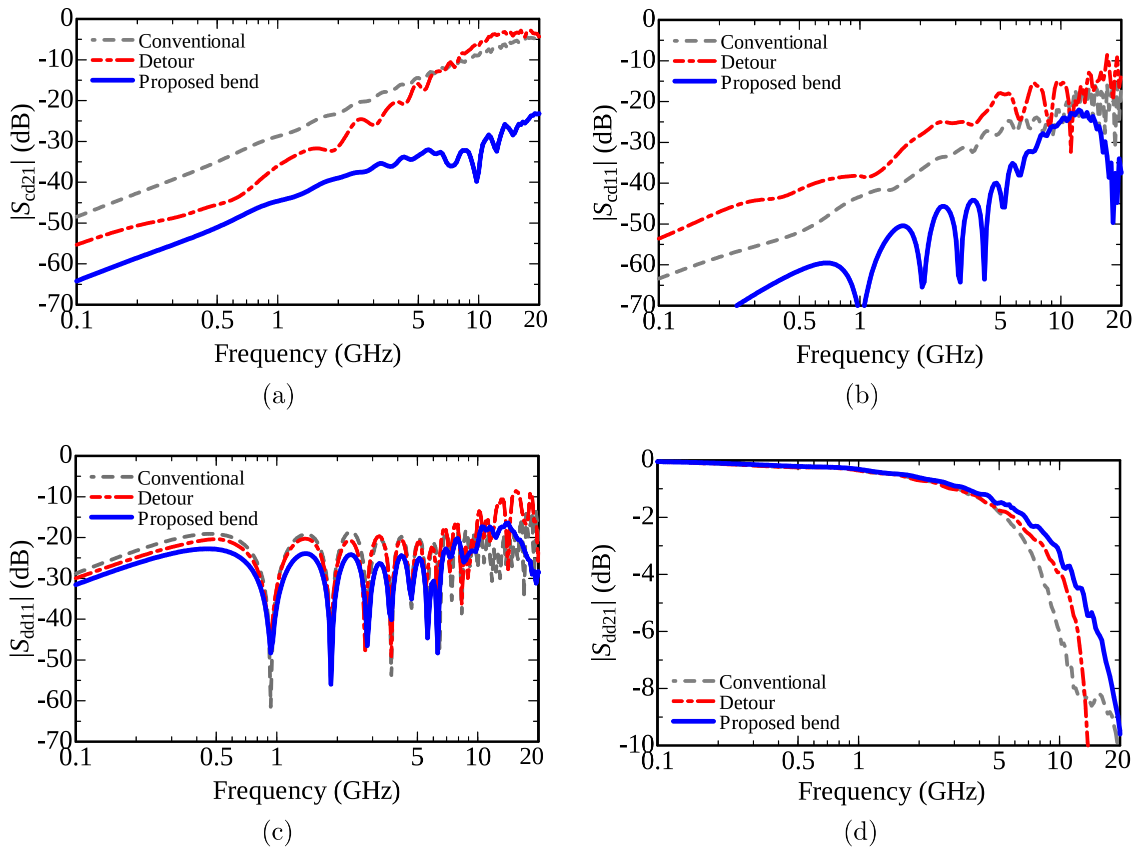

Figure 2.25 Simulation results for bend structures of Fig. 2.24. (a) Forward differential-to-common mode conversion. (b) Backward differential-to-common mode conversion. (c) Differential-mode reflection coefficient. (d) Differential-mode transmission coefficient.

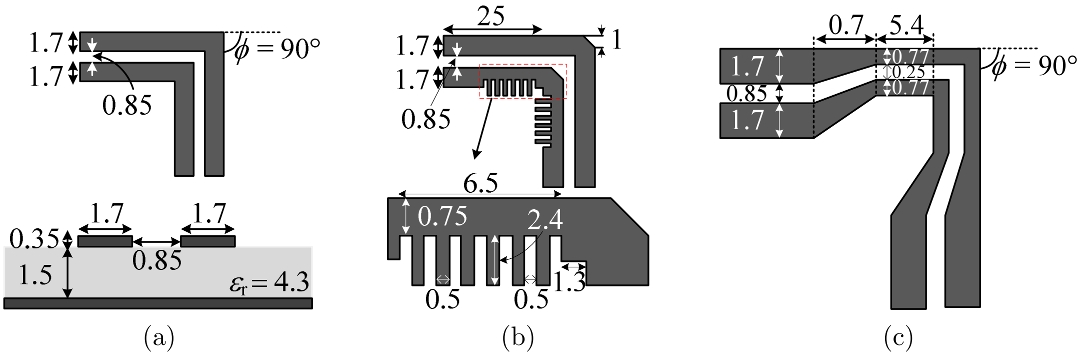

Figure 2.26 Physical structures of various bend differential transmission lines and the cross-sectional view (unit in mm). (a) Right-angle bends. (b) Right-angle bend differential transmission lines with slow-wave sections. (c) Proposed bend in this thesis.

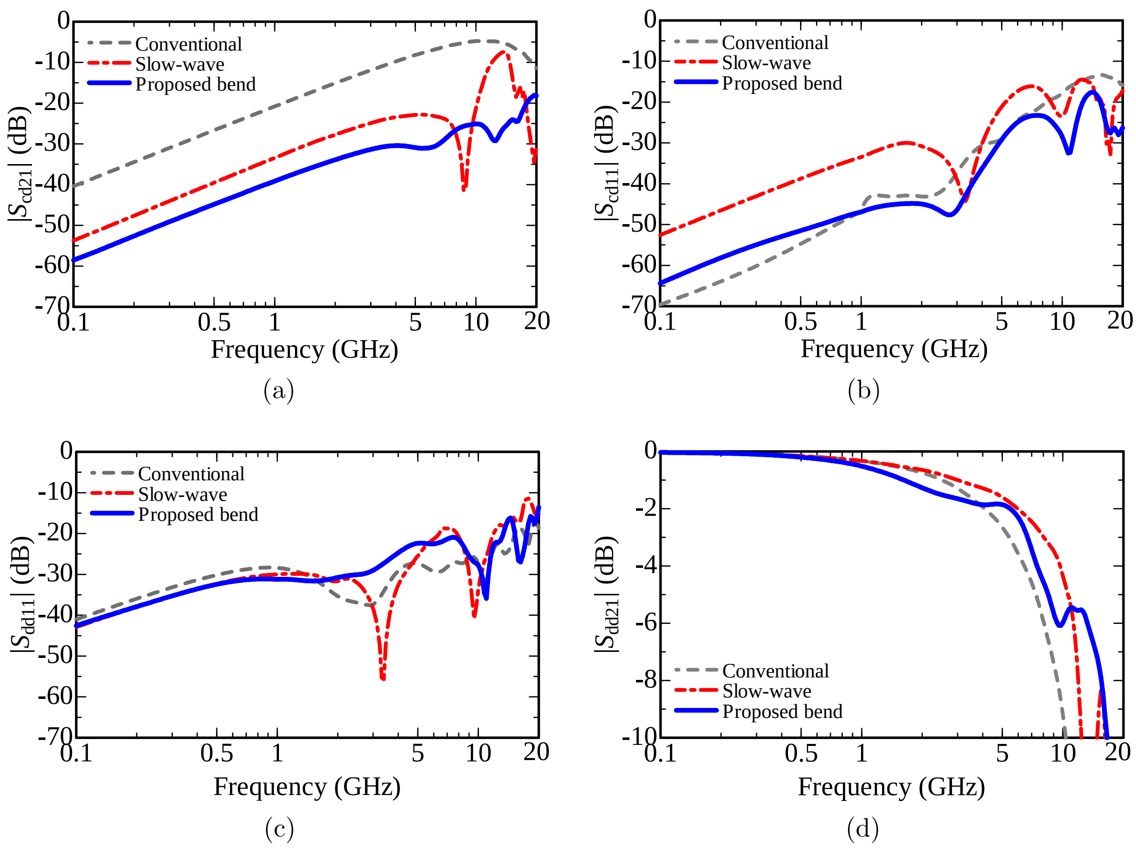

Figure 2.27 Simulation results for bend structures of Fig. 2.26. (a) Forward differential-to-common mode conversion. (b) Backward differential-to-common mode conversion. (c) Differential-mode reflection coefficient. (d) Differential-mode transmission coefficient.

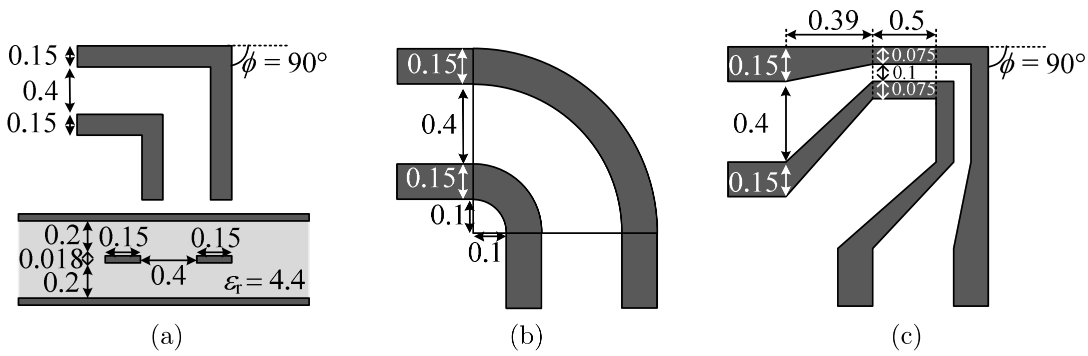

Figure 2.28 Physical structures of various bend differential transmission lines and the cross-sectional view (unit in mm). (a) Right-angle bends. (b) Round-corner bends. (c) Proposed bend in this thesis.

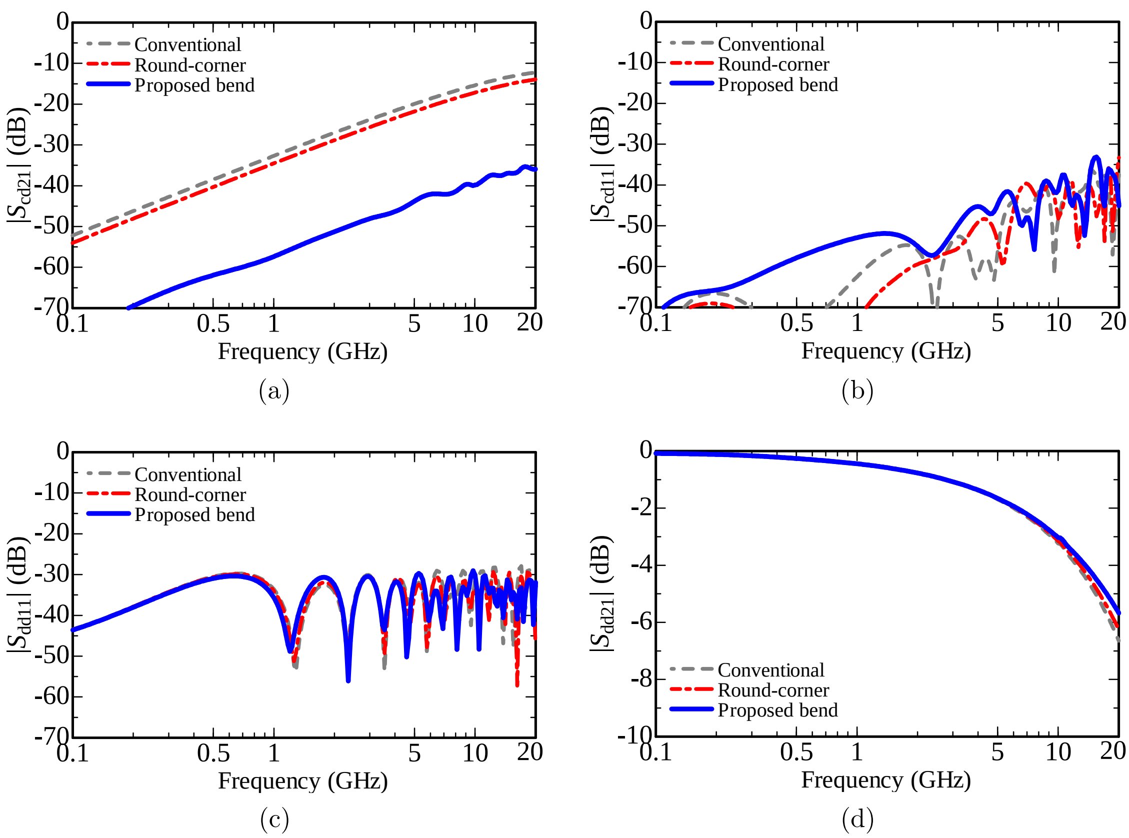

Figure 2.29 Simulation results for bend structures of Fig. 2.28. (a) Forward differential-to-common mode conversion. (b) Backward differential-to-common mode conversion. (c) Differential-mode reflection coefficient. (d) Differential-mode transmission coefficient.

2.6 Conclusion

In this chapter, we proposed a tightly coupled asymmetrically tapered bend for high-density wiring that can improve signal quality degradation for the bend structure of differential transmission lines. For it, we proposed the design methodology of our tightly coupled asymmetrically tapered bend to limit the bend within the area of the conventional bend, which is determined geometrically from the bend structure.

Full-wave simulation and measurement results of a 45-degree-angle bend showed that the new bend structure formed based on our design methodology suppressed differential-to-common mode conversion $|S_{\mathrm{cd21}}|$ and provides better or similar transmission characteristics compared to the original classic bend structure caused by bend discontinuity in a pair of differential lines. And, for the design methodology of our tightly coupled asymmetrically tapered bend, want to get a smaller the forward differential-to-common mode conversion coefficient $|S_{\mathrm{cd21}}|$, choose as small as possible w_{n} and s_{n} of the tightly coupled bend.

Then, using 3D electromagnetic simulation and measurement evaluated the 45 degree-angle bend formed based on our design methodology and found that the differential-to-common mode conversion was decreased by almost 20 dB and maintain its transmission characteristics compared to those of the conventional bend.

Furthermore, when compared with the compensation method proposed in other documents, the high-density wiring is clearly superior, and the simulation results show that the mode conversion amount (Forward and backward differential-to-common mode conversion) and the propagation characteristics (Differential-mode reflection and transmission coefficient) is equal or superior to those of other structures.

From the above, it can be said that the proposed structure is a bent structure with an extremely small mode conversion suitable for high-density wiring.

Chapter 3

Mitigating Differential Skew for High-density Mounting in Flexible Printed Circuits with a mesh ground

3.1 Introduction

In recent years, flexible printed circuit (FPC) boards have been increasingly used in electronic devices as these devices become smaller and lighter. The dielectric of an FPC is very thin, and the characteristic impedance of its differential transmission lines is lower than the designated value, so the ground (i.e. the return path of the differential transmission lines) is formed into a mesh structure to increase the characteristic impedance without changing the line width. In general, as shown in Fig. 3.1, the meshed ground is rotated by 45° relative to the differential transmission lines ($\phi = 45°$). The ground is also arranged such that the intersection position of the meshes are on the axis of symmetry of the differential transmission lines [44, 45].

When the design emphasizes symmetry in this manner, the interval between the adjacent differential transmission lines becomes dependent on the pitch of the meshed ground, making it difficult to set an arbitrary wiring interval. Considering the characteristic impedance, it is necessary to make the mesh pitch rough to cope with thinning of the dielectric, which results in lower packaging density. To improve the wiring density, the structure of the mesh must be changed; to do so, the wiring design of the lines must be redone first. In addition, it is challenging to arrange the lines and the meshed ground completely symmetrically in actual production. If the two are even slightly asymmetrical, the characteristic impedance changes [46], causing mode conversion and differential skew [47].

The effect of line position on the effective characteristic impedance of a single-ended line has been investigated in detail using full-wave simulation. When the angle between the wiring and the meshed ground (i.e. the rotation angle) is 0 or 45°, the characteristic impedance is heavily affected by the arrangement, but the effect is slight in the range of

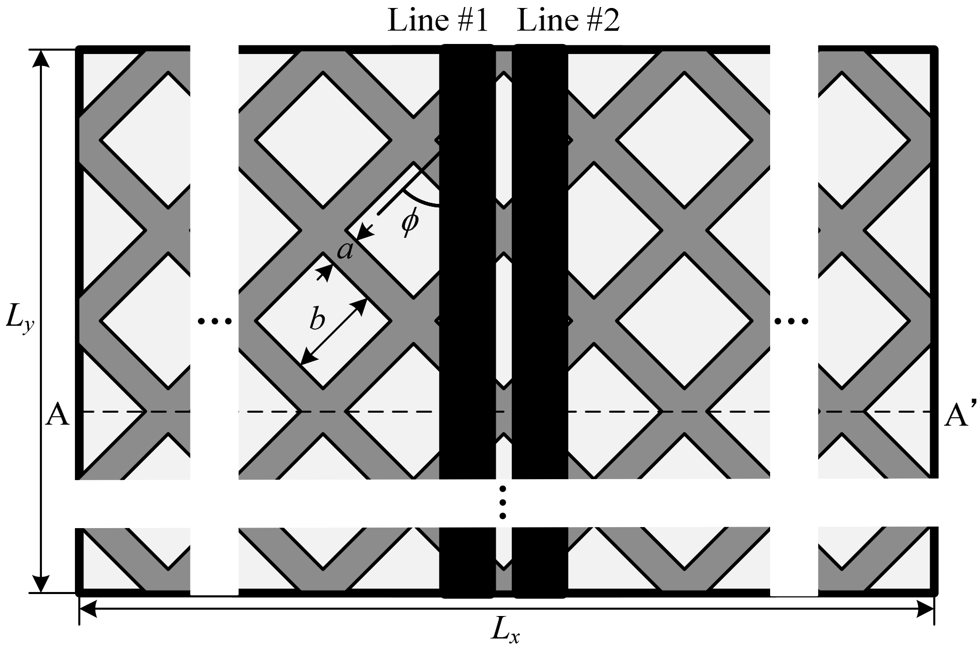

(a) Differential transmission lines with a meshed ground

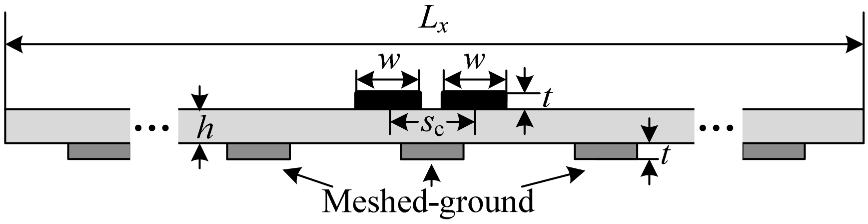

(b) cross-section along AA'

Figure 3.1 Differential transmission lines with a meshed ground and cross-section along AA'.

10 to 40°, and around 22.5°, the effective characteristic impedance is unaffected by the wiring position [46].

There is known a problem with the differential skew, such as the differential skew occurring in the differential transmission lines on a printed circuit board because of dielectric problems with the board's glass cloth [34, 35]. To solve this problem, it has been reported that the differential skew is mitigated when the angle between the trace of the differential transmission lines and the thread of the glass cloth is around 10° [43]. To the author' best knowledge, however, the angle dependence between 10° and 45°, especially the optimum angle has not been investigated. In this thesis, first, focuses on the angle between the trace of the differential lines and the meshed ground plane and investigates the angle dependence of the differential skew taking into account phase delay between two lines with propagation to find low differential skew at the angle other than 45°. And, a simple model was proposed for reducing the calculation time but is found to be able to evaluate the angle dependence of the differential skew at a similar accuracy to the 3D electromagnetic simulation [66, 67]. We also can apply this simple model to the board's glass cloth [65] (described in Appendix B).

Then, by setting the angle between the differential transmission lines and the meshed ground (the rotation angle) to between 30 and 40°, we found that the differential skew is not significantly affected by the position of the differential transmission lines and the meshed ground, and it becomes a relatively small value [66, 67]. As a result, it is found that the rotated meshed ground makes the phase difference between the two lines irregular at each mesh pitch to keep the differential skew small. Therefore, this thesis also proposed a randomly shifting mesh position, and evaluate the differential skew and characteristic impedance by the different position of the differential transmission lines.

In this chapter, first, we detail to explain that the simple model for the meshed ground [66, 67]. Next, we evaluated the differential skew caused by the meshed ground in detail using the simple model and full-wave simulation. Then, We built two sets of FPC test boards. Our first set of test boards were built to examine differential skew, characteristic impedance, and transmission characteristics. Our second set of test boards were built to evaluate the transmission characteristics of the differential transmission lines, including bending, to test the feasibility of high-density mounting. And, we show that the irregular phase difference by shifting the mesh position randomly does not affect the characteristic impedance nor differential skew in terms of the wiring position [67]. Finally, concludes with a summary. In this thesis, the differential-skew value is defined as the phase difference between the two lines in the differential transmission lines.

3.2 Simple Model for Meshed Ground

In this section, we will explain the simple model of mesh ground we have proposed. First, the calculation method of the phase change in each line of the differential wiring using a simple model with zero line width is explained. Then, how to consider the line width is described.

3.2.1 Differential Transmission Lines with Meshed Ground and Its Simple Model

In Fig. 3.1(a), the dark gray area shows the ground conductor mesh part, while the light gray area shows the part without the ground pattern. a and b indicate the mesh width and the distance between adjacent meshes, respectively. Fig. 3.1(b) shows the cross-sectional structure at AA' in Fig. 3.1(a), where w is the line width, and s_c is the distance between the centers of the lines Line #1 and Line #2. t is the thickness of the conductor, and h is the thickness of the dielectric. Lx and Ly represent the length of the mesh ground in the x-direction and the length in the y-direction, respectively, in the electromagnetic field simulation.

As shown in Fig. 3.2(a), the simplified model handled in this paper has two types of

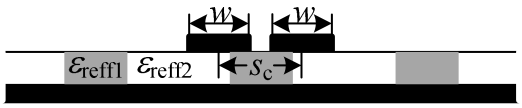

(a) Cross-sectional view

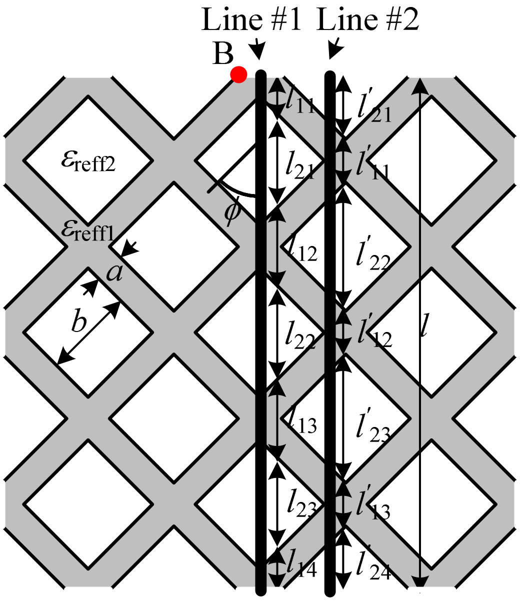

(b) simple model with no width

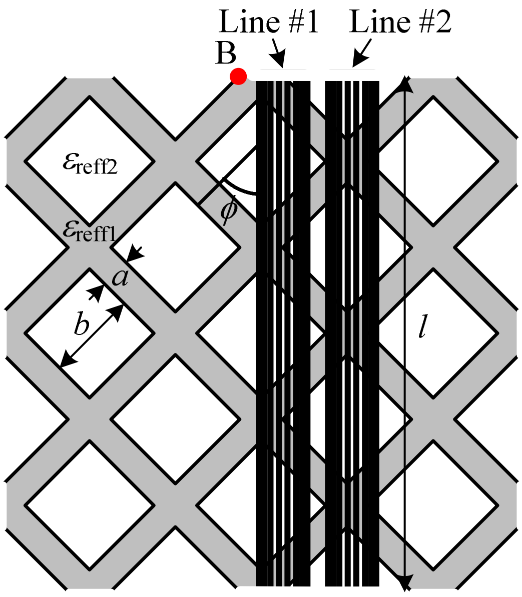

(c) simple model with width

Figure 3.2 Simple model treated in this paper.

relative dielectric constant $\varepsilon_{\rm reff1}$ and $\varepsilon_{\rm reff2}$ ($\varepsilon_{\rm reff1} > \varepsilon_{\rm reff2}$) that are uniform in the thickness direction of the dielectric. The ground is uniform. This model is not the mesh ground that is the subject of this paper, but the effect of mesh ground can be replaced by periodic changes in the effective relative permittivity is substituted. Also, for the sake of simplicity, the effective relative dielectric constant is assumed to be two values, $\varepsilon_{\mathrm{reff1}}$ and $\varepsilon_{\mathrm{reff2}}$. These correspond to the gray and white areas in Fig. 3.2(a), respectively.

In the calculation of the amount of the phase change on Line #1 and Line #2 of the differential transmission lines without and with the line width and these two cases were evaluated. Figures 3.2(b) and 3.2(c) show the in-plane structure of the simplified model when Line #1 and Line #2 are asymmetric concerning the meshed ground. Figure 3.2(b) does not consider the line width (the line width is zero assumed). Fig. 3.2(c) shows the case where the line width is taken into account.

3.2.2 Differential Skew Based on Phase Change Difference

First, consider the case of Fig. 3.2(b) where the line width is not considered. The length of Line #1 and Line #2 is l. Here, it is assumed that the coupling between the two lines is not considered, and the amount of phase change due to propagation is determined by the effective relative dielectric constant around the line. Since Line #1 and Line #2 pass over the two effective relative dielectric constants $\varepsilon_{\mathrm{reff1}}$ and $\varepsilon_{\mathrm{reff2}}$ alternately. For Line #1, for example, in Fig. 3.2(b), the lengths of l_{11}, l_{12}, l_{13}, ... correspond to the effective relative dielectric constant $\varepsilon_{\mathrm{reff1}}$. The length of l_{21}, l_{22}, l_{23}, ... correspond to the effective relative dielectric constant $\varepsilon_{\mathrm{reff2}}$. Therefore, the phase change amount of $\theta_{\mathrm{Line\#1}}$ of Line #1 can be expressed as follows

$$\theta_{\mathrm{Line\#1}} = \frac{\omega}{c}\left(\sum_{i=1}^{2}\sqrt{\varepsilon_{\mathrm{reff}i}}\sum_{j=1}^{N_i} l_{ij}\right) \tag{3.1}$$

where ω is the angular frequency and c is the speed of light in vacuum. N_1 and N_2 are the numbers of partial lines that pass through the dielectrics of effective relative dielectric constants $\varepsilon_{\mathrm{reff1}}$ and $\varepsilon_{\mathrm{reff2}}$ at Line #1, respectively. Also, l_{1j} and l_{2j} are the lengths of the jth partial line that passes through the dielectrics of effective relative dielectric constants $\varepsilon_{\mathrm{reff1}}$ and $\varepsilon_{\mathrm{reff2}}$ at Line #1, respectively.

For Line #2, for example, in Fig. 3.2(b), the lengths of l'_{11}, l'_{12}, l'_{13}, ... correspond to the effective relative dielectric constant $\varepsilon_{\mathrm{reff1}}$. The length of l'_{21}, l'_{22}, l'_{23}, ... correspond to the effective relative dielectric constant $\varepsilon_{\mathrm{reff2}}$. Therefore, the phase change amount of $\theta_{\mathrm{Line\#2}}$ of Line #2 can be expressed as follows

$$\theta_{\mathrm{Line\#2}} = \frac{\omega}{c}\left(\sum_{i=1}^{2}\sqrt{\varepsilon_{\mathrm{reff}i}}\sum_{j=1}^{M_i} l'_{ij}\right) \tag{3.2}$$

where M_1 and M_2 are the numbers of partial lines that pass through the dielectrics of effective relative dielectric constants $\varepsilon_{\mathrm{reff1}}$ and $\varepsilon_{\mathrm{reff2}}$ at Line #2, respectively. Also, l'_{1j} and l'_{2j} are the lengths of the jth partial line that passes through the dielectrics of effective relative dielectric constants $\varepsilon_{\mathrm{reff1}}$ and $\varepsilon_{\mathrm{reff2}}$ at Line #2, respectively.

From the above, the phase change difference $\Delta\theta$ between Line #1 and Line #2 is the difference between $\theta_{\text{Line\#1}}$ and $\theta_{\text{Line\#2}}$, and is given as follows

$$\Delta\theta = \frac{\omega}{c}\left|\sum_{i=1}^{2}\sqrt{\varepsilon_{\text{reff}i}}\left(\sum_{j=1}^{N_i} l_{ij} - \sum_{j=1}^{M_i} l'_{ij}\right)\right| \tag{3.3}$$

Here, the lengths of Line #1 and Line #2 are both l, there are the following relationships.

$$\begin{cases} \displaystyle\sum_{j=1}^{N_2} l_{2j} = l - \sum_{j=1}^{N_1} l_{1j} \\ \displaystyle\sum_{j=1}^{N_2} l'_{2j} = l - \sum_{j=1}^{N_1} l'_{1j} \end{cases} \tag{3.4}$$

Using these relationships, Eq, (3.3) can be rewritten

$$\Delta\theta = \frac{\omega}{c}\left(\sqrt{\varepsilon_{\text{reff1}}} - \sqrt{\varepsilon_{\text{reff2}}}\right)\left|\sum_{j=1}^{N_1} l_{1j} - \sum_{j=1}^{M_1} l'_{1j}\right|. \tag{3.5}$$

The purpose of calculation without considering the line width is to grasp the trend. Since the amount of calculation is small, the estimate becomes considerably rough.

Next, let us consider the case of considering the line width. In this case, the phase change of the line is given by the average value of the phase change of the divided line with zero line width. As shown in Fig. 3.2(c), the line widths of Line #1 and Line #2 are divided into multiple lines, and the amount of phase change due to propagation considered for the case of zero line width is considered for each line.

If the number of divided lines with zero line width is m, the phase change amount $\theta_{\text{Line\#1Ave}}$ of Line #1 is given as follows

$$\theta_{\text{Line\#1Ave}} = \frac{1}{m}\sum_{k=1}^{m}\frac{\omega}{c}\left(\sum_{i=1}^{2}\sqrt{\varepsilon_{\text{reff}i}}\sum_{j=1}^{N_{ik}} l_{ijk}\right) \tag{3.6}$$

Here, l_{ijk} is the length of the jth partial line that passes through the dielectric with the effective relative dielectric constants $\varepsilon_{\text{reff}i}$ in the divided kth line with zero line width. The phase change $\theta_{\text{Line\#1Ave}}$ of Line #2 is obtained in the same way.

Now consider how far the line width is divided. The more m, the more stable the analytical results, however, considering the analysis time, it is sufficient to set m to a suitable amount. In this paper, it was judged from the convergence of the effective relative dielectric constant when m was increased. From Eq. (3.6), effective relative dielectric constant of Line #1 as a whole is given as follows

$$\varepsilon_{\text{reffLine\#1}} = \left(\frac{\theta_{\text{Line\#1Ave}}c}{l\omega}\right)^2 = \left\{\frac{1}{ml}\sum_{k=1}^{m}\left(\sum_{i=1}^{2}\sqrt{\varepsilon_{\text{reff}i}}\sum_{j=1}^{N_{ik}} l_{ijk}\right)\right\}^2 \tag{3.7}$$

Table 3.1 summarizes the structural parameters and the values used in Sections 3.2 and 3.3. The effective relative dielectric constants $\varepsilon_{\mathrm{reff1}}$ and $\varepsilon_{\mathrm{reff2}}$ shown in Table 3.1 are values obtained from the cross-sectional structure of single-ended wiring using a commercially available simulator ANSYS 2D Extractor. This method was briefly explained in Appendix A.

Figure 3.3 shows how the effective relative dielectric constant of single-ended line depends on the number of divided lines m when the line width $w = 0.3$ mm, angle $\phi = 45°$, and wiring length $l = 9.6$ mm. When m was almost 100, the effective relative permittivity value converged. Also, the effective relative dielectric constant value converged at almost 100 even with different line widths. Therefore, in this paper, m is 101 when the line width is considered.

Table 3.1 Structural parameters and relative permittivities for preliminary evaluation.

Item	Value	Unit
w	0.3	mm
s_{c}	0.5	mm
a	0.21	mm
b	0.64	mm
t	0.035	mm
h	0.045	mm
ε_{r}	3.3	-
$\varepsilon_{\mathrm{reff1}}$	3.0	-
$\varepsilon_{\mathrm{reff2}}$	1.3	-

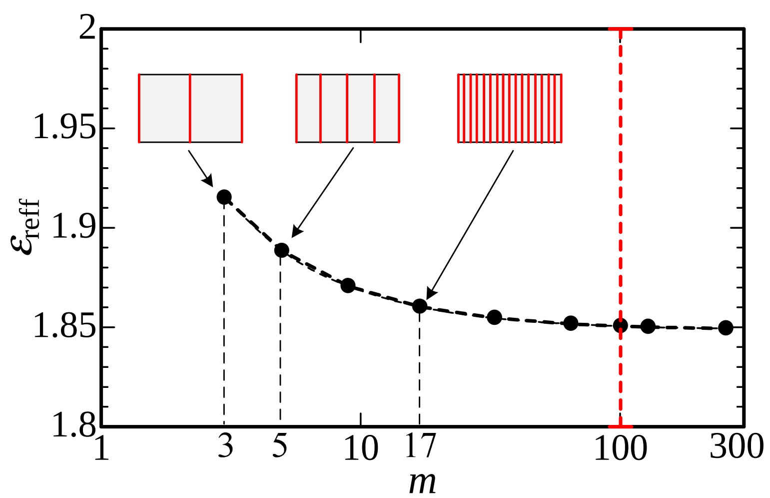

Figure 3.3 Effective relative permittivity as a function of m

3.3 Preliminary Evaluation using Simple Model for Meshed Ground

In this section, first, we evaluate the angular dependence of the differential skew when the line width is not considered and when the line width is considered.

3.3.1 Effect of Rotation Angle on Differential Skew

For evaluating the differential skew, the propagation time difference between a pair of the differential transmission lines ΔT, and the mode conversion amount of mixed-mode S parameters, $|S_{\mathrm{cd21}}|$, are generally used [35, 40]. The propagation time difference ΔT is given as

$$\Delta T = \frac{1}{\omega}\Delta\theta \tag{3.8}$$

and has the relationship with $|S_{\mathrm{cd21}}|$ given by

$$\Delta T = \frac{2}{\omega}\sin^{-1}|S_{\mathrm{cd21}}|. \tag{3.9}$$

Figures 3.4(a) and 3.4(b) show the difference in the angle ϕ dependency between the differential skew line and the mesh ground from 0° when the line width is not considered and when the line width is considered. It is shown in the range of 45°. The rotation angle ϕ at this time is when the differential wiring is rotated around the point B shown in Fig. 3.2(b) and Fig. 3.2(c), and the wiring length l at this time is 30 mm. Regardless of whether or not the line width is considered, ΔT decreases as the angle ϕ increases, and the angle between the mesh ground and the wiring is the smallest in the range of 30° to 40°.

This is because, in asymmetric structures, when the rotation angle ϕ is 0 or 45° (Fig. 3.2), and a phase difference between Line #1 and Line #2 exists at every mesh pitch, differential skew ΔT increases monotonically with line length l. This is because the same phase difference accumulates at each mesh pitch. This is also true when ϕ is 26.5°. However, at any other angle, the phase difference at the first mesh pitch is different from that at the next mesh pitch. This is because the different lines pass relatively randomly over the mesh and the separating space between meshes with different effective relative dielectric constants. Therefore, ΔT increases and decreases periodically with l. As ϕ becomes larger, the magnitude of the periodic increase and decrease becomes smaller.

As shown in Figs. 3.4(a) and 3.4(b), ΔT suddenly takes a large value at several rotation angles ϕ, which are 18.4°, 26.5°, in the order of increasing angles, in addition to 0° and 45° mentioned earlier. Using an integer ν which is greater than or equal to 2, the rotation angle ϕ is expressed as

$$\phi = \tan^{-1}\left\{\frac{(a+b)}{\nu(a+b)}\right\} = \tan^{-1}\left(\frac{1}{\nu}\right) \tag{3.10}$$

As shown in Fig. 3.4, $\phi = 45°$ when $\nu = 1$, and $\phi = 26.5°$ when $\nu = 2$ etc..

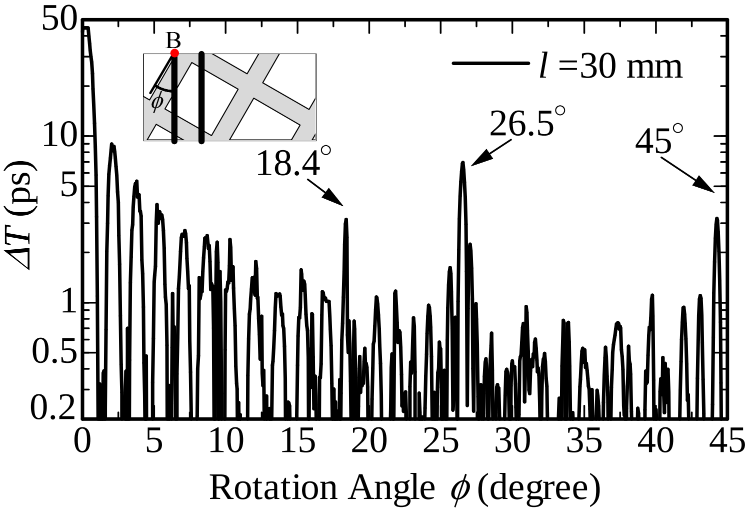

(a) Line width is not considered

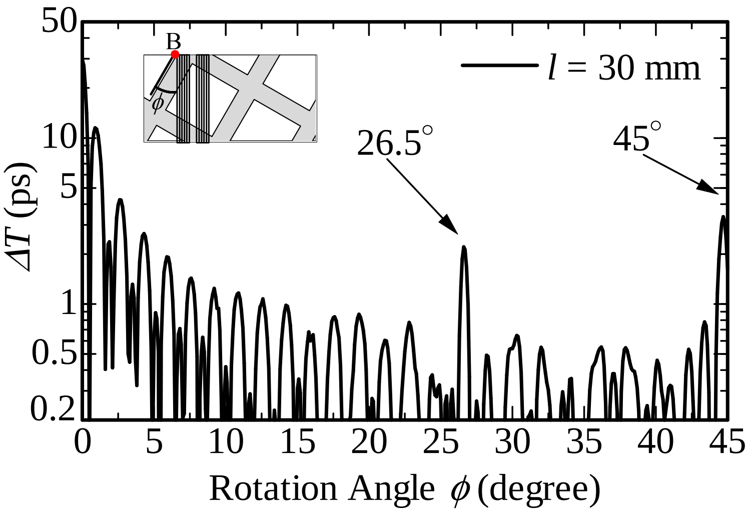

(b) Considering line width

Figure 3.4 Evaluation of propagation time difference $\varDelta T$ between lines by angle dependence.

3.3.2 Effect of Line Length on Differential Skew

Next, when the line width is taken into account, the dependence of $\varDelta T$ on the wiring length l is evaluated. In four different rotation angles ϕ between the meshed ground and the lines is 26.5, 30, 40, and 45°, the calculation was performed by changing l in the range of 0.1 to 30 mm at the same interval of 0.1 mm, and the dependency of $\varDelta T$ on the line length l was investigated. Figure 3.5 shows the results.

At 0° and 45°, $\varDelta T$ monotonically increases with the line length l. This is because the phase difference between Line #1 and Line #2 exists at every weave pitch, as described earlier. At 26.5°, when ν is equal to 2 in (3.10), $\varDelta T$ increases with the line length l, increasing and decreasing periodically. This is because the difference of the phase change

$\Delta\theta$ takes the same value once every ν times of the weave pitch.

At 10° and 40°, ΔT fluctuates but does not increase. This is because the change is not exactly periodic, so ΔT takes a random value in every portion. Since the average value approaches 0, ΔT does not increase even if the line length is extended.

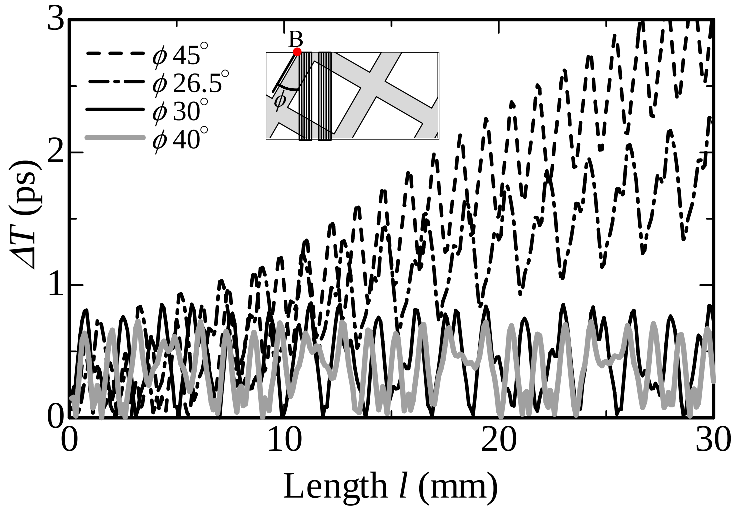

Figure 3.5 Wiring length l dependence with line width considered

3.3.3 Effect of Line position on Differential Skew

In the above, the angle dependence and wiring length dependence when a single point (point B in Fig. 3.2) is the center were evaluated. Next, the position dependence of the line is evaluated. Specifically, using the parameters shown in Table 3.1, Fig. 3.2 shows the case where the mesh ground is rotated in two ways of 45° and 30° for differential wiring with a wiring length l of 9.6 mm. The point B shown in Fig. 3.2 was the origin, and the distance was changed from 0 mm to 1 mm as shown in Fig. 3.6. Figure 3.7 shows the results. Since there are two types of ground mesh at this time, the solid line in the graph in Fig. 3.7 shows the case of a simple model that considers the line width. On the other hand, the marks (■, ▲) were the average value of ΔT obtained by Eq. (3.9) using the mode conversion amount $|S_{\text{cd21}}|$ in the frequency range of 0.1 to 10 GHz obtained using the commercially available 3D electromagnetic field simulator ANSYS HFSS. The calculation area at this time was $L_x = 7.2$ mm and $L_y = 9.6$ mm in Fig. 3.1(a), and the position dependence was evaluated at 10 locations in the range the distance was changed from 0 mm to 1 mm from point B. From Fig. 3.7, it can be seen that a result close to the electromagnetic simulation result can be obtained by considering the line width. Also, it can be seen that the differential skew does not depend much on the position of the differential transmission lines and mesh ground at 30° compared to 45°, and is relatively small.

(a) B position (b) 1 mm from B

Figure 3.6 Line position in simple model with width.

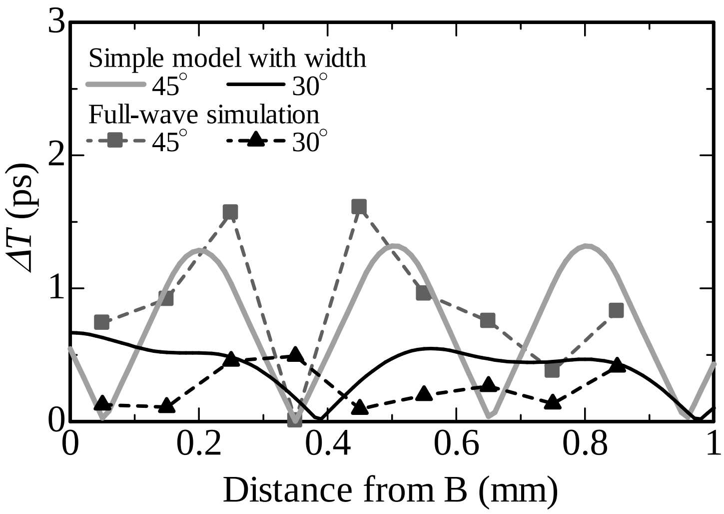

Figure 3.7 Line position dependence

3.4 Rotating Meshed Ground for High-density Mounting in FPCs

In Section 3.3, we evaluated the differential skew caused by the meshed ground in detail using the simple model and full-wave simulation. To examine the generality of the proposed bend structure, the structures with the different structural parameters from the previous discussion were fabricated, and the mode conversion (differential skew) and differential-mode characteristics were evaluated through full-wave simulation and measurement.

In this section, we built two sets of FPC test boards. Our first set of test boards were built to examine mode conversion (differential skew), differential-mode characteristic impedance, and differential-mode transmission characteristics. Our second set of test boards were built to evaluate the differential-mode transmission characteristics of the differential transmission lines, including bending, to test the feasibility of high-density mounting.

3.4.1 FPC Test Board for Measurement

Figure 3.8 shows the configuration of the FPC test board used in this paper; w is the line width, s is the distance between the lines L1 and L2, and a and b indicate the width of the mesh and the separating space between meshes, respectively. The dimensions w, s, a, and b shown in Fig. 3.8 are the structural parameters used in this section. These metal widths and spaces are generally easy for FPC manufacturers to make. Table 3.2 shows the thickness, relative dielectric constant (Dk), and dielectric loss (Df) of each layer material in our FPC test board. Using the above parameters, the differential-mode characteristic impedance was close to 100 Ω.

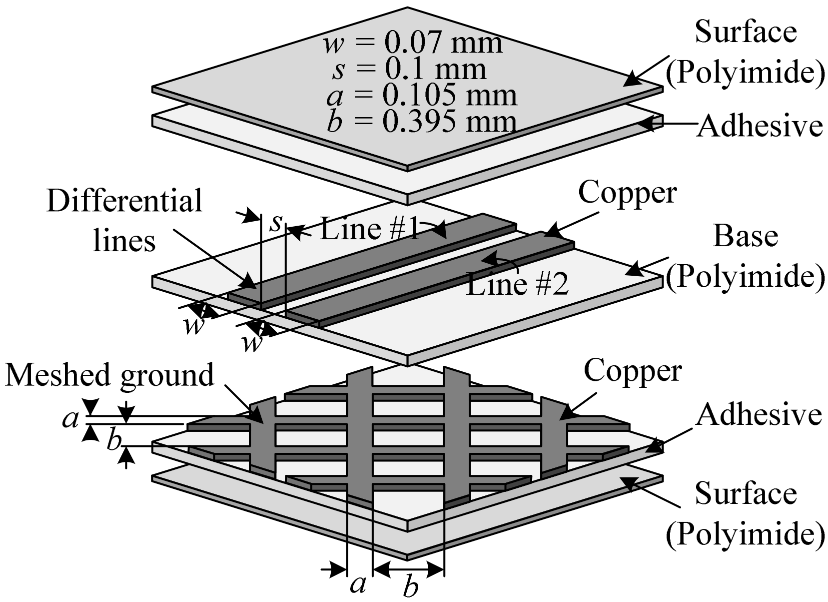

Figure 3.8 Structure of test board.

In asymmetric structures, when the rotation angle ϕ is 0 or 45° (Fig. 3.8), and a phase difference between Line #1 and Line #2 exists at every mesh pitch, differential skew ΔT increases monotonically with line length l. This is because the same phase difference accumulates at each mesh pitch. This is also true when ϕ is 26.5°, as mentioned earlier in this chapter. However, at any other angle, the phase difference at the first mesh pitch is different from that at the next mesh pitch. This is because the different lines pass relatively randomly over the mesh and the separating space between meshes with different effective relative dielectric constants. Therefore, ΔT increases and decreases periodically with l. As ϕ becomes larger, the magnitude of the periodic increase and decrease becomes smaller, as mentioned earlier in this chapter.

Table 3.2 Structural parameters of test board for measurement.

Construction	Thickness (μm)	Dk	Df
Surface (Polyimide)	12.5	3.4	0.007
Adhesive	25	3.3	0.025
Copper	15	-	-
Base (Polyimide)	25	3.2	0.005
Copper	15	-	-
Adhesive	25	3.3	0.025
Surface (Polyimide)	12.5	3.4	0.007

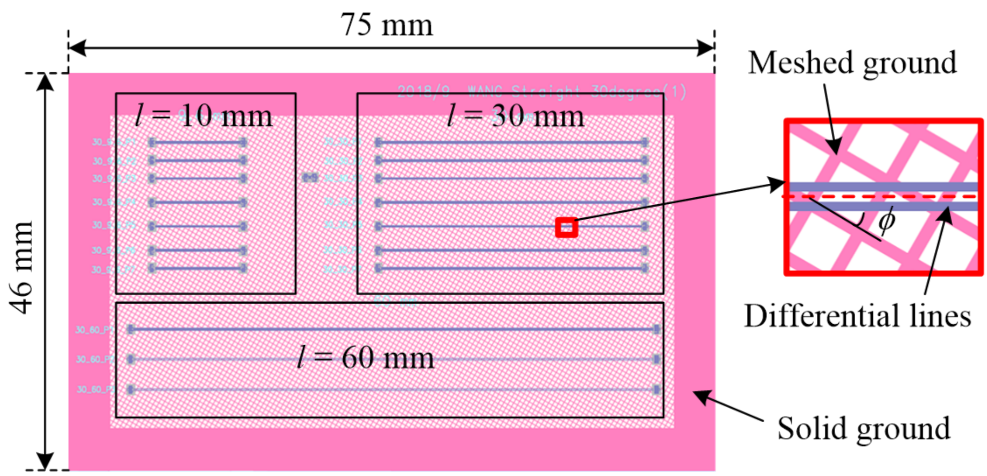

Figure 3.9 First set of test boards to measure differential skew (Example).

With this in mind, our first set of test boards, depicted in Fig. 3.9, was built to study the differential skew induced by the meshed ground. To measure how the rotation angle affected the differential skew ΔT, we measured seven different rotation angles ϕ, 0, 10, 22.5, 26.5, 30, 40, and 45°. To measure how line length affected ΔT, we measured three different line lengths l, 9.6, 30, and 60 mm. We also wanted to evaluate the effects of line position, but although the relationship between meshed ground and line position can be controlled at the time of fabrication, the worst positions for differential skew and characteristic impedance are different. For this reason, to evaluate how line position affects differential skew and characteristic impedance, at least 3 positions are required including the best (symmetrical) position. Therefore, the 60 mm long differential transmission lines have patterns of three different positions, and the 9.6 and 30 mm long differential transmission lines have patterns of seven different positions including additional four positions in the first set of test boards.

Our second set of test boards, depicted in Fig. 3.10, was built to investigate whether or not high-density mounting is possible when the rotation angle is set to 30°. However, the 45° bend that is usually used in wiring does not always keep the angle of the meshed ground in relation to the lines at 30°. A 90° bend, however, can always keep the angle at 30°. Therefore, the bend angles of 90° were used for the rotation angle of 30°.

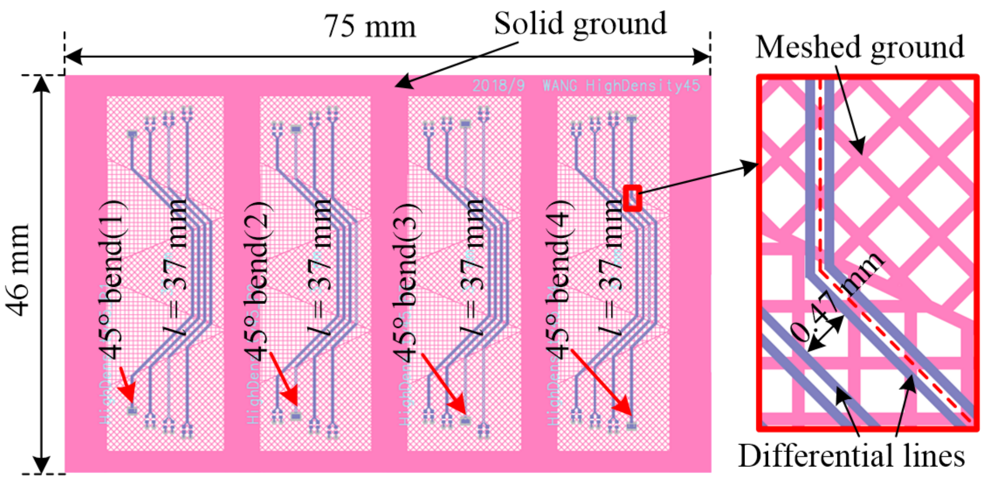

(a) FPC1

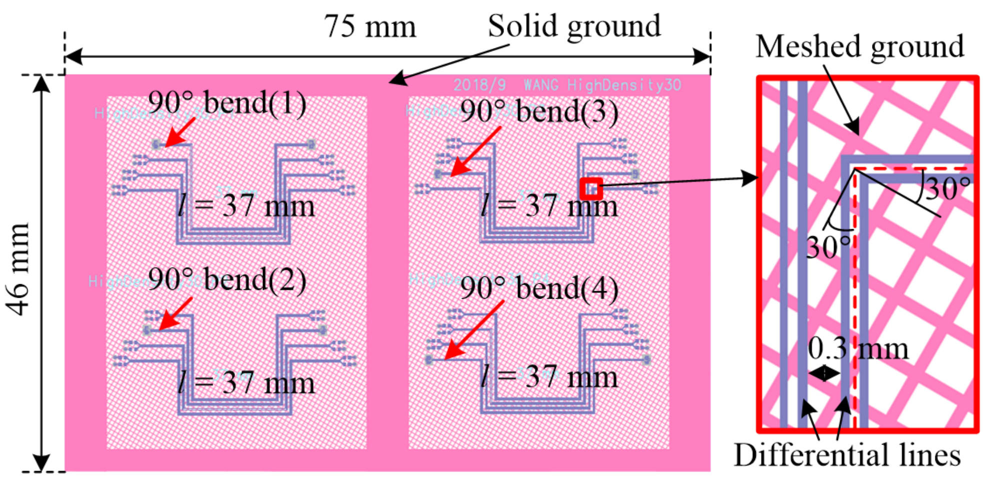

(b) FPC2

Figure 3.10 Second set of test boards to measure transmission characteristics.

Figure 3.10(a) shows a general board design with 45° bend differential transmission lines and a meshed ground. With this design, all lines can be placed symmetrically. However, the wiring density is still dependent on the mesh structure. With the dimensions in Fig. 3.8, the minimum distance between adjacent differential transmission lines is 0.47 mm in FPC1.

Figure 3.10(b) shows our proposed design. First, the meshed ground is rotated by 30°, and a 90° bend is used for the reasons given above. In this design, as shown in FPC2, the minimum distance between adjacent differential transmission lines is reduced to 0.3 mm. Note that optimizing the interval between adjacent differential transmission lines is not the purpose of this study, but generally, the interval is set to about three times the value of s to suppress crosstalk.

Table 3.3 Evaluation item of test boards.

Test boards	Differential skew	Characteristic impedance	Transmission characteristics
First set	○	○	-
Second set	-	-	○

The length of all the differential transmission lines in FPC1 and FPC2 was set to 37 mm. The red arrows indicate the lines used for measurement; all the unmeasured lines were matched by chip resistance of 50 Ω. Table 3.3 summarizes the evaluation item of two sets of FPC test boards.

Effect of Rotation Angle on Differential Skew

Figure 3.11 shows the effect of the angle between the trace of the differential transmission lines and the meshed ground (rotation angle) ϕ on $\varDelta T$, obtained by calculating the arithmetic average of $\varDelta T$ for the whole frequency of 0.1 to 10 GHz.

Figures 3.11(a), (b), and (c) show the effect of ϕ on $\varDelta T$ in the range from 0 to 45°, when the line length l is 9.6, 30, and 60 mm, respectively.

In Fig. 3.11(a), the red square and the rhombus represent the simulation and measurement values, respectively. The simulation values correspond to the case when $\varDelta T$ takes the largest value (the worst case) when the position of the differential transmission lines over the meshed ground plane is changed. The figure indicates that $\varDelta T$ decreases with ϕ and that it takes its smallest value at around $\phi = 30°$.

As shown in Figs. 3.11(b) and 3.11(c) and mentioned earlier, $\varDelta T$ takes a large value when ϕ is 0, 26.5, and 45°. In addition, it takes the smallest value at around $\phi = 30°$ regardless of the line length.

We use mixed-mode S parameters to evaluate differential skew, characteristic impedance, and transmission characteristics. To obtain mixed-mode S parameters, we conducted 4-port measurement using a vector network analyzer (KEYSIGHT E5071C). We also used a pair of 200-μm-pitched GSGSG microprobes (Cascade Microtech ACP-40-D-GSGSG), with which the propagation characteristics of the test boards were measured at frequencies ranging from 0.1 to 20 GHz.

Effect of Line Length on Differential Skew

Figure 3.12 shows how the differential skew $\varDelta T$ is affected by the line length l, ranging from 9.6 to 60 mm, for four different rotation angles ϕ, 22.5, 26.5, 30, and 45°.

We evaluated $\varDelta T$ occurring at l of 10, 30, and 60 mm using the positional relationship of the differential transmission lines and the meshed ground in the previously described

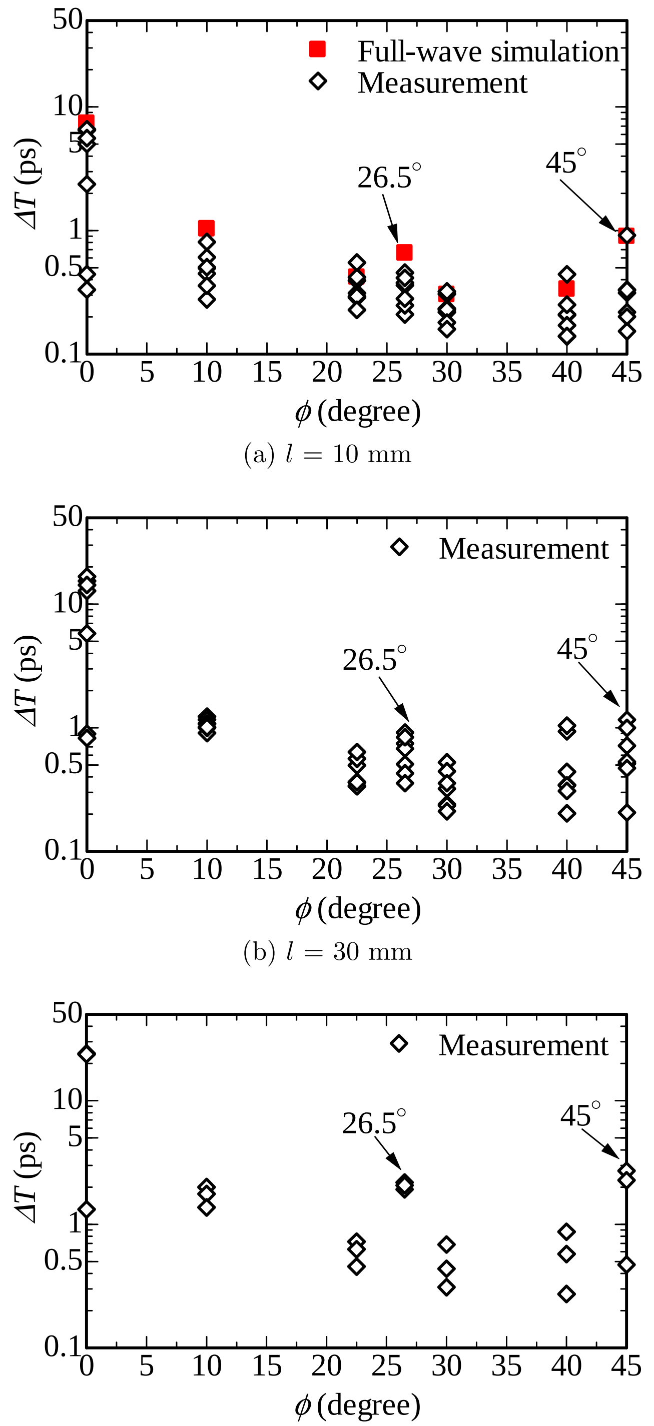

(a) l = 10 mm

(b) l = 30 mm

(c) l = 60 mm

Figure 3.11 Effect of rotation angle ϕ on differential skew ΔT for different line lengths l.

worst case. In particular, at 26.5 and 45°, the differential transmission lines of three different lengths are placed in the position shown in Fig. 3.12. At 26.5 and 45°, ΔT monotonically increases with l. This increasing tendency is caused by the accumulation

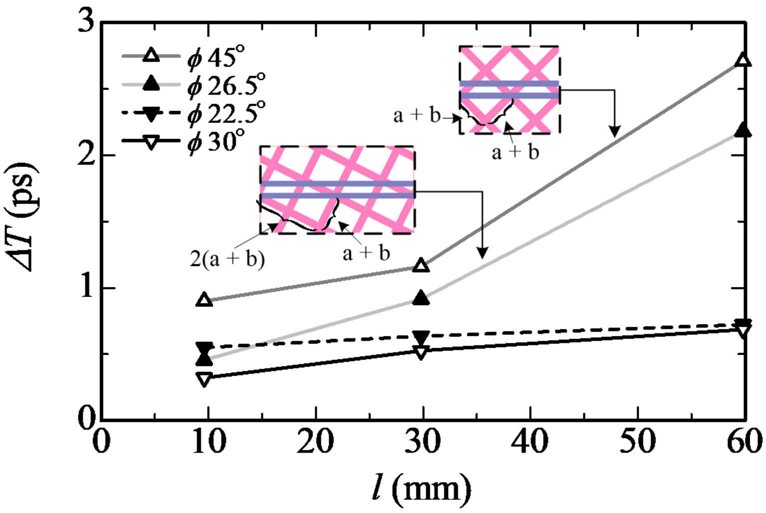

Figure 3.12 Effect of line length l on differential skew ΔT.

of the same phase difference. As shown in Fig. 3.12, $\phi = 45°$ when $\nu = 1$, and $\phi = 26.5°$ when $\nu = 2$. At 22.5 and 30°, ΔT fluctuates but does not increase. This is because the change is not exactly periodic, so ΔT takes a random value in every portion. The average value approaches 0, so ΔT does not increase even if l is extended.

Relationship Between Rotation Angle and Characteristic Impedance

In our analysis, we focus only on the differential-mode characteristic impedance. The effective differential-mode characteristic impedance Z_d was calculated using the S parameters and mixed-mode ABCD parameters [74, 75].

First, S parameters are obtained from the 9.6-mm differential transmission lines in our first set of test boards. Then, the mixed-mode ABCD parameters of this structure can be determined using S parameters [75].

Z_d of the differential transmission lines can be calculated from its mixed-mode ABCD parameters

$$Z_\mathrm{d} = \sqrt{\frac{B_\mathrm{d}}{C_\mathrm{d}}}, \tag{3.11}$$

where B_d is differential-mode B-parameter and C_d is differential-mode C-parameter.

Then, using the maximum and minimum values of Z_d obtained from different line positions, the relationship between the rotation angle and amount that the characteristic impedance changes is evaluated.

Figure 3.13 shows the maximum and minimum values of measured Z_diff for seven rotation angles. When the rotation angle is 0 or 45°, the characteristic impedance changes significantly depending on the arrangement of the wiring and meshed ground, but the change is small in the range of 10 to 40°. Further, around 30°, Z_d was scarcely affected

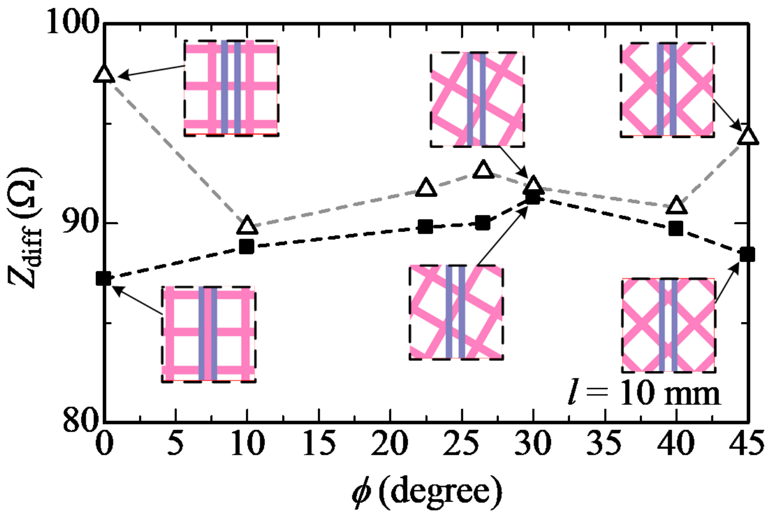

Figure 3.13 Relationship between rotation angle ϕ and differential-mode characteristic impedance Z_d.

by the wiring-and-ground position.

3.4.2 Differential-Mode Transmission Characteristics

In the previous section, the differential skew $|S_{cd21}|$ and the effective differential-mode characteristic impedance Z_d were evaluated. Here, using 60 mm long differential transmission lines, we evaluate the rotation angle $\phi = 0$, 45, (the symmetrical structures) and 30° (the worst case) with regard to differential mode.

Figure 3.14(a) first shows the differential-mode transmission coefficients. The differential-mode transmission coefficient of $\phi = 30°$ is larger than those of $\phi = 0$ and 45°. This is because $\phi = 30°$ suppresses differential-to-common mode conversion (Fig. 3.11) and the differential-mode reflection compared to $\phi = 0$ and 45°.

Next, the transmission characteristics of $\phi = 0$, 30, and 45° are evaluated with regard to phase. Note the group delay obtained from the phase characteristic of S_{dd21}.

The group delay time obtained by Eq. (2.17) is shown in Figs. 3.14(b), (c), and (d). These results show that T_g for when $\phi = 30°$ has almost the same characteristics as the symmetrical structures have. As a result, the structure takes the smallest distortion in the output waveform at $\phi = 30°$, and the signal can be successfully transmitted. This means that $\phi = 30°$ structure is comparable to the symmetrical structures in terms of the differential-mode transmission.

Finally, we evaluate our second set of test boards, shown in Fig. 3.9. Figure 3.15 and 3.16 shows the differential-to-common mode conversion $|S_{cd21}|$ and differential-mode characteristics of $|S_{dd11}|$ and $|S_{dd21}|$ as a function of frequency for test boards FPC1 and FPC2.

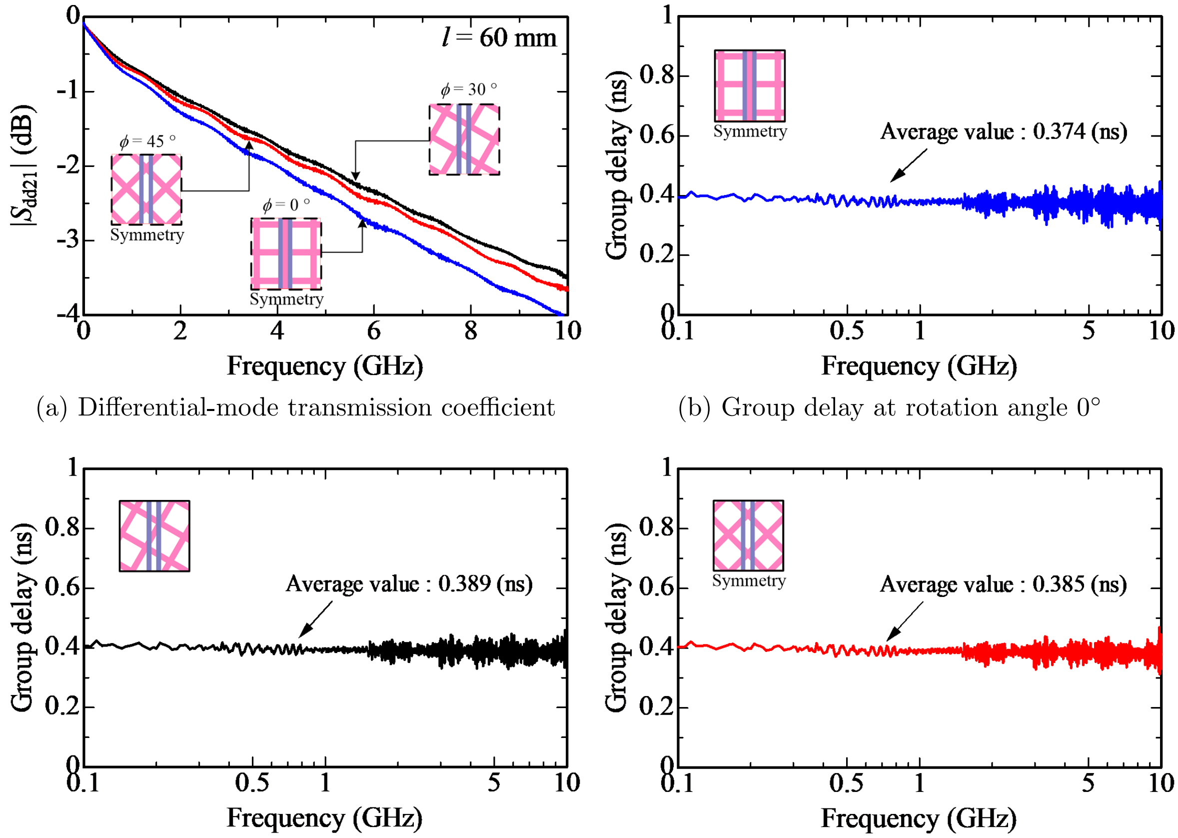

(a) Differential-mode transmission coefficient

(b) Group delay at rotation angle 0°

(c) Group delay at rotation angle 30°

(d) Group delay at rotation angle 45°

Figure 3.14 Comparison of transmission characteristics.

The following three points are clear from Fig. 3.15 and 3.16. First, $|S_{\mathrm{cd21}}|$ of FPC1 and FPC2 became less than -30 dB when frequency below 15 GHz. This shows that $|S_{\mathrm{cd21}}|$ for FPC2 is not dependent on the position of the differential transmission lines relative to the pattern of the meshed ground and comparable to that for FPC1. Second, the position dependence of the differential-mode reflection $|S_{\mathrm{dd11}}|$ for FPC2 is small compared to FPC1. This is because FPC1 demands high symmetry, and it is challenging to arrange the wiring and the meshed ground completely symmetrically in actual production. Third, the differential-mode transmission coefficient $|S_{\mathrm{dd21}}|$ of FPC2 is comparable but larger than that of FPC1. This is the same reason as $|S_{\mathrm{dd11}}|$, that is the small position dependence in FPC2.

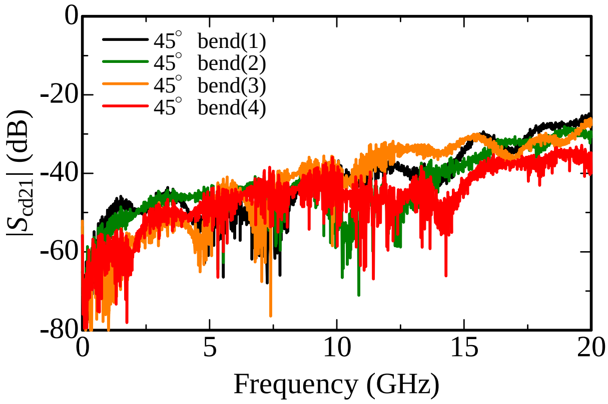

(a) Mode conversion

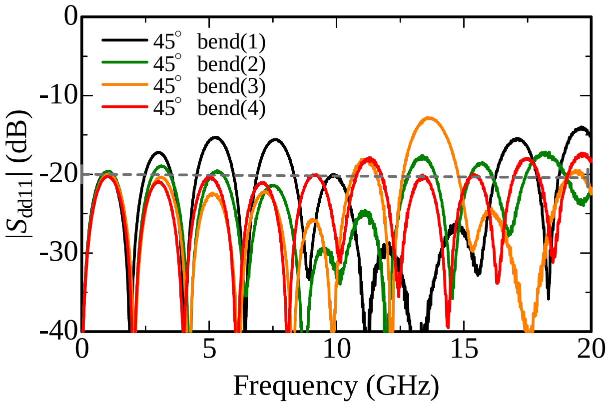

(b) Reflection coefficient

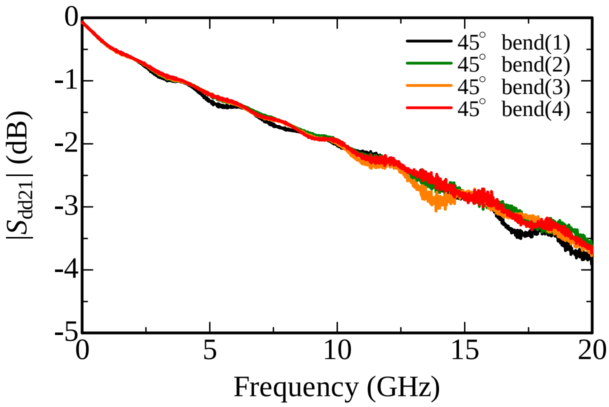

(c) Transmission coefficient

Figure 3.15 FPC1

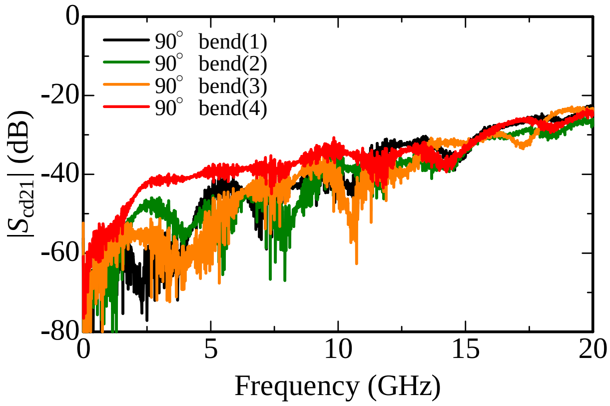

(a) Mode conversion

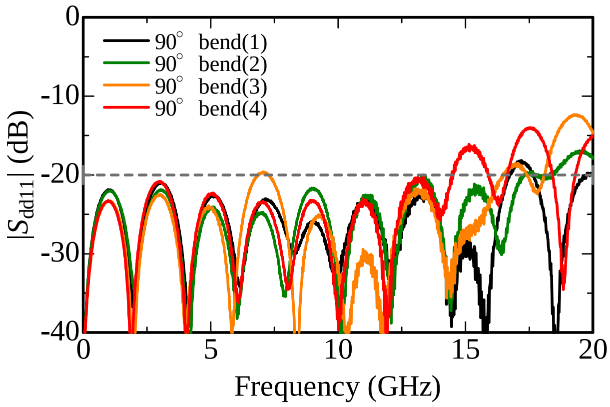

(b) Reflection coefficient

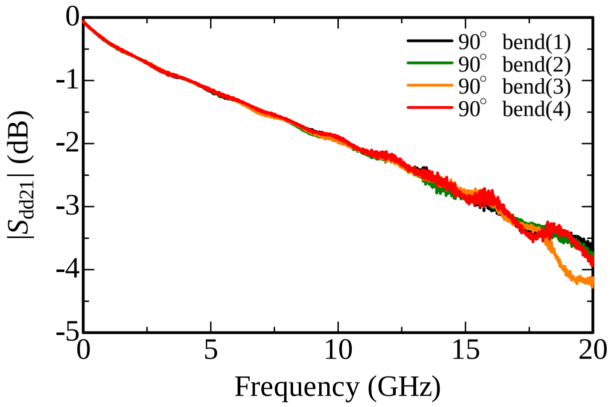

(c) Transmission coefficient

Figure 3.16 FPC2

3.5 Randomly Shifted Mesh Position of Meshed Ground

We previously showed that the rotated meshed ground keeps the differential skew small by making the phase difference between the two lines irregular at each mesh pitch. In this section, we also show that the irregular phase difference by shifting the mesh position randomly does not affect the characteristic impedance nor differential skew in terms of the wiring position.

Figure 3.8 and Table 3.2 shows the cross section of our FPC test vehicles and the thickness, the relative dielectric constant (Dk), and the dielectric loss (Df) of each layer. Figure 3.17(a) shows the conventional meshed ground structure, and a indicates the width of the mesh while b indicates the separating space between the meshes. The mesh pitch $a + b$ is 0.5 mm, and 140 columns of the mesh are placed in the horizontal direction.

We designed the randomly meshed ground by vertically shifting each column of the mesh randomly shifted from the reference line (the broken line), as shown in Fig. 3.17(b). The five shift amounts of 0, 0.1, 0.2, 0.3, and 0.4 mm were determined by pseudorandom numbers with five values. In addition, the adjacent pseudorandom numbers are not the same value.

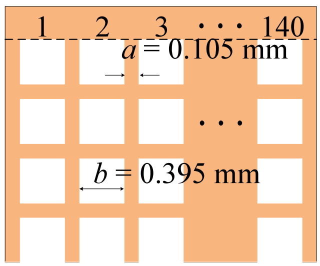

(a) Conventional meshed ground

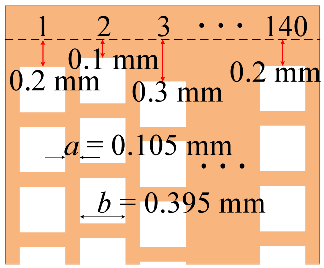

(b) Randomly meshed ground

Figure 3.17 Conventional meshed ground and randomly meshed ground.

Figure 3.18 shows four test vehicles with the same differential transmission lines, with l = 10 mm, $w = 0.07$ mm, and $s = 0.1$ mm. Figs. 3.18(a) and 3.18(b) show the conventional meshed ground structure at rotation angles of 0° and 45° to the differential transmission lines, respectively. Figs. 3.18(c) and 3.18(d) show the randomly shifted mesh ground structure at rotation angles of 0° and 45°, respectively. To investigate how the wiring position affects the characteristic impedance and the differential skew, seven wiring positions were set with the same interval in the direction of red arrow, as shown in Fig. 3.18.

To obtain the characteristic impedance Z_{d} and the differential skew ΔT by using S parameters, 4-port measurements were conducted with a vector network analyzer (KEYSIGHT E5071C). Fig. 3.19(a) shows the relationship between Z_{d} and the four test vehicles. The results show that the difference between the maximum and minimum Z_{d} of (c) and (d) is approximately five times smaller than that of (a) and (b). Fig. 3.19(b) shows the rela-

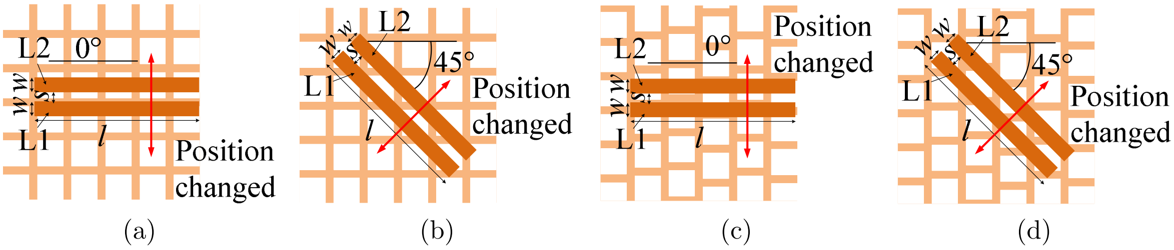

Figure 3.18 Four test vehicles treated.

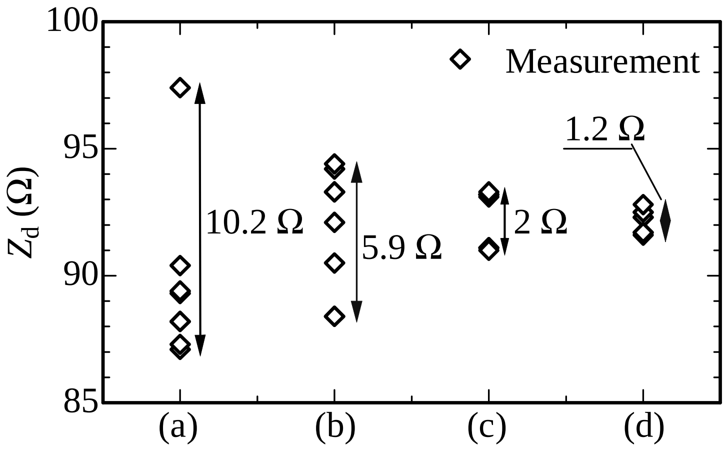

(a) Change in Z_d

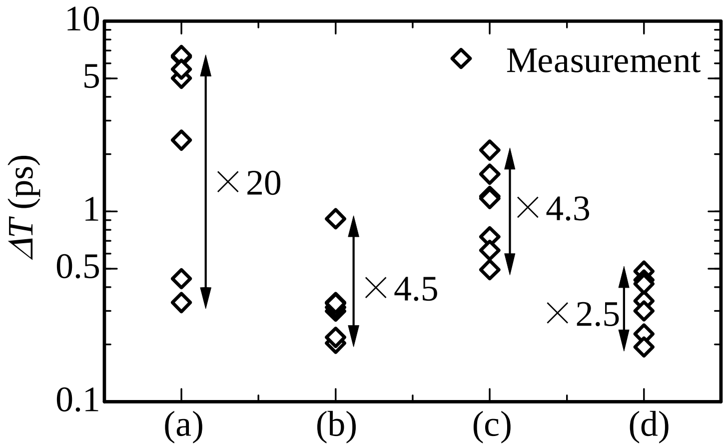

(b) Change in $\varDelta T$

Figure 3.19 Differential characteristic impedance and differential skew.

tionship between $\varDelta T$ and the four test vehicles. Similarly, $\varDelta T$ of (c) and (d) had smaller changes than that of (a) and (b) in terms of the wiring position on meshed ground. These results suggest that the randomly shifted meshed ground was not sensitive to the position of differential lines compared to the conventional one.

3.6 Conclusion

We described a simple model to evaluation differential skew caused by meshed ground, which leads to the differential-to-common mode conversion and achieved very low levels of differential skew by rotating the meshed ground.

We found that the differential skew is not affected by the position of the differential transmission lines relative to the pattern of the meshed ground and that it takes its minimum value when the rotation angle is around 30°. Through the evaluation of the transmission coefficient, we found that the structure with the rotation angle $\phi = 30°$ is comparable with the symmetrical structures in which $\phi = 0$ and 45° in terms of the differential-mode transmission.

We also proposed a design wherein the meshed ground is rotated by 30° with a 90° bend in the differential transmission lines. We compared this design with a general design that has 45° bend differential transmission lines and meshed ground. Our proposed design is unaffected by the position of the lines relative to the meshed ground, enabling improved wiring density. Further, our design is better for the differential-mode transmission characteristics than the general design, which demands high symmetry. From the above results, it is found that the rotated meshed ground keeps the differential skew small by making the phase difference between the two lines irregular at each mesh pitch.

In this chapter, we also show that the irregular phase difference by shifting the mesh position randomly does not affect the characteristic impedance nor differential skew in terms of the wiring position.

Chapter 4

Suppression Method of Crosstalk in Adjacent Differential Transmission Lines

4.1 Introduction

In recent years, with increasing frequencies and PCBs size reduction which leads to increased differential trace density. The electromagnetic coupling between the adjacent differential pairs becomes strong, which causes a problem of crosstalk, it is one of the most critical SI and EMI issues [11, 49, 58], well known by high-speed PCB designers. Generally speaking, the distance between the line pairs should be taken rather wider than the differential-line spacing for crosstalk suppression, but it is difficult to keep the rule with high-density wiring. Conversely, As the distance d_c between the center lines of the adjacent differential pairs, as shown in Fig. 4.1(a), is reduced and the rise times of digital signals become shorter, crosstalk becomes a more severe problem. It generates additional delays, skews, jitters, or false switching of digital logic, degrading the noise margin and the timing margin of the system [11, 58].

Many design methods or recommendations have been proposed and established to help suppress or minimize the effects of crosstalk between adjacent transmission pairs such as a ground trace in putting between adjacent differential pairs [59], a twisted differential line structure [60], etc. However, it is difficult to apply next-generation high-speed signal transmission because these structures are difficult to keep the high-density wiring or too complicated.

The periodic rectangular structure had been so far proposed to suppress crosstalk between the differential microstrip lines and the single-ended microstrip line [76]. In [77, 78], as shown in Fig. 4.1(b), the adjacent differential pairs with a periodic rectangular structure are proposed, and their propagation characteristics were evaluated. However, the reduction mechanism of crosstalk between adjacent differential pairs with periodic structure has been left unclear.

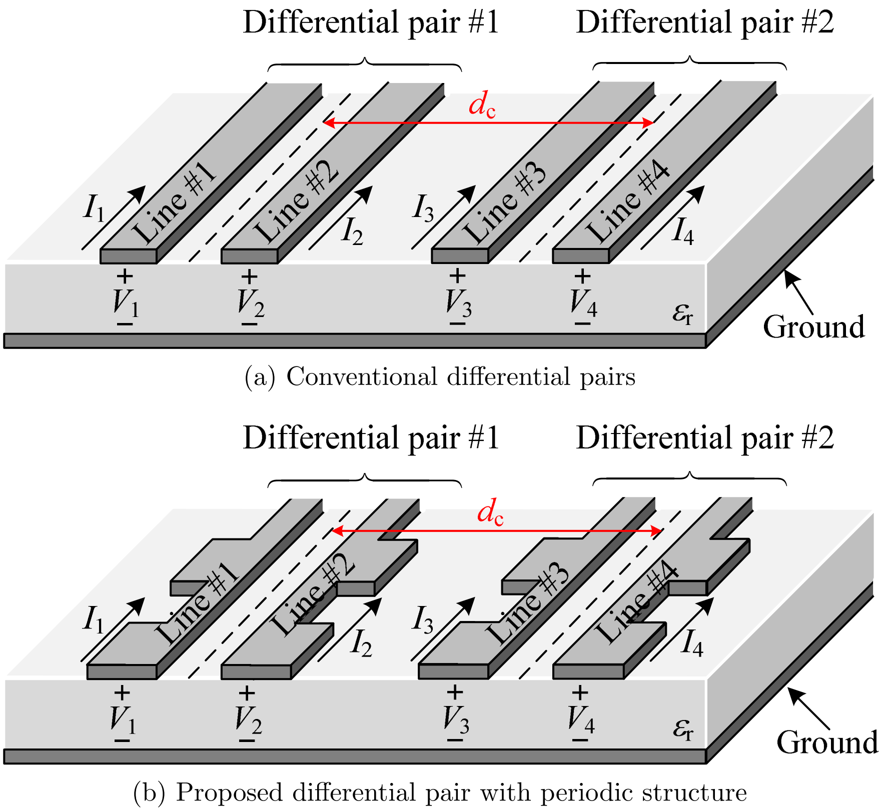

Figure 4.1 Overview of two kinds of differential pairs.

In [80] have reviewed theories for crosstalk between a pair of uniform microstrip transmission lines and have simplified the theory to easily computed formulas for near-end crosstalk (NEXT) and far-end crosstalk (FEXT). These theories formulas require values for the even- and odd-mode characteristic impedances and the effective dielectric constant for the even- and odd-modes and the isolated strip. It is clear that NEXT greatly depends on the difference between the even- and odd-mode characteristic impedances, and FEXT greatly depends on the difference between the even- and odd-mode effective dielectric constants. However, have an unsolved problem, namely, expand the crosstalk theory to computed for differential-mode crosstalk between neighboring differential pairs.

We can use a modal equivalent circuit created applying the mode-decomposition technique to the telegrapher's equations for analyzing a multiconductor transmission-line system. As long as the simplifying assumptions in weakly coupled and weak imbalance are satisfied, the DM is not influenced by the other modes and allows the modal equivalent circuit interpretation. And, the results obtained from the circuit simulation using the modal equivalent-circuit model were in good agreement with those obtained from full-wave simulation and measurement [82]. However, the modal equivalent circuit doesn't make it clear how the even- and odd-mode characteristic impedances and the effective dielectric constant change between neighboring differential pairs.

In this chapter, we focus only on the differential modes (DMs) of the adjacent differential pairs, and the mechanisms of crosstalk occurring in adjacent differential pairs were investigated by combining modal analysis, multi-conductor transmission line theory, and the simplifying assumptions of weak coupling. For discussion DM crosstalk of the 5-conductor transmission line, we proposed the concept of odd- and even-mode DMs by referring to [58]. According to the classical coupled transmission line theory, we can use the approximate solution of [79, 80] and equate NEXT and FEXT of DM to the mixed-mode S parameters. And using computed formulas for NEXT and FEXT in DM to investigate the reduction mechanism of DM crosstalk of the differential pairs with a periodic structure, as shown in Fig. 4.1(b).

4.2 Multiconductor Transmission Lines Under Analysis

In this section, we focus on the 5-conductor transmission system, as shown in Fig. 4.1(a), and the mechanisms of crosstalk occurring in adjacent differential pairs were investigated by combining modal analysis, multi-conductor transmission line theory, and the simplifying assumptions of weak coupling.

4.2.1 Per-Unit-Length Parameters and Modal Analysis

The PCB structure in Fig. 4.1(a) is modeled as a uniform and lossless 5-conductor transmission lines (4-conductor transmission lines and the ground as reference conductor), We assume the conductor is close enough to each other, and only TEM modes propagate along the transmission line. Due to medium in-homogeneity, analysis of the corresponding per-unit length (p.u.l.) inductance and capacitance parameters are carried out by using the ANSYS 2D Extractor. This yields 4×4 p.u.l. inductance and capacitance matrices exhibiting persymmetric structure and characterized by the following symmetries among the involved entries:

$$[\boldsymbol{L}] = \begin{bmatrix} L_{11} & L_{12} & L_{13} & L_{14} \\ L_{21} & L_{22} & L_{23} & L_{24} \\ L_{31} & L_{32} & L_{33} & L_{34} \\ L_{41} & L_{42} & L_{43} & L_{44} \end{bmatrix} = \begin{bmatrix} L_{11} & L_{12} & L_{13} & L_{14} \\ L_{12} & L_{22} & L_{23} & L_{13} \\ L_{13} & L_{23} & L_{22} & L_{12} \\ L_{14} & L_{13} & L_{12} & L_{11} \end{bmatrix} \tag{4.1}$$

$$[\boldsymbol{C}] = \begin{bmatrix} C_{11} & C_{12} & C_{13} & C_{14} \\ C_{21} & C_{22} & C_{23} & C_{24} \\ C_{31} & C_{32} & C_{33} & C_{34} \\ C_{41} & C_{42} & C_{43} & C_{44} \end{bmatrix} = \begin{bmatrix} C_{11} & C_{12} & C_{13} & C_{14} \\ C_{12} & C_{22} & C_{23} & C_{13} \\ C_{13} & C_{23} & C_{22} & C_{12} \\ C_{14} & C_{13} & C_{12} & C_{11} \end{bmatrix} \tag{4.2}$$

In particular, it is worthwhile noticing that despite the four traces are identical, the self-diagonal entries-theoretically equal if the two differential transmission lines were infinitely separated each other-may slightly differ (i.e., $L_{11} > L_{22}$, $C_{11} < C_{22}$) due to close proximity between the inner traces.

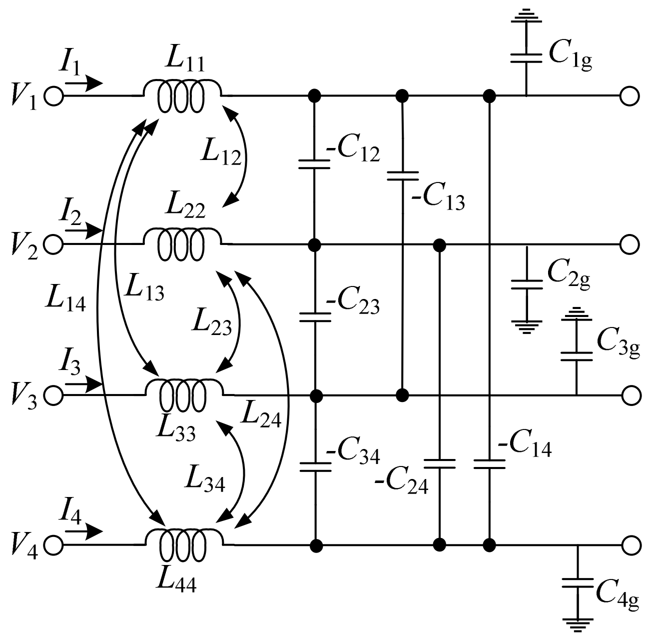

Figure 4.2 Equivalent circuit of of Fig. 4.1(a) p.u.l..

Figure 4.2 shows the equivalent circuit of Fig. 4.1(a) p.u.l.. In Fig. 4.2 assume that:

$$\begin{aligned}
C_{g1} &= C_{11} + C_{12} + C_{13} + C_{14}, \\
C_{g2} &= C_{21} + C_{22} + C_{23} + C_{24}, \\
C_{g3} &= C_{31} + C_{32} + C_{33} + C_{34}, \\
C_{g4} &= C_{41} + C_{42} + C_{43} + C_{44}.
\end{aligned} \tag{4.3}$$

Figure 4.1(a) can be expressed by using the cascade connection of a unit shown in Fig. 4.2. The results obtained from the circuit simulation using this equivalent-circuit model were in good agreement with those obtained from full-wave simulation as long as the TEM-mode propagation was satisfied. However, the differential-mode crosstalk can not be analyzed directly. We can use a modal equivalent circuit created applying the mode-decomposition technique to the telegrapher's equations for analyzing a multi-conductor transmission-line system [81].

For the above 5-conductor system, the differential mode (DM) and common mode (CM) quantities are introduced starting from the physical voltages and currents of the two differential transmission lines, as they were independent the one from the other.

Accordingly, the following transformation matrices are exploited [82]:

$$\begin{bmatrix} V_1 \\ V_2 \\ V_3 \\ V_4 \end{bmatrix} = [\boldsymbol{T}_{\mathrm{V}}][\boldsymbol{V}_{\mathrm{m}}] = \begin{bmatrix} 1/2 & 1 & 0 & 0 \\ -1/2 & 1 & 0 & 0 \\ 0 & 0 & 1/2 & 1 \\ 0 & 0 & -1/2 & 1 \end{bmatrix} \begin{bmatrix} V_{\mathrm{d1}} \\ V_{\mathrm{c1}} \\ V_{\mathrm{d2}} \\ V_{\mathrm{c2}} \end{bmatrix} \tag{4.4}$$

$$\begin{bmatrix} I_1 \\ I_2 \\ I_3 \\ I_4 \end{bmatrix} = [\boldsymbol{T}_{\mathrm{I}}][\boldsymbol{I}_{\mathrm{m}}] = \begin{bmatrix} 1 & 1/2 & 0 & 0 \\ -1 & 1/2 & 0 & 0 \\ 0 & 0 & 1 & 1/2 \\ 0 & 0 & -1 & 1/2 \end{bmatrix} \begin{bmatrix} I_{\mathrm{d1}} \\ I_{\mathrm{c1}} \\ I_{\mathrm{d2}} \\ I_{\mathrm{c2}} \end{bmatrix} \tag{4.5}$$

By virtue of Eqs. (4.4) and (4.5), the per-unit length inductance and capacitance matrices in Eqs. (4.1) and (4.2) can be rephrased in the modal domain as

$$[\boldsymbol{L}_{\mathrm{m}}] = [\boldsymbol{T}_{\mathrm{V}}]^{-1}[\boldsymbol{L}][\boldsymbol{T}_{\mathrm{I}}] = \begin{bmatrix} L_{\mathrm{dd11}} & -\Delta L & L_{\mathrm{dd12}} & \Delta L_{\mathrm{m}} \\ -\Delta L & L_{\mathrm{cc11}} & -\Delta L_{\mathrm{m}} & L_{\mathrm{cc12}} \\ L_{\mathrm{dd12}} & -\Delta L_{\mathrm{m}} & L_{\mathrm{dd11}} & \Delta L \\ \Delta L_{\mathrm{m}} & L_{\mathrm{cc12}} & \Delta L & L_{\mathrm{cc11}} \end{bmatrix} \tag{4.6}$$

$$[\boldsymbol{C}_{\mathrm{m}}] = [\boldsymbol{T}_{\mathrm{I}}]^{-1}[\boldsymbol{C}][\boldsymbol{T}_{\mathrm{V}}] = \begin{bmatrix} C_{\mathrm{dd11}} & -\Delta C & C_{\mathrm{dd12}} & \Delta C_{\mathrm{m}} \\ -\Delta C & C_{\mathrm{cc11}} & -\Delta C_{\mathrm{m}} & C_{\mathrm{cc12}} \\ C_{\mathrm{dd12}} & -\Delta C_{\mathrm{m}} & C_{\mathrm{dd11}} & \Delta C \\ \Delta C_{\mathrm{m}} & C_{\mathrm{cc12}} & \Delta C & C_{\mathrm{cc11}} \end{bmatrix} \tag{4.7}$$

In Eqs. (4.6) and (4.7), L_{dd11}, C_{dd11} and L_{cc11}, C_{cc11} are the per-unit length inductance and capacitance of the equivalent CM and DM 2-conductor transmission line associated with the two differential transmission lines; and ΔL, ΔC, are imbalance factors responsible for the conversion of DM1 (DM2) into CM1 (CM2), and vice versa. ΔL_{m}, ΔC_{m} are responsible for cross-mode conversion of DM1 (DM2) into CM2 (CM1), and vice versa; and L_{dd12}, C_{dd12} and L_{cc12}, C_{cc12} account for crosstalk modal coupling between the CMs (i.e., between CM1 and CM2) and the DMs (i.e., between DM1 and DM2).

4.2.2 Circuit Interpretation of Differential-Mode Crosstalk

An extensive set of numerical simulations based on exact and approximate solution of multi-conductor transmission line equations has been carried out, in order to identify the relevant phenomena responsible for mode conversion, as well as the conditions under which the p.u.l. modal matrices in Eqs. (4.6) and (4.7) can be possibly simplified.

This thesis focus only on the differential modes (DMs), and assume that the differential pair #1 excited by a pure DM source, the differential pair #2 idle, and terminal networks ideally symmetric concerning ground, it was found that the mechanisms of conversion of the excited DM1 into DM2 can be summarized as shown in principle diagram in Fig. 4.3, where the role played by the assumptions of weak coupling [84] weak imbalance [83] put in evidence. DM1 induces a nonnull DM2 on the idle differential pair #2 by modal crosstalk by matrix entries L_{dd12} and C_{dd12} in Eqs. (4.6) and (4.7).

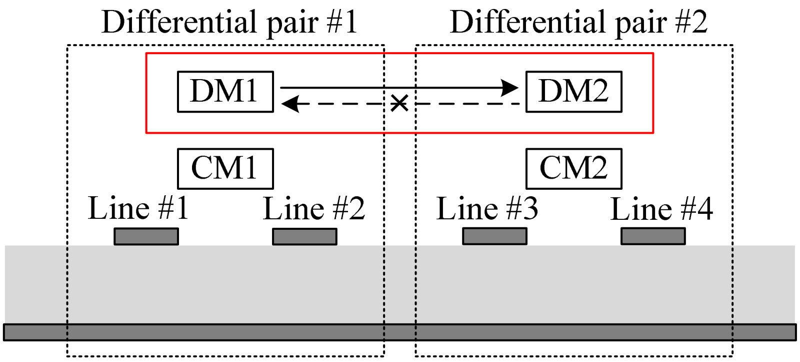

Figure 4.3 Principle diagram of the differential-mode crosstalk mechanisms (and involved simplifying assumptions) occurring in the structure under analysis

And, as long as the two DM circuits are weakly coupled, the back crosstalk of DM2 onto DM1 can be neglected [84] that is if

$$L_{\mathrm{dd12}}^2/L_{\mathrm{dd11}}^2 \ll 1, C_{\mathrm{dd12}}^2/C_{\mathrm{dd11}}^2 \ll 1. \tag{4.8}$$

As long as the simplifying assumptions in weakly coupled and weak imbalance are satisfied, the DM is not influenced by the other modes, and allow the modal equivalent circuit interpretation in Fig. 4.4 [82].

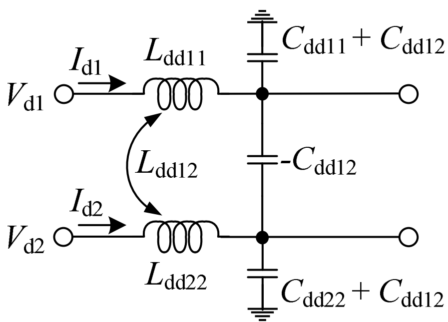

Figure 4.4 Modal equivalent circuit of differential modes in two differential pairs p.u.l..

In Fig. 4.4, each element of the modal equivalent circuits is characterized by

$$\begin{aligned} L_{\mathrm{dd11}} &= L_{11} + L_{22} - 2L_{12}, \\ L_{\mathrm{dd12}} &= 2L_{13} - L_{14} - L_{23}, \\ C_{\mathrm{dd11}} &= \frac{C_{11} + C_{22} - 2C_{12}}{4}, \\ C_{\mathrm{dd12}} &= \frac{2C_{13} - C_{14} - C_{23}}{4}. \end{aligned} \tag{4.9}$$

Also, this modal equivalent circuit (Fig. 4.2) can be equivalent to a pair of uniform microstrip transmission lines. In [80] have reviewed theories for crosstalk between a pair of uniform microstrip transmission lines and have simplified the theory to easily computed formulas for near-end crosstalk (NEXT) and far-end crosstalk (FEXT). These theories formulas require values for the even- and odd-mode characteristic impedances and the effective dielectric constant for the even- and odd-modes and the isolated strip. It is clear that NEXT greatly depends on the difference between the even- and odd-mode characteristic impedances, and FEXT greatly depends on the difference between the even- and odd-mode effective dielectric constants.

For the two DMs(as long as the weak coupling assumptions are satisfied), the characteristic impedance Z_{d} and propagation constant γ_{d} of a pair of differential transmission lines take the expressions [82]

$$Z_{\mathrm{d}} = \sqrt{\frac{L_{\mathrm{dd11}}}{C_{\mathrm{dd11}}}}, \tag{4.10}$$

$$\gamma_{\mathrm{d}} = j\omega\sqrt{L_{\mathrm{dd11}}C_{\mathrm{dd11}}} = \frac{j\omega\sqrt{\varepsilon_{\mathrm{reffd}}}}{c}, \tag{4.11}$$

and the relative effective dielectric constant $\varepsilon_{\mathrm{reffd}}$ for a pair of differential transmission lines take the expressions

$$\varepsilon_{\mathrm{reffd}} = c^2 L_{\mathrm{dd11}} C_{\mathrm{dd11}}, \tag{4.12}$$

Thus, for discussion DM crosstalk mechanism of the adjacent differential pairs, we proposed the concept of odd- and even-mode in the two DMs in the next section. According to the classical coupled transmission line theory, we can use the approximate solution of [79,80] and equate NEXT and FEXT of DM to the mixed-mode S parameters for extraction parameters of the even- and odd-mode DMs characteristic impedance and effective dielectric constant.

4.3 Proposed Concept of Even- and Odd-Mode Differential Modes

When multi-conductor transmission lines (5-conductor transmission lines) are in close proximity, the electric and magnetic fields will react with each other in specific ways that depend on the signal patterns present on the transmission lines. The importance of this is that these interactions will have to alter as follows:

(A) different phase velocity (relative effective dielectric constant) for odd- and even-mode.

(B) different the effective characteristic impedance for odd- and even-mode.

(C) different conductor losses for odd- and even-mode.

(D) Different dielectric losses for odd- and even-mode.

All of the above will have a negative impact on FEXT and NEXT. For FEXT and NEXT of lossy microstrip transmission lines, (A) and (B) dominating. As long as the simplifying assumptions in weakly coupled and weak imbalance are satisfied, and estimating FEXT and NEXT using lossless assumptions is accurate enough practically. The impact of lossy dielectric material and conductor is almost negligible.

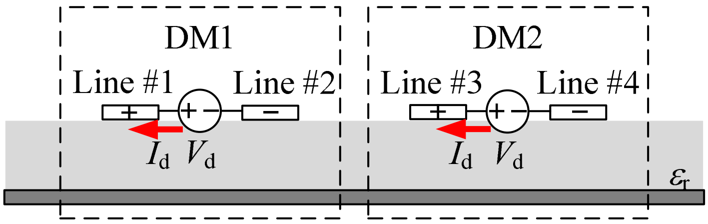

(a) Mode current of same direction

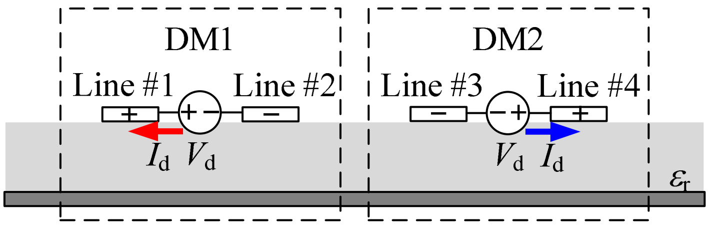

(b) Mode current of opposite direction

Figure 4.5 Two differential-modes excitations for adjacent differential transmission lines.

Now consider two special types of DM excitations for adjacent differential transmission lines, as shown in Fig. 4.5. In Fig. 4.5(a), the mode currents in the DMs are equal in amplitude and in the same direction, and in Fig. 4.5(b), the mode currents in the DMs

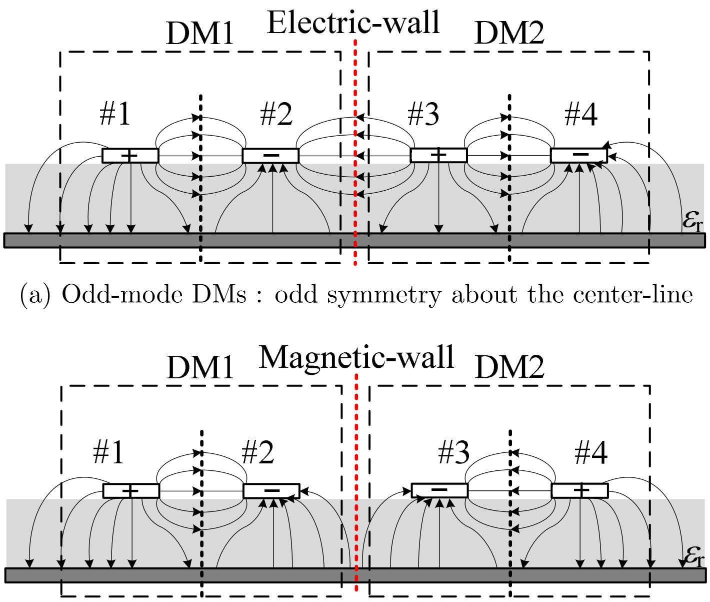

(a) Odd-mode DMs : odd symmetry about the center-line

(b) Even-mode DMs : even symmetry about the center-line

Figure 4.6 Electric field lines of Figs. 4.5(a) and 4.5(b).

are equal in amplitude but in opposite directions. The electric field lines for these two cases are sketched in Fig. 4.6.

As shown in Fig 4.6(a), the electric field lines have odd symmetry about the center-line (red dashed line). Thus, we define it as an odd mode DMs in this thesis. As shown in Fig 4.6(b), the electric field lines have even symmetry about the center-line (red dashed line). Thus, we define it as an even mode DMs in this thesis.

Even- and odd-mode in a pair of coupled transmission lines is deduced in [58]. In this section, for discussion DM crosstalk, we pushed the equivalent inductance and the equivalent capacitance of odd- and even-mode DMs by referring to [58].

4.3.1 Odd-Mode DMs

It is considered to be odd-mode DMs propagation mode in this thesis when two DMs have DM currents with equal magnitude and in the same direction with one another lead to the electric field lines have odd symmetry about the center-line, consider Fig. 4.6(a). Then, to examine the effect that odd-mode DMs propagation on two adjacent differential pairs will have on the characteristic impedance and the relative effective dielectric constant.

In odd-mode DMs propagation, first, let's consider the effect of mutual inductance. Assume that $L_{11} = L_{44}$, $L_{22} = L_{33}$, $L_{12} = L_{34}$, and $L_{13} = L_{24}$. Subsequently, applying

Kirchhoff's voltage law produces

$$V_1 = L_{11}\frac{d}{dt}I_1 + L_{12}\frac{d}{dt}I_2 + L_{13}\frac{d}{dt}I_3 + L_{14}\frac{d}{dt}I_4, \tag{4.13}$$

$$V_2 = L_{12}\frac{d}{dt}I_1 + L_{22}\frac{d}{dt}I_2 + L_{23}\frac{d}{dt}I_3 + L_{13}\frac{d}{dt}I_4, \tag{4.14}$$

$$V_3 = L_{13}\frac{d}{dt}I_1 + L_{23}\frac{d}{dt}I_2 + L_{22}\frac{d}{dt}I_3 + L_{12}\frac{d}{dt}I_4, \tag{4.15}$$

$$V_4 = L_{14}\frac{d}{dt}I_1 + L_{13}\frac{d}{dt}I_2 + L_{12}\frac{d}{dt}I_3 + L_{11}\frac{d}{dt}I_4. \tag{4.16}$$

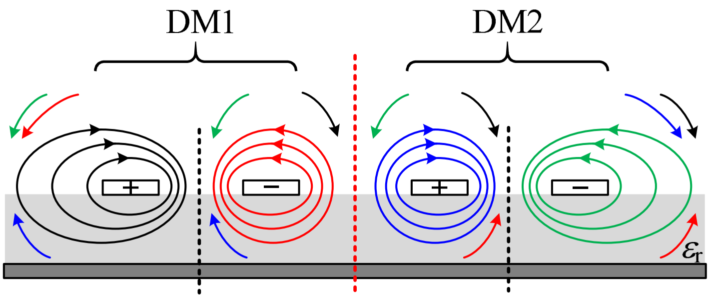

Figure 4.7 Magnetic field : odd-mde DMs.

Since the signals for odd-mode DMs switching are always opposite in adjacent lines, it is necessary to substitute $I_1 = -I_2 = I_3 = -I_4$ and $V_1 = -V_2 = V_3 = -V_4$ into Eqs. (4.13), (4.14), (4.15), and (4.16). And, about the effect of mutual inductance, refer also to Fig. 4.7. This yields

$$V_1 = (L_{11} - L_{12} + L_{13} - L_{14})\frac{d}{dt}I_1, \tag{4.17}$$

$$V_2 = (L_{22} - L_{12} - L_{23} + L_{13})\frac{d}{dt}I_2, \tag{4.18}$$

$$V_3 = (L_{22} + L_{13} - L_{23} - L_{12})\frac{d}{dt}I_3, \tag{4.19}$$

$$V_4 = (L_{11} - L_{14} + L_{13} - L_{12})\frac{d}{dt}I_4. \tag{4.20}$$

According to the relationship between DM voltage (DM current) and actual voltage (actual current) as Eqs. (4.4) and (4.5). This yields

$$V_{d1} = V_1 - V_2 = (L_{11} + L_{22} - 2L_{12} + 2L_{13} - L_{14} - L_{23})\frac{d}{dt}I_{d1}, \tag{4.21}$$

$$V_{d2} = V_3 - V_4 = (L_{11} + L_{22} - 2L_{12} + 2L_{13} - L_{14} - L_{23})\frac{d}{dt}I_{d2}. \tag{4.22}$$

Therefore, the equivalent inductance seen by DM1 in two DMs propagating in odd-mode DMs is

$$L_{\mathrm{d}}^{\mathrm{o}} = L_{11} + L_{22} - 2L_{12} + 2L_{13} - L_{14} - L_{23} = L_{\mathrm{dd11}} + L_{\mathrm{dd12}}. \tag{4.23}$$

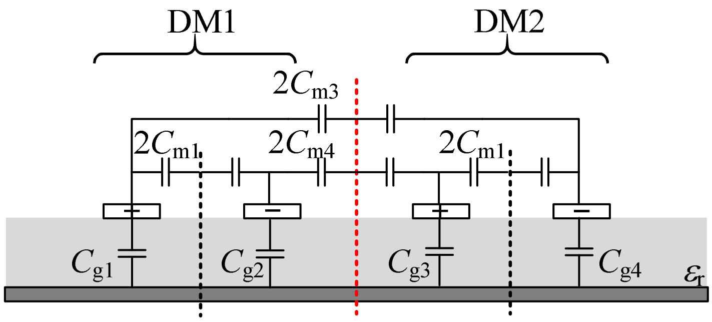

Figure 4.8 Equivalent capacitance for odd mode DMs.

Similarly, the effect of the mutual capacitance can be derived. Refer to Fig. 4.8. Applying Kirchhoff's current law at nodes V_1, V_2, V_3, and V_4 yields (assume that $C_{\mathrm{m1}} =$ -C_{12}, $C_{\mathrm{m2}} =$ -C_{13}, $C_{\mathrm{m3}} =$ -C_{14}, and $C_{\mathrm{m4}} =$ -C_{23})

$$I_1 = C_{\mathrm{g1}}\frac{d}{dt}V_1 + C_{\mathrm{m1}}\frac{d}{dt}(V_1 - V_2) + C_{\mathrm{m2}}\frac{d}{dt}(V_1 - V_3) + C_{\mathrm{m3}}\frac{d}{dt}(V_1 - V_4), \tag{4.24}$$

$$I_2 = C_{\mathrm{g2}}\frac{d}{dt}V_2 + C_{\mathrm{m1}}\frac{d}{dt}(V_2 - V_1) + C_{\mathrm{m4}}\frac{d}{dt}(V_2 - V_3) + C_{\mathrm{m2}}\frac{d}{dt}(V_2 - V_4). \tag{4.25}$$

Because of the symmetry, the equations for I_3 and I_4 are omitted here.

Then, substituting $I_1 = -I_2 = I_3 = -I_4$ and $V_1 = -V_2 = V_3 = -V_4$ for odd-mode DMs propagation, therefore, as following equations yield

$$I_1 = (C_{\mathrm{g1}} + 2C_{\mathrm{m1}} + 2C_{\mathrm{m3}})\frac{d}{dt}V_1, \tag{4.26}$$

$$I_2 = (C_{\mathrm{g2}} + 2C_{\mathrm{m1}} + 2C_{\mathrm{m4}})\frac{d}{dt}V_2. \tag{4.27}$$

According to the relationship between DM voltage (DM current) and actual voltage (actual current). This yields

$$I_{\mathrm{d1}} = \frac{1}{2}(I_1 - I_2) = \frac{1}{4}(C_{11} + C_{22} - 2C_{12} + 2C_{13} - C_{14} - C_{23})\frac{d}{dt}V_{\mathrm{d1}} \tag{4.28}$$

Therefore, the equivalent capacitance seen by DM1 in two DMs propagating in odd-mode DMs is

$$C_{\mathrm{d}}^{\mathrm{o}} = \frac{1}{4}(C_{11} + C_{22} - 2C_{12} + 2C_{13} - C_{14} - C_{23}) = C_{\mathrm{dd11}} + C_{\mathrm{dd12}}. \tag{4.29}$$

Subsequently, the equivalent characteristic impedance and relative effective dielectric constant for two pair of the differential transmission lines propagating in an odd-mode DMs pattern are

$$Z_{\mathrm{d}}^{\mathrm{o}} = \sqrt{\frac{L_{\mathrm{d}}^{\mathrm{o}}}{C_{\mathrm{d}}^{\mathrm{o}}}} = \sqrt{\frac{L_{\mathrm{dd11}} + L_{\mathrm{dd12}}}{C_{\mathrm{dd11}} + C_{\mathrm{dd12}}}}, \tag{4.30}$$

$$\varepsilon_{\mathrm{reffd}}^{\mathrm{o}} = c^2 \left(L_{\mathrm{dd11}} + L_{\mathrm{dd12}}\right)\left(C_{\mathrm{dd11}} + C_{\mathrm{dd12}}\right), \tag{4.31}$$

4.3.2 Even-Mode DMs

Even-mode DMs propagation mode occurs when two DMs are driven with an equal magnitude but in opposite directions with one another lead to the electric field lines have even symmetry about the center-line, consider Fig. 4.6(b). Then, to examine the effect that even-mode DMs propagation on two adjacent differential pairs will have on the characteristic impedance and the relative effective dielectric constant.

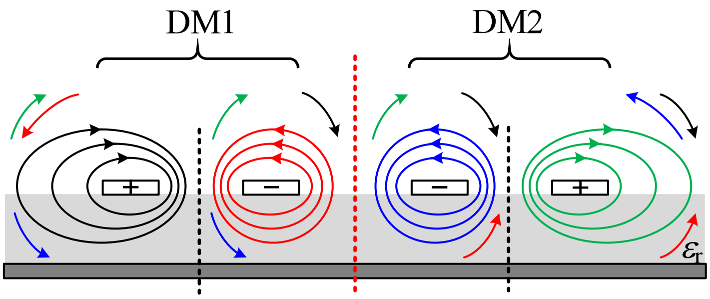

Figure 4.9 Magnetic field : even-mde DMs.

In even-mode DMs propagation, first, let's consider the effect of mutual inductance. Refer to Fig. 4.9. The analysis that was done for even-mode switching can be done to determine the effective even-mode capacitance and inductance. For even-mode DMs, $I_1 = -I_2 = -I_3 = I_4$ and $V_1 = -V_2 = -V_3 = V_4$; therefore, Eqs. 4.13, 4.14, 4.15, and 4.16 yield (Because of the symmetry, only Lines #1 and #2 are discussed here)

$$V_1 = \left(L_{11} - L_{12} - L_{13} + L_{14}\right)\frac{d}{dt}I_1, \tag{4.32}$$

$$V_2 = \left(L_{22} - L_{12} + L_{23} - L_{13}\right)\frac{d}{dt}I_2. \tag{4.33}$$

According to the relationship between DM voltage (DM current) and actual voltage (actual current). This yields

$$V_{\mathrm{d1}} = V_1 - V_2 = \left(L_{11} + L_{22} - 2L_{12} - 2L_{13} + L_{14} + L_{23}\right)\frac{d}{dt}I_{\mathrm{d1}}. \tag{4.34}$$

Therefore, the equivalent inductance seen by DM1 in two DMs propagating in even-mode DMs is

$$L_{\mathrm{d}}^{\mathrm{e}} = L_{11} + L_{22} - 2L_{12} - 2L_{13} + L_{14} + L_{23} = L_{\mathrm{dd11}} - L_{\mathrm{dd12}}. \tag{4.35}$$

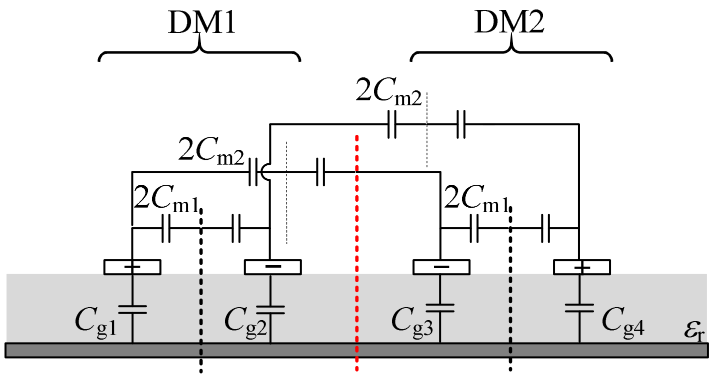

Figure 4.10 Equivalent capacitance for even mode DMs.

Similarly, the effect of the mutual capacitance can be derived. Refer to Fig. 4.10. Substituting $I_1 = -I_2 = -I_3 = I_4$ and $V_1 = -V_2 = -V_3 = V_4$ for even-mode DMs, therefore, Eqs. 4.24 and 4.25 yield

$$I_1 = (C_{\mathrm{g1}} + 2C_{\mathrm{m1}} + 2C_{\mathrm{m2}}) \frac{d}{dt} V_1, \tag{4.36}$$

$$I_2 = (C_{\mathrm{g2}} + 2C_{\mathrm{m1}} + 2C_{\mathrm{m2}}) \frac{d}{dt} V_2. \tag{4.37}$$

According to the relationship between DM voltage (DM current) and actual voltage (actual current). This yields

$$I_{\mathrm{d1}} = \frac{1}{2}(I_1 - I_2) = \frac{1}{4}(C_{11} + C_{22} - 2C_{12} - 2C_{13} + C_{14} + C_{23}) \frac{d}{dt} V_{\mathrm{d1}} \tag{4.38}$$

Therefore, the equivalent capacitance seen by DM1 in two DMs propagating in even-mode DMs is

$$C_{\mathrm{d}}^{\mathrm{e}} = \frac{1}{4}(C_{11} + C_{22} - 2C_{12} - 2C_{13} + C_{14} + C_{23}) = C_{\mathrm{dd11}} - C_{\mathrm{dd12}}. \tag{4.39}$$

Subsequently, the equivalent characteristic impedance and relative effective dielectric constant for two pair of the differential transmission lines propagating in an even-mode DMs pattern are

$$Z_{\mathrm{d}}^{\mathrm{e}} = \sqrt{\frac{L_{\mathrm{d}}^{\mathrm{e}}}{C_{\mathrm{d}}^{\mathrm{e}}}} = \sqrt{\frac{L_{\mathrm{dd11}} - L_{\mathrm{dd12}}}{C_{\mathrm{dd11}} - C_{\mathrm{dd12}}}}, \tag{4.40}$$

$$\varepsilon^{\mathrm{e}}_{\mathrm{reffd}} = c^2 \left(L_{\mathrm{dd11}} - L_{\mathrm{dd12}}\right)\left(C_{\mathrm{dd11}} - C_{\mathrm{dd12}}\right), \tag{4.41}$$

Notice that both Line #1 and Line #2 (Line #3 and Line #4) are always at different potentials, whether odd-mode DMs or even-mode DMs propagation, an effect of the capacitance between the two lines must exist. Line #1 and Line #3 (Line #2 and Line #4) are always at the same potential for odd-mode DMs propagation. Since there is no voltage differential, there can be no effect of capacitance between the lines. Line #1 and Line #3 (Line #2 and Line #4) are always at different potentials in even-mode DMs propagation, an effect of the capacitance between the two lines must exist. They will cause the equivalent characteristic impedance and relative effective dielectric constant characteristics to be slightly different from those analyzed by the 3-conductor transmission lines.

4.4 Differential-Mode Crosstalk Predictions

In this section, we expand the crosstalk theory to computed for DM crosstalk (FEXT and NEXT) between neighboring differential pairs and using the equivalent characteristic impedances ($Z^{\mathrm{o}}_{\mathrm{d}}$ and $Z^{\mathrm{e}}_{\mathrm{d}}$) and relative effective dielectric constants ($\varepsilon^{\mathrm{o}}_{\mathrm{reffd}}$ and $\varepsilon^{\mathrm{e}}_{\mathrm{reffd}}$) of odd- and even-mode DMs to investigate reduction mechanism of DM crosstalk.

4.4.1 Proposed Theoretical Formula

First, in the section uses a modal equivalent circuit created applying the mode-decomposition technique to the telegrapher's equations for analyzing two DMs of a 5-conductor transmission line system, and briefly explain simple expressions for NEXT and FEXT in DMs. Figure 4.11 shows the layout of adjacent differential pairs with line length l. We assume that the four transmission lines have equal width w and thickness t, respectively. The lines are located on a dielectric of thickness h and have a line separation s and adjacent differential pairs distance d. The substrate has a relative permittivity ε_{r}.

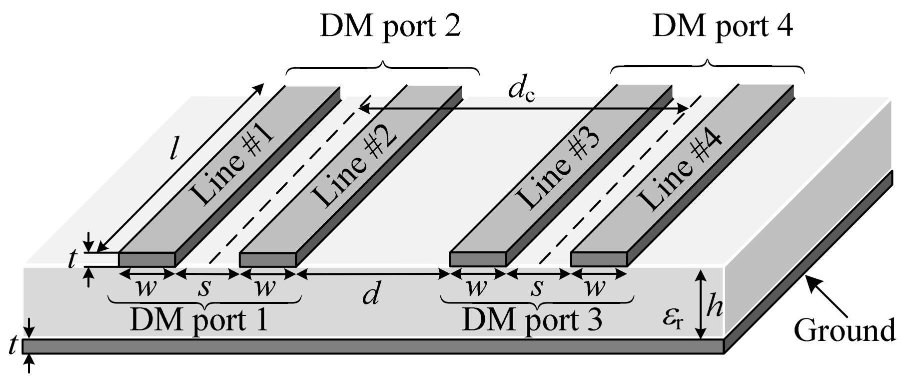

Figure 4.11 Two pairs of differential transmission lines.

To study crosstalk between two DMs, in this case, it is assumed to be 3-conductor transmission lines, as shown in Fig. 4.4. As shown in Fig. 4.12, DM port1 is fed with a differential-mode voltage generator E_d at $x = 0$, and all four ports are terminated with an impedance Z_d. We label the driven and terminated ends of DM ports 1 and 2, and the near and far ends of DM ports 3 and 4.

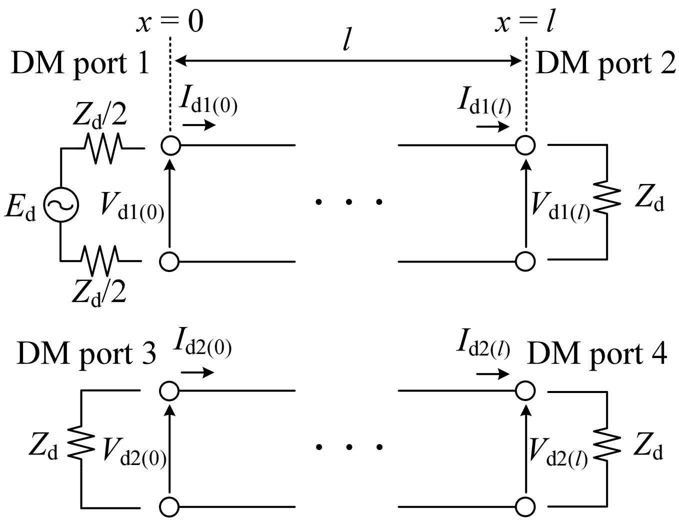

Figure 4.12 Boundary conditions imposed on two DMs.

For DM crosstalk prediction, we assume that the lines are loosely coupled (d is not too small compared to h and s). This because the classic crosstalk predictions formula is derived by solving Telegrapher's equations under the lossless assumptions [79,80]. The stronger coupling between traces makes the influence of lossy conductor and dielectric material will become stronger and affect the prediction results. However, they are often neglected in loosely coupled. According to classical coupled transmission line theory, we can use the approximate solution of [79, 80] and equate NEXT and FEXT of differential mode to the mixed-mode S parameters as follows:

$$S_{\mathrm{dd31}} = \frac{V_{\mathrm{d2}}(0)}{V_{\mathrm{d1}}(0)} \tag{4.42}$$

$$S_{\mathrm{dd41}} = \frac{V_{\mathrm{d2}}(l)}{V_{\mathrm{d1}}(0)} \tag{4.43}$$

NEXT (S_{dd31}) and FEXT (S_{dd41}) in the differential mode are written as

$$S_{\mathrm{dd31}} = \frac{\Delta Z}{2Z_\mathrm{d}} \left\{ 1 - e^{-2\gamma_\mathrm{d} l}[\cos(2\Delta K l) + \frac{\Delta Z}{Z_\mathrm{d}} \sin(2\Delta K l)] \right\} \tag{4.44}$$

$$S_{\mathrm{dd41}} = -je^{-\gamma_\mathrm{d} l} \sin(2\Delta K l) \approx -j\Delta K l. \tag{4.45}$$

where

$$\Delta Z = \left| \frac{Z_{\mathrm{d}}^{\mathrm{e}} - Z_{\mathrm{d}}^{\mathrm{o}}}{2} \right| \approx \left| \frac{j\omega}{2\gamma_{\mathrm{d}}} \left(L_{\mathrm{dd12}} - C_{\mathrm{dd12}} Z_{\mathrm{d}}^{2} \right) \right| \tag{4.46}$$

and

$$\Delta K = \left| \frac{\omega \left(\sqrt{\varepsilon_{\mathrm{reffd}}^{\mathrm{e}}} - \sqrt{\varepsilon_{\mathrm{reffd}}^{\mathrm{o}}} \right)}{2c} \right| \approx \left| \frac{\omega \left(L_{\mathrm{dd12}} + C_{\mathrm{dd12}} Z_{\mathrm{d}}^{2} \right)}{2Z_{\mathrm{d}}} \right|. \tag{4.47}$$

where c is the velocity of light in free space. Moreover, notice that the investigations performed in this thesis are based on all ports that are well-matched.

According to Eqs. (4.44), (4.45), (4.46), and (4.47) for NEXT (S_{dd31}) and FEXT (S_{dd41}), it is found that NEXT greatly depends on the difference ΔZ between the even- and odd-mode characteristic impedances in DMs, and FEXT greatly depends on the difference ΔK between the even- and odd-mode relative effective dielectric constants in DMs. According to Eqs. (4.46) and (4.47), it is found that the values of ΔZ and ΔK depend on L_{dd12} and C_{dd12}. Because the relationship between L_{dd12} and C_{dd12} is always positive and negative. Therefore, L_{dd12} and C_{dd12} have an additive relationship in Eq. (4.46), while the subtractive relationship between L_{dd12} and C_{dd12} in Eq. (4.47). FEXT can be minimized when L_{dd12} and C_{dd12} are both 0 or $|L_{\mathrm{dd12}}|$ and $|C_{\mathrm{dd12}}Z_{\mathrm{d}}^{2}|$ are equal, while NEXT must be L_{dd12} and C_{dd12} are both 0.

4.4.2 Validation of Proposed Theoretical Formula

In this section, we will discuss the effect of d_{c} (distance between the center lines of the adjacent differential pairs) changes on generated FEXT and NEXT between adjacent differential pairs. And, the generation mechanism of NEXT and FEXT in DM is discussed using Eqs. (4.44) and (4.45). Figure 4.13 shows the layout of adjacent conventional differential pairs. The cross-sectional view shown in Fig. 4.13(b). The structural and electrical characteristics parameters used in Section 4.5 are summarized in Table 4.1. The height of the dielectric h is 200 μm, dielectric constant of the glass epoxy ε_{r} is 4.4, the trace thickness t is 35 μm. The differential-mode characteristic impedance Z_{d} of an isolated differential pair was set to 100 Ω (line width $w = 0.21$, line separation $s = 0.15$) by using 2D Extractor based on the cross-sectional structure shown in Fig. 4.13(b).

Table 4.1 Structural and electrical parameters in this chapter.

Item	Value	Unit
ε_{r}	4.4	-
h	200	μm
t	35	μm
Z_{d}	100	Ω

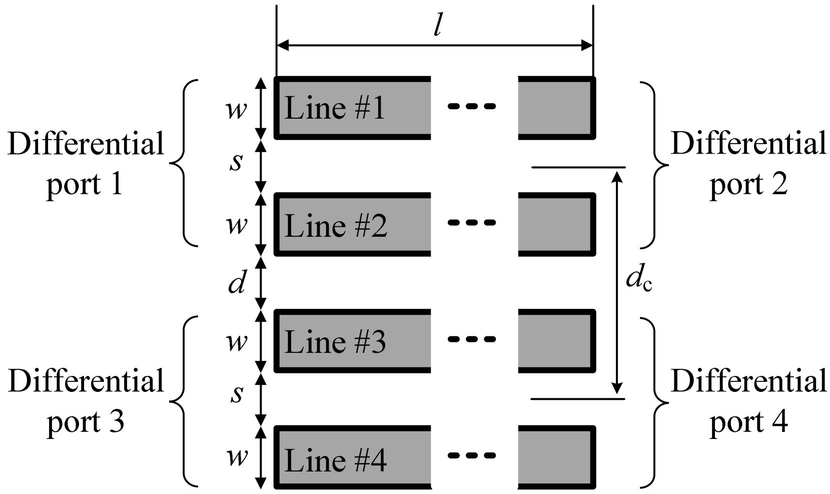

(a) Top view of conventional differential pairs

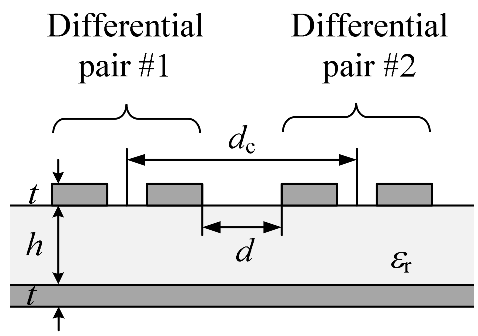

(b) Cross-sectional view

Figure 4.13 Physical structures of adjacent differential pairs.

Then, the load impedance of all DM ports should well-matched the differential-mode characteristic impedance of each differential pair is adjacent differential pairs. And, we don't want the modal coupling (C_{dd12} and L_{dd12}) between the two DMs to change Z_{d} and $\varepsilon_{\mathrm{reffd}}$, which lead to the deterioration of differential-mode transmission characteristics. For large the adjacent differential pairs distance d, the modal coupling L_{dd12} and C_{dd12} between the DMs become small. In this case, the differential-mode characteristic impedance Z_{d} and relative effective dielectric constant $\varepsilon_{\mathrm{reffd}}$ of each differential pair approach that of an isolated differential pair. Thus, first, the change in Z_{d} and $\varepsilon_{\mathrm{reffd}}$ as a function of adjacent differential pairs distance d are calculated, as shown in Figs. 4.14(a) and 4.14(b). According to the change in Z_{d} and $\varepsilon_{\mathrm{reffd}}$, a weakly coupling k

$$k = \frac{Z_{\mathrm{d}}^{\mathrm{e}} - Z_{\mathrm{d}}^{\mathrm{o}}}{Z_{\mathrm{d}}^{\mathrm{e}} + Z_{\mathrm{d}}^{\mathrm{o}}} \tag{4.48}$$

is determined, as shown in Fig. 4.14(c).

Figures 4.14(a) and 4.14(b) show the change in Z_{d} and $\varepsilon_{\mathrm{reffd}}$. The differential-mode characteristic impedance Z_{d} and the relative effective dielectric constant $\varepsilon_{\mathrm{reffd}}$ of an isolated differential pair, as shown in green lines. The black lines indicate Z_{d} and $\varepsilon_{\mathrm{reffd}}$ of

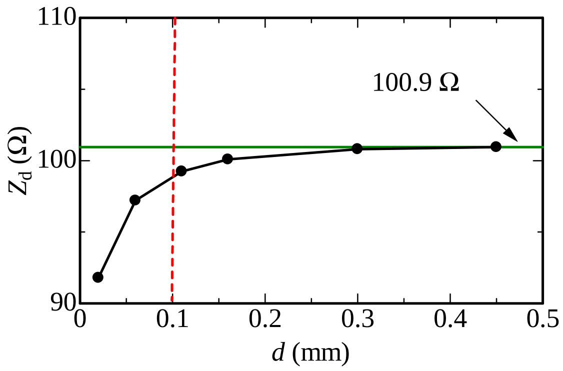

(a) Change in differential-mode characteristic impedance Z_d

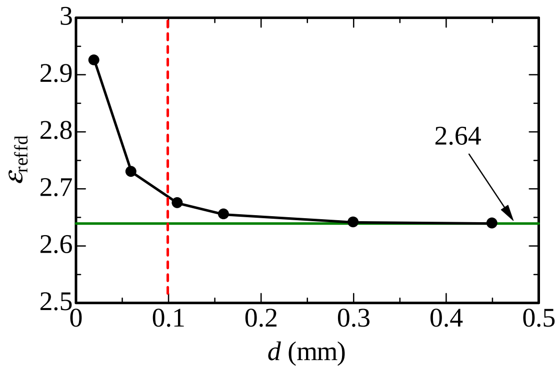

(b) Change in relative effective dielectric constant $\varepsilon_{\mathrm{reffd}}$

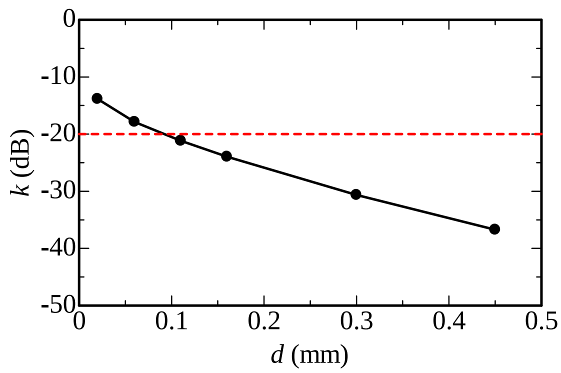

(c) Coupling k

Figure 4.14 Change in Z_d, $\varepsilon_{\mathrm{reffd}}$, and k as a function of adjacent differential pairs distance d.

Table 4.2 Conventional structural parameters.

Item	Value	Unit
w	0.21	mm
s	0.15	mm
l	50	mm
d	0.16 / 0.3 / 0.45	mm
d_c	0.73 / 0.87 / 1.02	mm

each differential pair change with d. As a result, it is found that the modal coupling between the two DMs leads to a drastic change in the differential-mode characteristic impedance Z_d and the relative effective dielectric constant $\varepsilon_{\mathrm{reffd}}$ of each differential pair when adjacent differential pairs distance d below 0.1 mm. Thus, the adjacent differential pairs distance d used in this thesis will be higher than 0.1 mm. Figures 4.14(c) shows the transmission characteristics of each differential pair will not have much impact when the coupling k below -20 dB.

Three types of conventional differential pairs with $l = 50$ mm are used for evaluation by full-wave simulation (commercial simulator, ANSYS HFSS), and their structural parameters are summarized in Table 4.2. Generally speaking, the distance between adjacent differential pairs d is set to about three times the value of line separation s to suppress crosstalk. Therefore, the line width w and line separation s of conventional differential pairs were fixed, and d_c was set to 0.73 ($d \simeq 1s = 0.16$ mm), 0.87 ($d = 2s = 0.3$ mm), and 1.02 mm ($d = 3s = 0.45$ mm), respectively, to evaluate the DM crosstalk mechanism. And, the inductance and capacitance matrices of these three types of conventional differential pairs are extracted by 2D Extractor for analyzing the different relative effective dielectric constant and effective characteristic impedance for odd- and even-mode of two adjacent differential pairs by Eqs. (4.44) and (4.45).

FEXT in DMs

First, the FEXT in DMs was evaluated using these three types of structures, as shown in Table 4.2. According to Eq. (4.45), FEXT greatly depends on ΔK, which is the difference between $\varepsilon^{\mathrm{e}}_{\mathrm{reffd}}$ and $\varepsilon^{\mathrm{o}}_{\mathrm{reffd}}$.

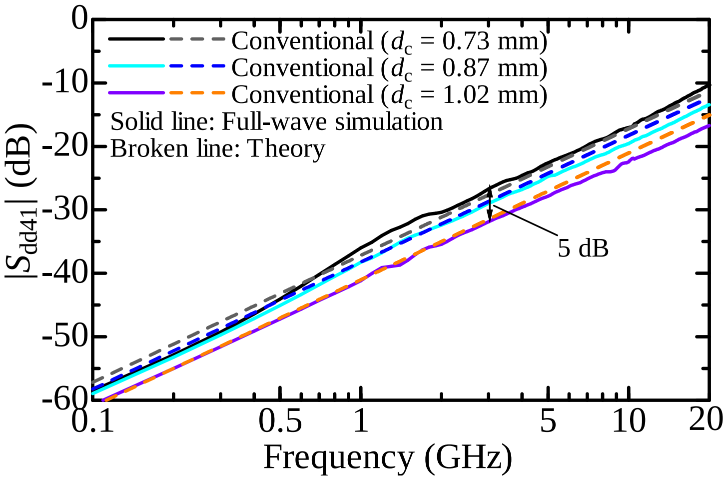

Figure 4.15 Comparison of FEXT characteristics between full-wave simulation and analytical result.

Figure 4.15 shows FEXT($|S_{\mathrm{dd41}}|$) and the solid lines denote the full-wave simulation at frequencies ranging from 0.1 to 20 GHz. On the other hand, the broken lines are obtained from Eq. (4.45). And it is clear that the results obtained from Eq. (4.45) are almost in agreement with full-wave simulation. This means that the parameter extraction is valid. Therefore, we were able to explain the FEXT reduction mechanism by focusing on $\varepsilon^{\mathrm{e}}_{\mathrm{reffd}}$, $\varepsilon^{\mathrm{o}}_{\mathrm{reffd}}$, L_{dd12}, and C_{dd12}.

Figure 4.16 shows the $\varepsilon^{\mathrm{e}}_{\mathrm{reffd}}$ and $\varepsilon^{\mathrm{o}}_{\mathrm{reffd}}$ as a function of distance between the center lines of the adjacent differential pairs, d_c. It shows that even if d_c increases, the difference

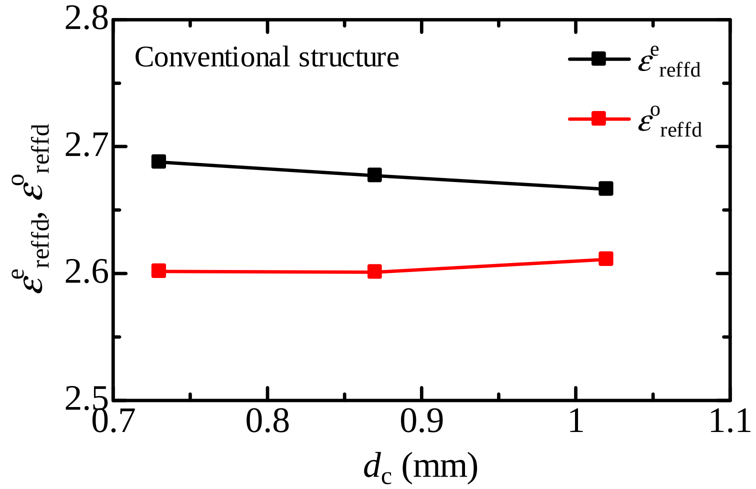

Figure 4.16 $\varepsilon^{e}_{\mathrm{reffd}}$ and $\varepsilon^{o}_{\mathrm{reffd}}$ as a function of distance d_{c} between the center lines of the adjacent differential pairs.

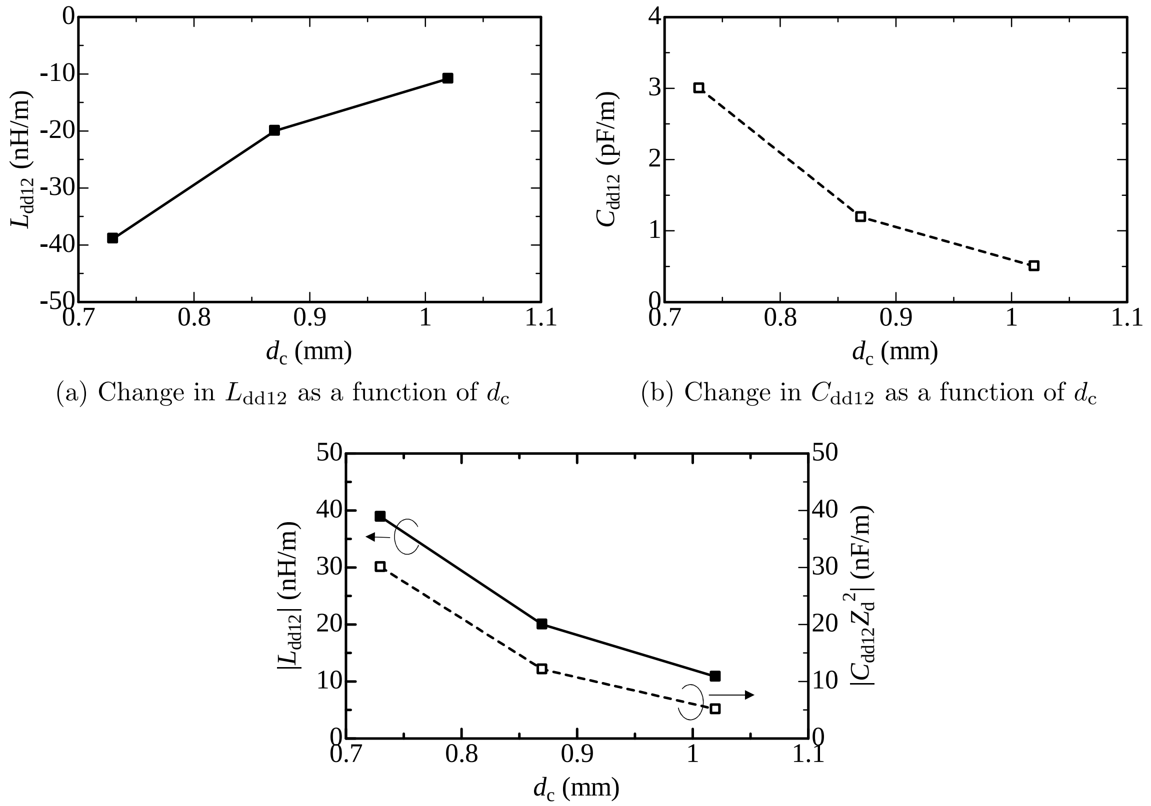

(a) Change in L_{dd12} as a function of d_{c}

(b) Change in C_{dd12} as a function of d_{c}

(c) Difference between $|L_{\mathrm{dd12}}|$ and $|C_{\mathrm{dd12}}Z_{\mathrm{d}}^2|$

Figure 4.17 Crosstalk modal coupling L_{dd12} and C_{dd12} between the DMs.

between $\varepsilon^{e}_{\mathrm{reffd}}$ and $\varepsilon^{o}_{\mathrm{reffd}}$ does not change significantly. This is because the decrease of FEXT is not entirely dependent on the increase of distance d_{c} between the center lines of the adjacent differential pairs but also on the difference between $|L_{\mathrm{dd12}}|$ and $|C_{\mathrm{dd12}}Z_{\mathrm{d}}^2|$. Refer to Eq. 4.47. Next, Figs. 4.17(a) and (b) show the crosstalk modal coupling L_{dd12} and C_{dd12} between the CMs and explained the relationship between L_{dd12} and C_{dd12} is always positive and negative. Although the crosstalk modal coupling L_{dd12} and C_{dd12} tend to zero with the increase of d_{c}, the difference between $|L_{\mathrm{dd12}}|$ and $|C_{\mathrm{dd12}}Z_{\mathrm{d}}^2|$ does not change much, as shown in Fig. 4.17(c).

From the above, with adjacent conventional differential pairs, SI is affected by DM crosstalk unless the distance d between adjacent differential pairs is sufficient. In particular, the suppression of FEXT requires a larger d_{c}. This is because, even if the distance between adjacent differential pairs d increases three times the value of line separation s, the amount of suppression is only 5 dB, as shown in Fig. 4.15. Therefore, it is difficult to apply next-generation high-density wiring for the high-speed signal transmission system.

NEXT in DM

Then, the NEXT in DMs was evaluated using these three types of structures, as shown in Table 4.2. According to Eq. (4.44), NEXT greatly depends on ΔZ, which is the difference between $Z_{\mathrm{d}}^{\mathrm{e}}$ and $Z_{\mathrm{d}}^{\mathrm{o}}$. With the increase of d_{c}, L_{dd12} and C_{dd12} will decrease, as shown in Figs. 4.17(a) and (b). Therefore, the difference between $Z_{\mathrm{d}}^{\mathrm{e}}$ and $Z_{\mathrm{d}}^{\mathrm{o}}$ decreases with it. This is because the NEXT in DMs only dependent on $(|L_{\mathrm{dd12}}| + |C_{\mathrm{dd12}}Z_{\mathrm{d}}^2|)$. Refer to Eq. 4.46.

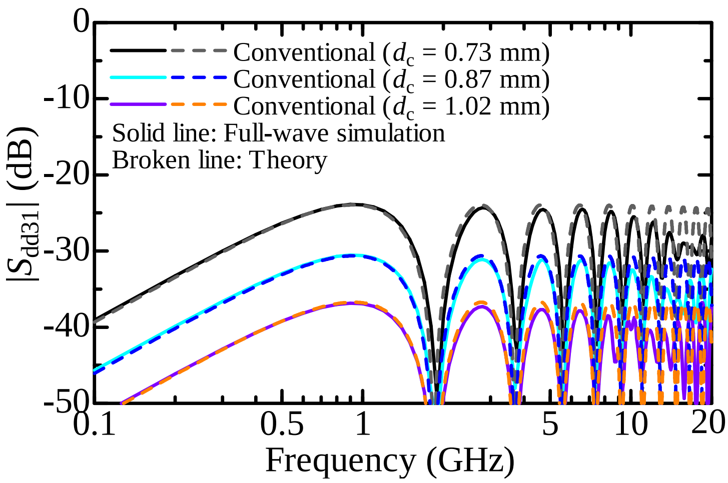

Figure 4.18 Comparison of NEXT characteristics between full-wave simulation and analytical result.

Figure 4.18 shows NEXT($|S_{\mathrm{dd31}}|$) and the solid lines denote the full-wave simulation at frequencies ranging from 0.1 to 20 GHz. On the other hand, the broken lines are obtained from Eq. (4.44). And it is clear that the results obtained from the theoretical formula of this research are almost in agreement with full-wave simulation. This means that the

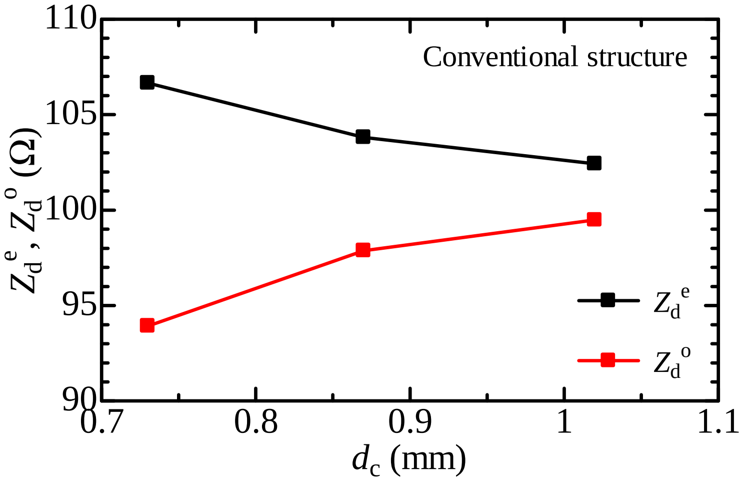

Figure 4.19 Z_d^e and Z_d^o as a function of d_c.

parameter extraction is valid.

Figure 4.19 shows the Z_d^e and Z_d^o as a function of distance between the center lines of the adjacent differential pairs, d_c. With the increase of d_c, the difference between Z_d^e and Z_d^o decreases. This is because the sum of $|L_{dd12}|$ and $|C_{dd12}Z_d^2|$ decreases with an increase of d_c, as shown in Figs. 4.17(a) and (b). From the above, to suppress NEXT, we need to reduce modal coupling L_{dd12} and C_{dd12} as much as possible.

4.5 Reduction Mechanism of DM Crosstalk Due to Periodic Structure

In this section, first, we investigated the transmission characteristics of the differential pair when introducing the periodic structure as Fig. 4.20. The requirements for the

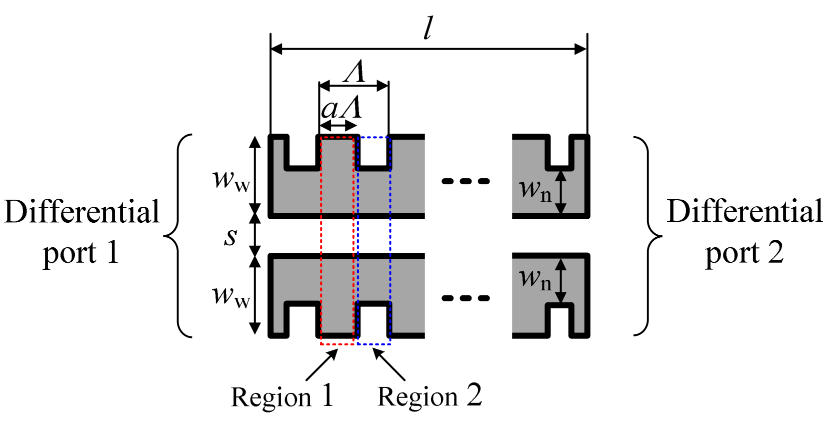

Figure 4.20 One differential pair with periodic structure.

periodic structure investigations were as follows:

(1) effective differential-mode characteristic impedance,

(2) effective relative permittivity,

(3) upper limit frequency.

Finally, the focus of this thesis is only on the odd- and even-mode in DMs and using the theoretical formula of crosstalk to investigate the reduction mechanism of DM crosstalk between adjacent differential pairs with the periodic structure.

4.5.1 Propagation Characteristics of Periodic Structure

Figure 4.20 shows the periodic structure differential pair treated in this thesis. The structural parameters of differential pairs with the periodic structure are as follows: the wide part of line width w_w, the narrow part of line width w_n, the lattice length Λ, the occupation ratio a.

Effective Differential-Mode Characteristic Impedance and Effective Relative Permittivity

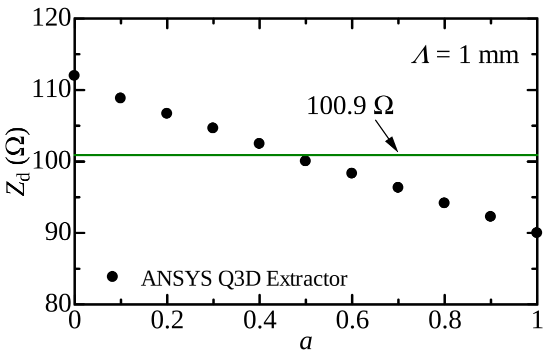

(a) Effective differential-mode characteristic impedance

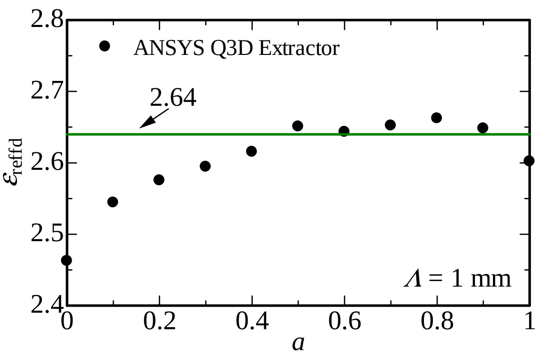

(b) Relative effective dielectric constant

Figure 4.21 Relationship between transmission characteristics of the differential pair with periodic structure and occupation ratio a.

The geometries of the periodic structure differential pair in this section are illustrated in Fig. 4.20. The height of the dielectric h is 200 μm, dielectric constant of the glass epoxy ε_r is 4.4, the trace thickness t is 35 μm shown in Table 4.1. The unit cell of the periodic structure has consisted of two regions (Regions 1 and 2). In this thesis, electromagnetic field simulation by ANSYS Q3D Extractor was performed to extract inductance and capacitance matrices for the differential pair shown in Fig. 4.20 with l = 10 mm. Then, using the Eqs. (4.10) and (4.12), the effective characteristic impedance and the effective relative permittivity can be calculated. And, Region 1 of length $a\Lambda$ and line width $w_{\mathrm{w}} =$ 0.24 mm ($Z_{\mathrm{d}} = 90\ \Omega$, $\varepsilon^{\mathrm{d}}_{\mathrm{reff}} = 2.6$) and Region 2 of length $(1 - a)\Lambda$ and width $w_{\mathrm{n}} = 0.13$ mm ($Z_{\mathrm{d}} = 112\ \Omega$, $\varepsilon^{\mathrm{d}}_{\mathrm{reff}} = 2.46$).

Figure 4.21(a) shows the relationship between occupation ratio a and the effective differential-mode characteristic impedance Z_{d} when the period length $\Lambda = 1.0$ mm. The differential-mode characteristic impedance Z_{d} of an isolated conventional differential pair in Table 4.2, as shown in green lines. As a result, the effective differential-mode characteristic impedance Z_{d} of differential pair with periodic structure approach that of an isolated conventional differential pair when the occupation ratio $a = 0.5$. Also, Fig. 4.21(b) shows the relationship between occupation ratio a and the relative effective dielectric constant $\varepsilon_{\mathrm{reffd}}$ when the period length $\Lambda = 1.0$ mm. The relative effective dielectric constant $\varepsilon_{\mathrm{reffd}}$ of an isolated conventional differential pair, as shown in green lines. As a result, the relative effective dielectric constant $\varepsilon_{\mathrm{reffd}}$ of differential pair with periodic structure approach that of an isolated conventional differential pair when the occupation ratio $a = 0.5$.

Upper Limit Frequency

When the structure changes periodically, multiple reflections occur, and there are frequencies where signals cannot be transmitted. This lowest frequency is considered to be the upper limit frequency of the periodic structure differential line in this thesis.

In this thesis, the lattice length Λ is set to 1.0 mm, assuming high-frequency transmission. To clarify the upper limit frequency of this lattice length in consideration of calculation cost and accuracy, the approximate upper limit frequency for $\Lambda = 1.0$ mm was estimated from the upper limit frequency obtained from the reflection characteristics of $\Lambda = 10$ mm with the lattice length multiplied by 10.

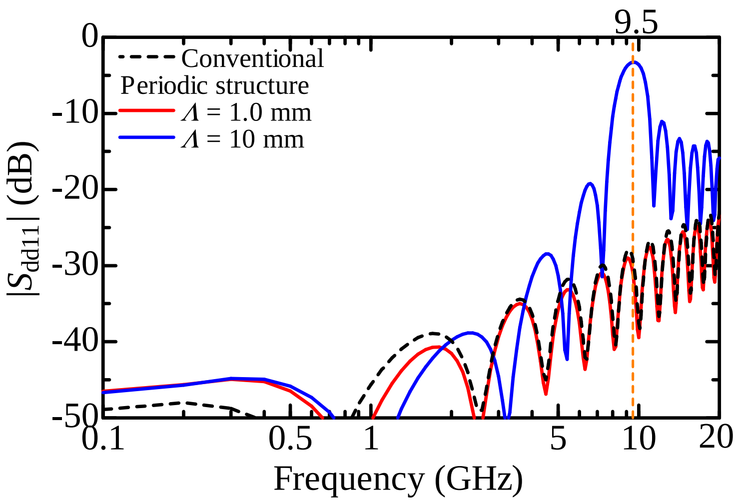

Figure 4.22 Differential-mode reflection coefficient.

Figure 4.22 [78] shows the calculation results using 3D electromagnetic simulation

(ANSYS HFSS). The solid red line indicates the lattice length $\Lambda = 1.0$ mm. On the other hand, the solid blue line shows the result for the lattice length $\Lambda = 10$ mm. At this time, the upper limit frequency of the line is near 9.5 GHz from the differential-mode reflection coefficient S_{dd11} in Fig. 4.22. From this, it is considered that the upper limit frequency is 95 GHz for the lattice length $\Lambda = 1.0$ mm used in this thesis.

First, confirm the upper limit frequency by a simple calculation. If multiple reflections occur in the period of the structure, signal transmission becomes impossible, so the transmission limit is considered when the period length Λ is half the wavelength of the signal. From this, the upper limit frequency f_{c} can be represented by period length Λ [78], as follows

$$f_{\mathrm{c}} = \frac{c}{2\sqrt{\varepsilon_{\mathrm{reffd}}}\Lambda}, \tag{4.49}$$

where c is the velocity of light in free space. In this structure, the upper limit frequency can be estimated to be $f_{\mathrm{c}} = 92.1$ GHz when the period length $\Lambda = 1.0$ mm because of $\varepsilon_{\mathrm{reffd}} = 2.65$. This is in good agreement with the above 95 GHz.

Transmission Characteristics

Here, the differential-mode reflection and transmission characteristics of one pair of differential lines with the periodic structure are compared with those of the conventional differential lines with the dimensions shown in Table 4.2.

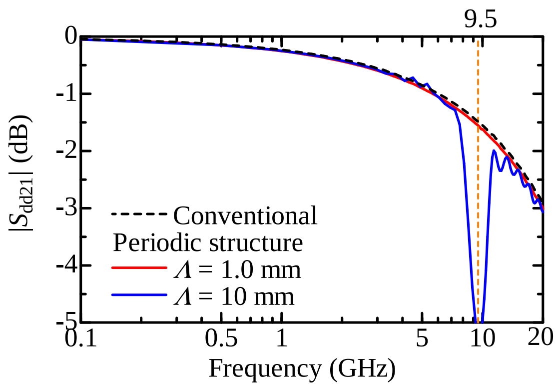

(a) Differential-mode transmission coefficient

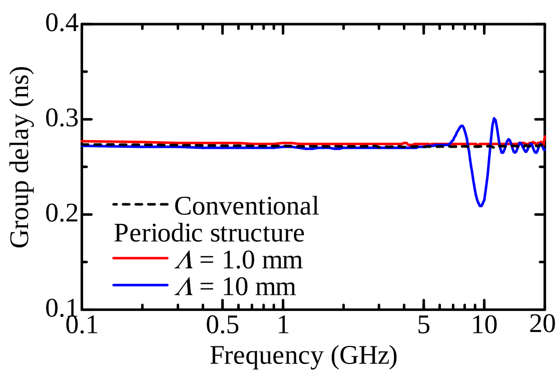

(b) Group delay

Figure 4.23 Characteristics of one pair of differential pair.

Fig. 4.22 shows the broken line denotes the conventional differential lines. From Fig. 4.22, when $\Lambda = 1.0$ mm, the reflection characteristics are almost agree with that of the conventional differential pair. From Fig. 4.23(a) [78], when $\Lambda = 1.0$ mm, the transmission characteristics almost agree with that of the conventional differential pair. From this, it can be seen that if the reflection can be suppressed even when the periodic structure is introduced, the same transmission characteristics as the conventional differential pair can be obtained. Figure 4.23(b) [78] shows the group delay. From these results, it is clear that the transmission characteristics of a periodic differential line with a group delay time T_g of $\Lambda = 1.0$ mm are almost the same as those of the conventional differential pair below 20 GHz. Thus, it is considered that the output waveform of the periodic structure line has almost no distortion, and the signal can be transmitted.

4.5.2 Evaluation of Crosstalk in Adjacent Differential Pairs with Periodic Structure

In the previous section, we evaluated one pair of differential transmission lines with the periodic structure and confirmed that they were effective as lines. In this section, we evaluate the crosstalk when two pairs of periodic structure differential pairs are arranged adjacent to each other, as shown in Fig. 4.24.

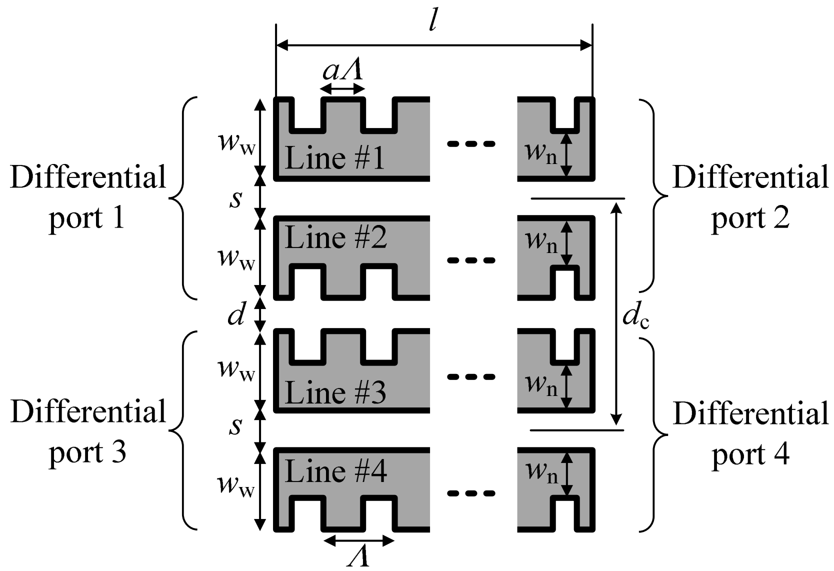

Figure 4.24 Top view of differential pairs with periodic structure.

Table 4.3 Periodic structural model parameters.

Item	Value	Unit
w_w	0.24	mm
w_n	0.13	mm
s	0.12	mm
Λ	1	mm
a	0.5	mm
l	50	mm
d	0.13	mm
d_c	0.73	mm

The parameters of the conventional differential pair used in Table 4.2 were used, and the distance d_c between adjacent lines was 0.73 mm. The distance d_c from the center of the differential line to the center of the adjacent differential pairs was set to be equal at 0.73 mm so that the conventional differential line and the periodic structure line had the same wiring density. The structural parameters of the periodic structure lines are summarized in Table 4.3.

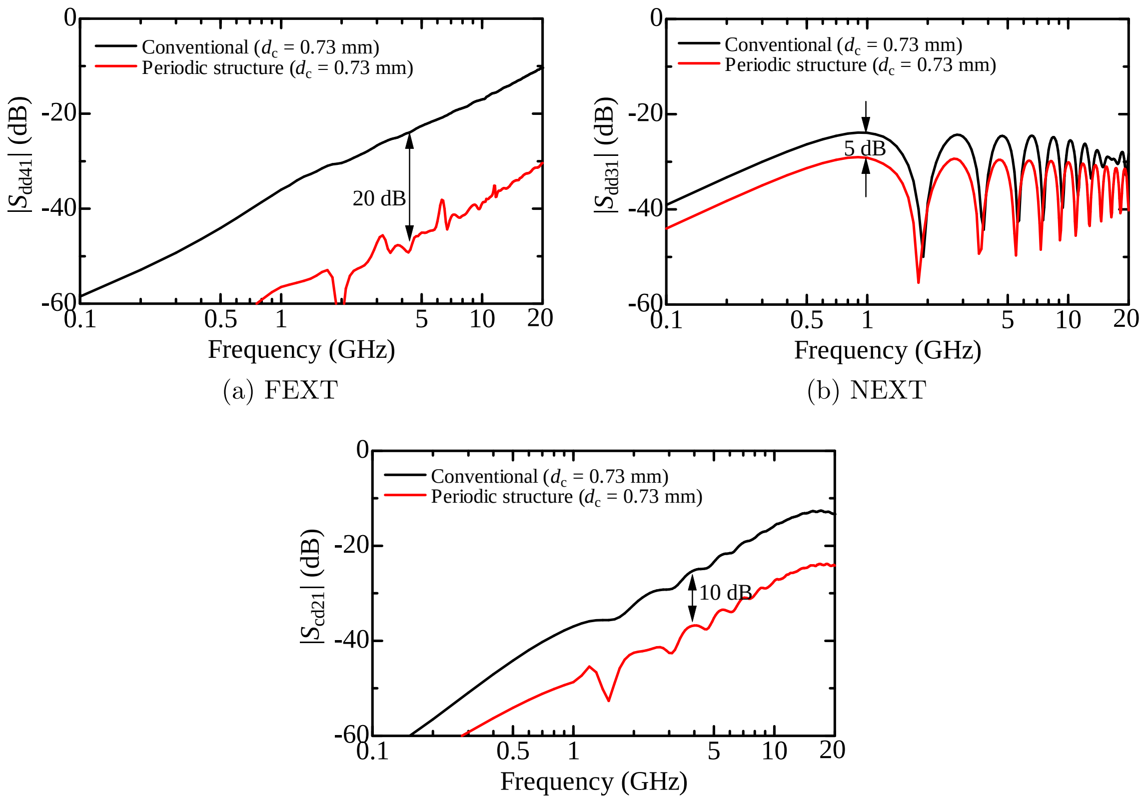

(a) FEXT

(b) NEXT

(c) Differential-to-common mode conversion

Figure 4.25 Propagation characteristics of differential pairs.

Figure 4.25 shows the propagation characteristics for two pairs of differential transmission lines. In Fig. 4.25(a), the FEXT ($|S_{dd41}|$) of the proposed periodic differential pairs was reduced by 20 dB or more compared to the conventional ones, and about 5 dB NEXT suppression, as shown in Fig. 4.25(b). In the next section, Eqs. (4.44) and (4.45) are used to investigate the DM crosstalk-reduction mechanism of the proposed periodic structure.

The amount of the differential-to-common mode conversion ($|S_{cd21}|$) in Fig. 4.25(c) is also suppressed by introducing the periodic structure. This is because the periodic structure weakened the coupling with the adjacent differential pairs compared to the conventional transmission lines. Therefore, it is considered that degradation of signal quality was prevented by suppressing differential-to-common mode conversion in this way.

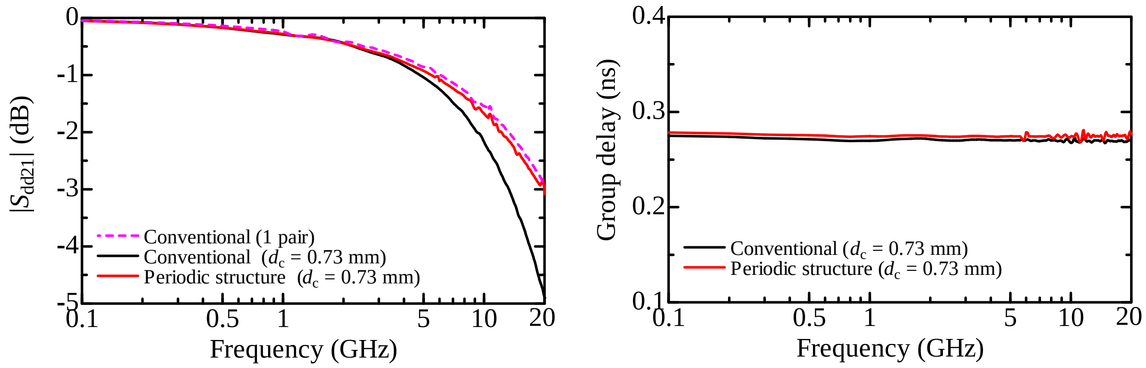

(a) Differential-mode transmission coefficient (b) Group delay

Figure 4.26 Transmission characteristics of differential pairs.

Next, Fig. 4.26 shows the transmission characteristics for two pairs of differential transmission lines. From the transmission characteristics shown in Fig.Fig. 4.26(a), it can be seen that the periodic structure line is better than the conventional differential pairs due to the suppression of crosstalk and the reduction of the mode conversion amount. Also, the transmission characteristics when the periodic structure is introduced are improved to the same level as a pair of conventional differential pair (pink dashed line) without crosstalk. Therefore, in high-density mounting, introducing a periodic structure is more effective from the viewpoint of maintaining SI. Furthermore, for the group delay shown in Fig. 4.26(b), the delay time of the periodic structure line is also constant, and it can be seen that the transmission characteristics are almost the same as those of the conventional differential pairs below 20 GHz. From this, it is considered that there is almost no distortion even if the periodic structure line is arranged adjacently, and the signal can be transmitted.

4.5.3 Fabrication of Proposed Periodic Structure and Evaluation by Measurement

In this section, the conventional structure and the periodic structure (d_c = 0.73 mm) from the previous discussion were fabricated, and the NEXT and FEXT in DMs were evaluated through measurement.

To obtain mixed-mode S parameters, an 4-port measurement was carried out using a VNA (KEYSIGHT E5071C) and a pair of 200-μm-pitched GSGSG microprobes (Cascade Microtech ACP-40-D-GSGSG). The measured data were plotted below 20 GHz due to the measurement limit of the vector network analyzer.

The set up of single-ended 4-port VNA measurement NEXT is shown in Fig. 4.27(a). During the 4-port VNA measurement, four ports on the left side of the adjacent differential pairs are connected to 4-port VNA respectively, and the four remaining ports were terminated with a chip resistance of 50 Ω.

The set up of single-ended 4-port VNA measurement FEXT is shown in Fig. 4.27(b). In adjacent differential pairs, two ports on the left side of the first differential pair and two ports on the right side of another differential pair are connected to 4-port VNA, respectively, and the four remaining ports were terminated with a chip resistance of 50 Ω.

In adjacent differential pairs, 2 ports on the left of the first pair of the differential transmission lines and 2 ports on the right of the other pair of the differential transmission lines are connected to 4-port VNA respectively, and the 4 remaining ports were terminated with a chip resistance of 50 Ω.

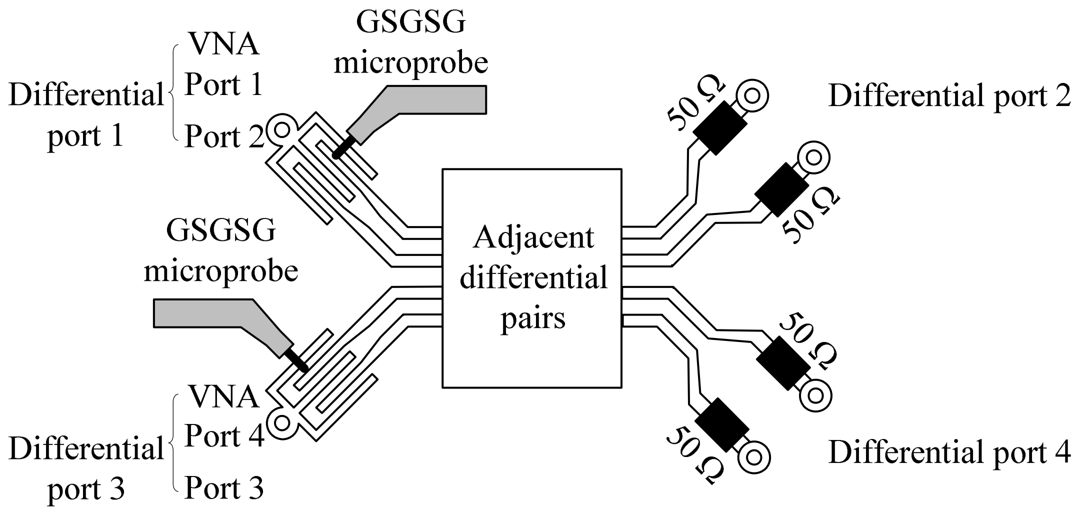

(a) NEXT measurement system

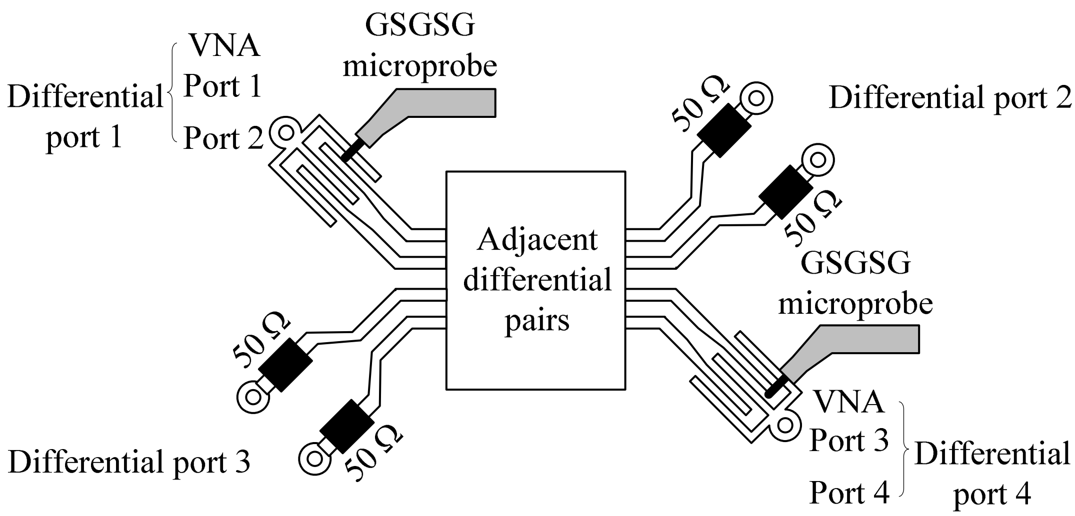

(b) FEXT measurement system

Figure 4.27 NEXT and FEXT measurement system.

These 4-port measurement results can be used to form standard 4-port S parameters. Standard S parameters will be converted into mixed-mode S parameters. According to Fig. 4.27(a), and using the algebraic form of $|S_{\mathrm{dd21}}|$ from the standard 4-port S parameters, the NEXT ($|S_{\mathrm{dd31}}|$) equation can be written as

$$S_{\mathrm{dd31}} = \frac{1}{2}(S_{31} - S_{32} - S_{41} + S_{42}), \tag{4.50}$$

and, in the same way, according to Fig. 4.27(b), the FEXT ($|S_{\mathrm{dd41}}|$) equation can be written as

$$S_{\mathrm{dd41}} = \frac{1}{2}(S_{31} - S_{32} - S_{41} + S_{42}). \tag{4.51}$$

Finally, Fig. 4.28 shows the NEXT and FEXT in DMs as a function of frequency concerning the conventional differential pairs and the proposed periodic structure which suppressed DM crosstalk most. It is observed from Fig. 4.28 as follow: First, at lower fre-

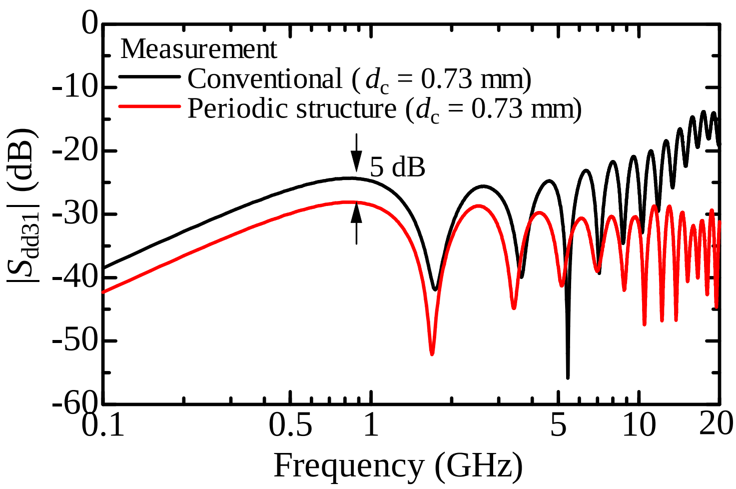

(a) NEXT in DMs

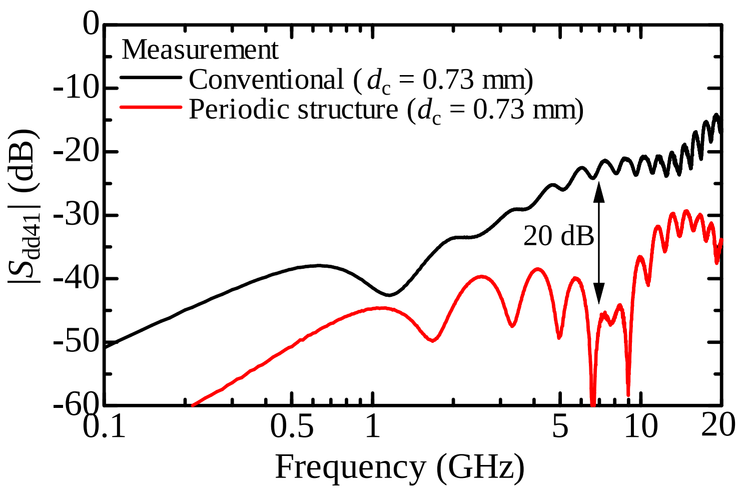

(b) FEXT IN DMs

Figure 4.28 Crosstalk characteristics obtained by measurement.

quencies results, the NEXT in DM of the proposed periodic structure was decreased by approximately 5 dB compared to the conventional differential pairs, as shown in Fig. 4.28(a).

Then, due to introducing the periodic structure, there is about 20 dB FEXT suppression at frequencies ranging from 5 to 10 GHz, as shown in Fig. 4.28(b). It was confirmed by actual measurement that crosstalk can be suppressed by introducing the periodic structure into the differential pairs.

4.5.4 Mechanism of Crosstalk between Adjacent Differential Pairs with Periodic Structure

The proposed periodic structure with $l = 50$ mm is used for evaluation by full-wave simulation (commercial simulator, ANSYS HFSS), and their structural parameters are summarized in Table 4.4. At all periodic structures, w_{w} was set to 0.24 mm, w_{n} was set to 0.13 mm, s was set to 0.12 mm, Λ was set to 1.0 mm, and a was to 0.5 mm. By the change of d_{c}, the proposed periodic structure, to evaluate the DM crosstalk-reduction mechanism. And, the inductance and capacitance matrices of the proposed periodic structures in Table 4.4 are extracted by ANSYS Q3D Extractor ($l = 10$ mm) for analyzing DM crosstalk of two adjacent differential pairs by Eqs. (4.44) and (4.45).

Table 4.4 Periodic structural parameters for investigating the reduction mechanism of crosstalk.

Item	Value	Unit
w_{w}	0.24	mm
w_{n}	0.13	mm
s	0.12	mm
Λ	1	mm
a	0.5	mm
l	50	mm
d	0.13 / 0.27 / 0.42	mm
d_{c}	0.73 / 0.87 / 1.02	mm

FEXT in DMs

First, the FEXT in DMs was evaluated using these three types of structures, as shown in Table 4.4. As mentioned earlier, FEXT greatly depends on ΔK, which is the difference between $\varepsilon^{\mathrm{e}}_{\mathrm{reffd}}$ and $\varepsilon^{\mathrm{o}}_{\mathrm{reffd}}$. According to Eq. (4.47), ΔK also depend on ($|L_{\mathrm{dd12}}|$ - $|C_{\mathrm{dd12}}|$). Therefore, ΔK can be minimized when L_{dd12} and C_{dd12} are both 0 or $|L_{\mathrm{dd12}}|$ and $|C_{\mathrm{dd12}}Z_{\mathrm{d}}^2|$ are equal.

Figure 4.29 shows FEXT($|S_{\mathrm{dd41}}|$) and the solid lines denote the full-wave simulation at frequencies ranging from 0.1 to 20 GHz. On the other hand, the broken lines are obtained from Eq. (4.45). And it is clear that the results obtained from Eq. (4.45) are almost in agreement with full-wave simulation. This means that the parameter extraction is valid.

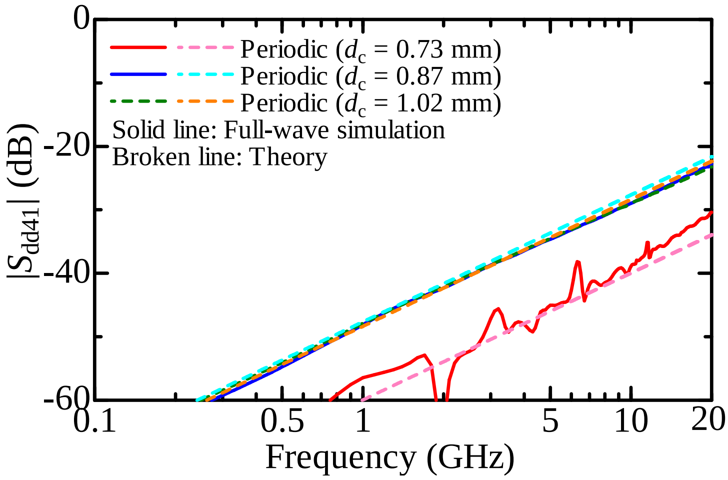

Figure 4.29 Comparison of FEXT characteristics between full-wave simulation and analytical result (periodic structure).

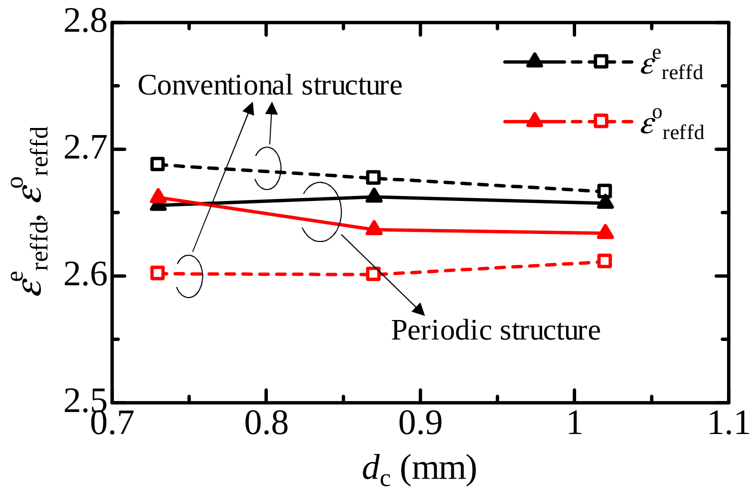

Figure 4.30 $\varepsilon^e_{\mathrm{reffd}}$ and $\varepsilon^o_{\mathrm{reffd}}$ as a function of distance d_c between the center lines of the adjacent differential pairs (conventional and periodic).

Therefore, we were able to explain the FEXT reduction mechanism by focusing on $\varepsilon^e_{\mathrm{reffd}}$, $\varepsilon^o_{\mathrm{reffd}}$, L_{dd12}, and C_{dd12}.

Figure 4.30 shows the $\varepsilon^e_{\mathrm{reffd}}$ and $\varepsilon^o_{\mathrm{reffd}}$ as a function of distance between the center lines of the adjacent differential pairs, d_c. The solid lines denote $\varepsilon^e_{\mathrm{reffd}}$ and $\varepsilon^o_{\mathrm{reffd}}$ of the periodic structures. On the other hand, the broken lines are obtained from conventional structures. The conventional structure shows that even if d_c increases, the difference between $\varepsilon^e_{\mathrm{reffd}}$, $\varepsilon^o_{\mathrm{reffd}}$ does not change significantly. However, using periodic structure the difference between $\varepsilon^e_{\mathrm{reffd}}$ and $\varepsilon^o_{\mathrm{reffd}}$ is minimized with d_c decreases. This is because the decrease of FEXT is not entirely dependent on the increase of distance d_c between the

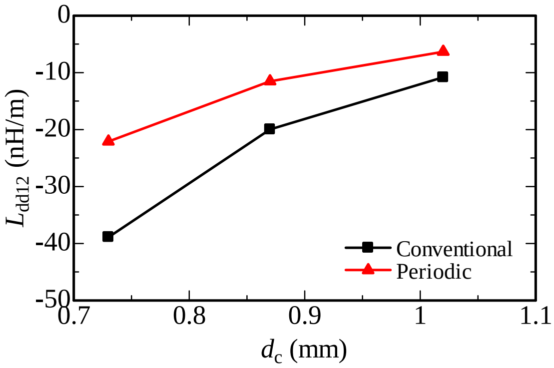

(a) Change in L_{dd12} as a function of d_{c}

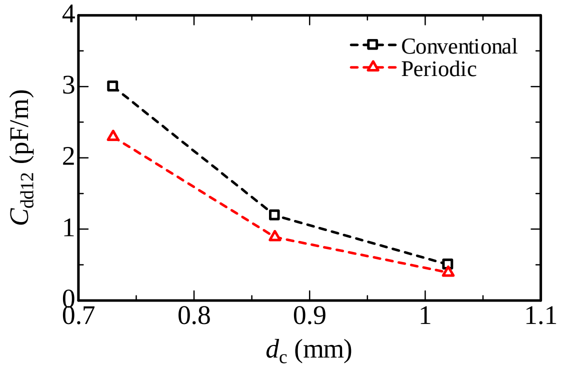

(b) Change in C_{dd12} as a function of d_{c}

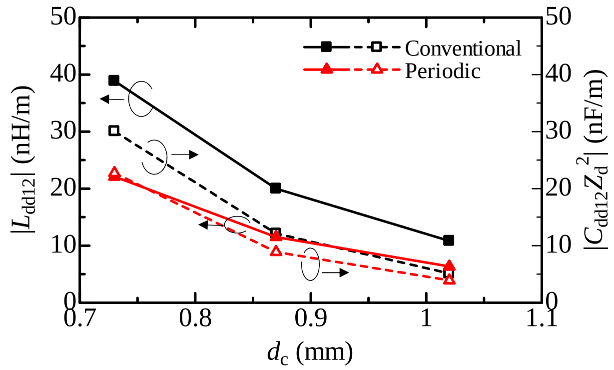

(c) Difference between $|L_{\mathrm{dd12}}|$ and $|C_{\mathrm{dd12}} Z_{\mathrm{d}}^2|$

Figure 4.31 Crosstalk modal coupling L_{dd12} and C_{dd12} between the DMs (conventional and periodic).

center lines of the adjacent differential pairs but also on ($|L_{\mathrm{dd12}}|$ - $|C_{\mathrm{dd12}} Z_{\mathrm{d}}^2|$).

Next, Figs. 4.31(a) and (b) show the crosstalk modal coupling L_{dd12} and C_{dd12} between the CMs and also compared conventional structure and periodic structure. As a result, L_{dd12} and C_{dd12} of the periodic structure are smaller than that of the conventional structure. Therefore, it is found that the periodic structure can reduce the crosstalk modal coupling. Moreover, for the periodic structure, reduce the amount of L_{dd12} is more than that of C_{dd12}. When d_{c} is 0.73 mm, $|L_{\mathrm{dd12}}|$ is almost equal to $|C_{\mathrm{dd12}} Z_{\mathrm{d}}^2|$ lead to FEXT can be minimized, as shown in Fig. 4.31(c).

NEXT in DMs

Then, the NEXT in DMs was evaluated using these three types of structures, as shown in Table 4.4. According to Eq. (4.44), NEXT greatly depends on ΔZ, which is the difference between $Z_{\mathrm{d}}^{\mathrm{e}}$ and $Z_{\mathrm{d}}^{\mathrm{o}}$. With the increase of d_{c}, L_{dd12} and C_{dd12} will decrease, as shown in Figs. 4.17(a) and (b). Therefore, the difference between $Z_{\mathrm{d}}^{\mathrm{e}}$ and $Z_{\mathrm{d}}^{\mathrm{o}}$ decreases with it. This is because the NEXT in DMs only dependent on ($|L_{\mathrm{dd12}}| + |C_{\mathrm{dd12}} Z_{\mathrm{d}}^2|$). Refer to Eq. 4.46.

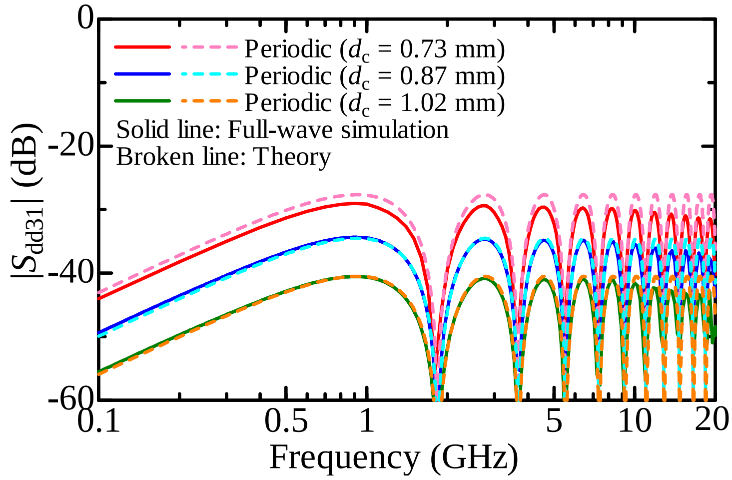

Figure 4.32 Comparison of NEXT characteristics between full-wave simulation and analytical result (periodic structure).

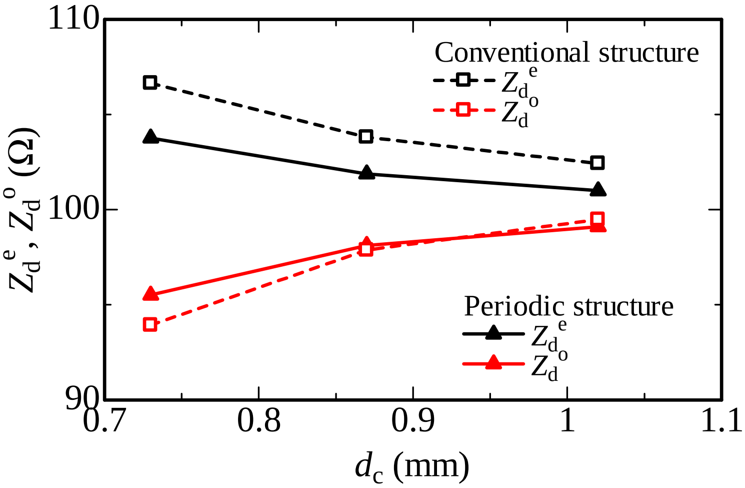

Figure 4.33 Z_d^e and Z_d^o as a function of d_c (conventional and periodic).

Figure 4.32 shows NEXT($|S_{\mathrm{dd}31}|$) and the solid lines denote the full-wave simulation at frequencies ranging from 0.1 to 20 GHz. On the other hand, the broken lines are obtained from Eq. (4.44). And it is clear that the results obtained from the theoretical formula of this research are almost in agreement with full-wave simulation.

Figure 4.33 shows the Z_d^e and Z_d^o as a function of distance between the center lines of the adjacent differential pairs, d_c. The solid lines denote Z_d^e and Z_d^o of the periodic structures. On the other hand, the broken lines indicate Z_d^e and Z_d^o of the conventional structures. As a result, the difference between Z_d^e and Z_d^o of the periodic structures is smaller than that of the conventional structures. This is because $L_{\mathrm{dd}12}$ and $C_{\mathrm{dd}12}$ of the periodic structure are smaller than that of the conventional structure, as shown in

Figs. 4.31(a) and (b).

4.6 Conclusion

In this chapter, the mechanisms of crosstalk occurring in adjacent differential pairs were investigated by combining modal analysis, multi-conductor transmission line theory, and the simplifying assumptions of weak coupling. For the five-conductor transmission line, we expand the crosstalk theory to computed for differential-mode crosstalk between neighboring differential pairs to easily calculated for NEXT and FEXT in DM by introducing the concept of odd- and even-mode DMs. And have also shown the validity of computed formulas. According to computed formulas for NEXT and FEXT in DM, it is found that NEXT greatly depends on the difference between the even- and odd-mode characteristic impedances in DMs, and FEXT greatly depends on the difference between the even- and odd-mode relative effective dielectric constants in DMs. And the difference between the even- and odd-mode characteristic impedances and relative effective dielectric constants in DMs greatly depends on the modal coupling L_{dd12} and C_{dd12}. Because the relationship between L_{dd12} and C_{dd12} is always positive and negative. Therefore, L_{dd12} and C_{dd12} have an additive relationship, while the subtractive relationship between L_{dd12} and C_{dd12}. FEXT can be minimized when L_{dd12} and C_{dd12} are both 0 or $|L_{\mathrm{dd12}}|$ and $|C_{\mathrm{dd12}}Z_{\mathrm{d}}^2|$ are equal, while NEXT must be L_{dd12} and C_{dd12} are both 0.

We focus on the crosstalk problem that occurs in the dense line part of the differential transmission system used for high-speed signal transmission and proposed to provide a concave and convex periodic structure on the differential line to suppress the crosstalk. And computed formulas for NEXT and FEXT in DM have used evaluation of the crosstalk-reduction mechanism of the periodic structure. As a result of FXET, L_{dd12} and C_{dd12} of the periodic structure are smaller than that of the conventional structure. Therefore, it is found that the periodic structure can reduce the crosstalk modal coupling. Moreover, for the periodic structure, reduce the amount of L_{dd12} is more than that of C_{dd12}. When d_{c} is 0.73 mm, $|L_{\mathrm{dd12}}|$ is almost equal to $|C_{\mathrm{dd12}}Z_{\mathrm{d}}^2|$ lead to FEXT can be minimized. As a result of NEXT, the difference between $Z_{\mathrm{d}}^{\mathrm{e}}$ and $Z_{\mathrm{d}}^{\mathrm{o}}$ of the periodic structures is smaller than that of the conventional structures. This is because the periodic structure can reduce the crosstalk modal coupling. Also, the validity of the proposed periodic structure was confirmed by verified experimentally as well.

Chapter 5

General Conclusion

In this thesis, the author focuses on the asymmetry, or imbalance, of the high-speed differential transmission lines on PCBs, lead to common-mode noise, skew, and crosstalk, as following :

(A) common-mode noise generated at a bend of the differential transmission lines.

(B) differential skew caused by different effective relative permittivity around each line of differential transmission lines.

(C) differential mode crosstalk between adjacent differential pairs.

The main objective of this thesis is to elucidate the mechanism of EMC and SI issues of (A), (B), and (C), and it is to propose a design of high SI and low common-mode noise transmission lines.

In Chapter 2, the author (assuming as high-density wiring) proposed a tightly coupled asymmetrically tapered bend that limits the bend structure within the area of the conventional bend and its design methodology. First, a geometrical path difference of the asymmetric taper part was defined, the setting of the taper formation conditions and the calculation formula of the structural parameter was derived. Next, by reducing the line width and line separation of the tightly coupled bend, the geometric path difference and the effective path difference were matched, and it was shown that the characteristics as designed were obtained. Then, using 3D electromagnetic simulation and measurement evaluated the 45 degree-angle bend formed based on our design methodology and found that the differential-to-common mode conversion was decreased by almost 20 dB and maintain its transmission characteristics compared to those of the conventional bend. Furthermore, when compared with the compensation method proposed in other documents, the high-density wiring is clearly superior, and the simulation results show that the mode conversion amount (Forward and backward differential-to-common mode conversion) and the propagation characteristics (Differential-mode reflection and transmission coefficient) is equal or superior to those of other structures. From the above, it can be said that the proposed structure is a bent structure with an extremely small mode conversion suitable for high-density wiring.

Chapter 3 described two mesh ground structures that do not affect the differential skew and characteristic impedance of the differential line. First, the author focuses on the angle between the trace of the differential lines and the meshed ground plane and investigates the angle dependence of the differential skew, taking into account phase delay between two lines with propagation to find low differential skew at the angle other than 45°. A simple model was proposed for reducing the calculation time but is found to be able to evaluate the angle dependence of the differential skew at a similar accuracy to the 3D electromagnetic simulation. As a result, it is found that the differential skew does not depend on the position of the differential lines to the meshed ground and keeps a comparatively small value at the angle between 30° and 40°. the author also proposed a design wherein the meshed ground is rotated by 30° with a 90° bend in the differential transmission lines. We compared this design with a general design that has 45°-bend differential transmission lines and meshed ground. Our proposed design is unaffected by the position of the lines relative to the meshed ground, enabling improved wiring density. Further, our design is better for the differential-mode transmission characteristics than the general design, which demands high symmetry. From the above results, it is found that the rotated meshed ground keeps the differential skew small by making the phase difference between the two lines irregular at each mesh pitch. In this thesis, we also show that the irregular phase difference by shifting the mesh position randomly does not affect the characteristic impedance nor differential skew in terms of the wiring position.

In Chapter 4, the mechanisms of crosstalk occurring in adjacent differential pairs were investigated by combining modal analysis, multi-conductor transmission line theory, and the simplifying assumptions of weak coupling. For the five-conductor transmission line, we expand the crosstalk theory to computed for differential-mode crosstalk between neighboring differential pairs to easily calculated for NEXT and FEXT in DM by introducing the concept of odd- and even-mode DMs. And have also shown the validity of computed formulas. According to computed formulas for NEXT and FEXT in DM, it is found that NEXT greatly depends on the difference between the even- and odd-mode characteristic impedances in DMs, and FEXT greatly depends on the difference between the even- and odd-mode relative effective dielectric constants in DMs. And the difference between the even- and odd-mode characteristic impedances and relative effective dielectric constants in DMs greatly depends on the modal coupling L_{dd12} and C_{dd12}. Because the relationship between L_{dd12} and C_{dd12} is always positive and negative. Therefore, L_{dd12} and C_{dd12} have an additive relationship, while the subtractive relationship between L_{dd12} and C_{dd12}. FEXT can be minimized when L_{dd12} and C_{dd12} are both 0 or $|L_{\mathrm{dd12}}|$ and $|C_{\mathrm{dd12}}Z_{\mathrm{d}}^{2}|$ are equal, while NEXT must be L_{dd12} and C_{dd12} are both 0. Then, in this chapter examined the introduction of a periodic structure into both outsides of a differential pair to reduce crosstalk. The effect of its crosstalk reduction was evaluated, and the reduction mechanism was clarified. As a result of NEXT, the difference between $Z_{\mathrm{d}}^{\mathrm{e}}$ and $Z_{\mathrm{d}}^{\mathrm{o}}$ of the periodic structures is smaller than that of the conventional structures. This is because the periodic structure can reduce the crosstalk modal coupling. As a result of FEXT, L_{dd12} and C_{dd12} of the periodic structure are smaller than that of the conventional structure. Therefore, it is found that the periodic structure can reduce the crosstalk modal coupling. Moreover, for the periodic structure, reduce the amount of L_{dd12} is more than that of C_{dd12}. When d_{c} is 0.73 mm, $|L_{\mathrm{dd12}}|$ is almost equal to $|C_{\mathrm{dd12}} Z_{\mathrm{d}}^2|$ lead to FEXT can be minimized, and as a result, far-end crosstalk could be reduced to 0 theoretically without changing d_{c}.

As mentioned above, in each study, a method for realizing high SI and low common-mode noise design was proposed, and its validity was demonstrated. The innovation presented in this thesis is useful for designing next-generation the high-speed signal transmission system of PCBs.

Appendix A

Effective Relative Dielectric Constant Calculation Method

$\varepsilon_{\text{reff1}}$ and $\varepsilon_{\text{reff2}}$ shown in Table 3.1 are values obtained from the cross-sectional structure of the single-ended wiring in Fig. A.1. In the 2D electrostatic field calculation, ANSYS

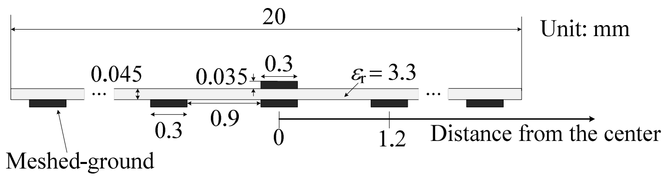

Figure A.1 Position of single-ended wiring.

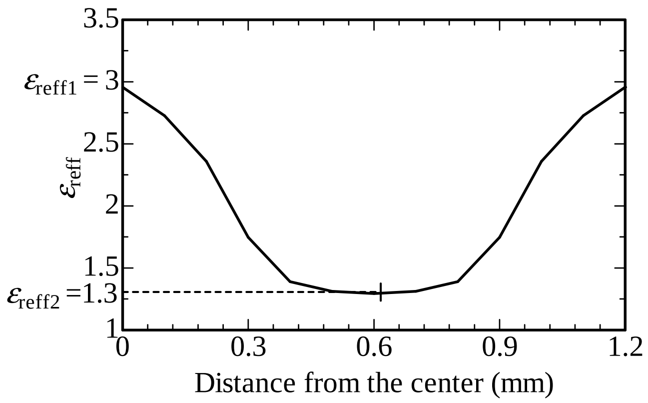

Figure A.2 Position dependence of effective relative dielectric constant.

2D Extractor was used to calculate the effective relative dielectric constant while shifting the wiring position from 0 mm as shown in Fig. A.1. The results are shown in Fig. A.2. For simplicity, $\varepsilon_{\text{reff1}}$ and $\varepsilon_{\text{reff2}}$ adopted the maximum value of 3.0 and the minimum value of 1.3 as effective relative permittivity, respectively, and used them for calculations using a simple model. There is room for consideration in the calculation of the effective relative dielectric constant adopted here. This is a future issue.

Appendix B

Optimum Rotation Angle for Mitigating Differential Skew Induced by Glass Cloth in PCBs

PCBs are generally constructed with various glass fibers saturated in epoxy resin. Since relative permittivity ε_{r1} of the glass fibers is about 6 and relative permittivity ε_{r2} of the epoxy resin is about 3, the distribution of the epoxy resin and the glass cloth around each differential transmission line causes a phase difference (Fig. B.1) that leads to a differential skew. In high-speed signal transmissions, differential skew induced by the glass cloth is one of the important factors that cause the deterioration of signal quality [1]-[6].

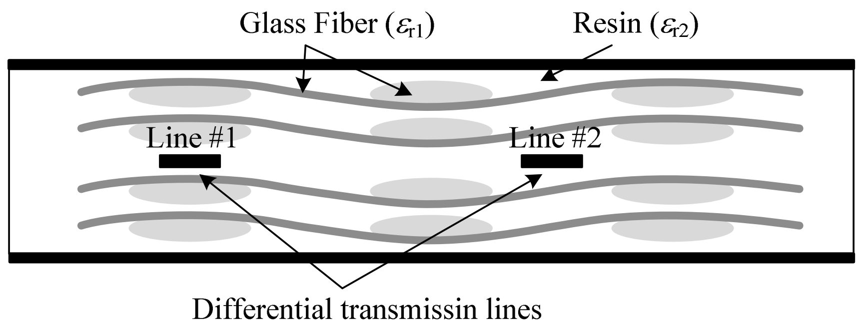

Figure B.1 Cross-sectional view of glass cloth in PCB.

In high-speed signal transmissions, glass cloth of the dielectric in printed circuit boards can cause a differential skew. It has been reported that the differential skew is mitigated when the angle between the differential transmission lines and the thread of the glass cloth is around 10°. However, the angle dependence between 10° and 45° and the optimum angle have not yet been investigated. This study focuses on the angle between the trace of the differential transmission lines and the thread of the glass cloth to investigate the angle dependence of the differential skew. We conducted a preliminary evaluation by analytical

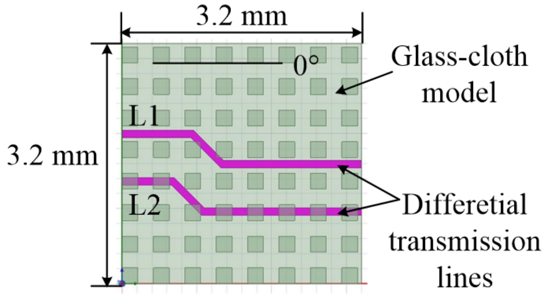

(a) No rotation, 45° bend

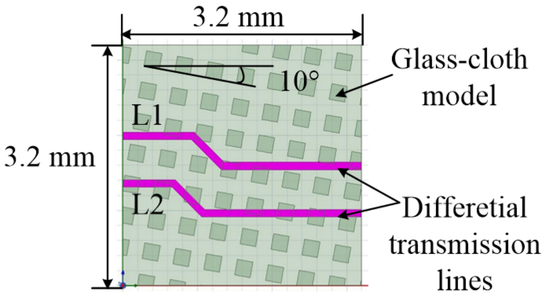

(b) 10° rotation, 45° bend

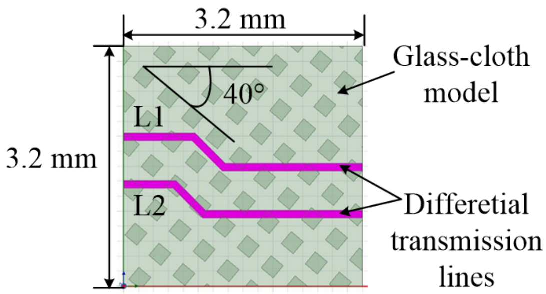

(c) 40° rotation, 45° bend

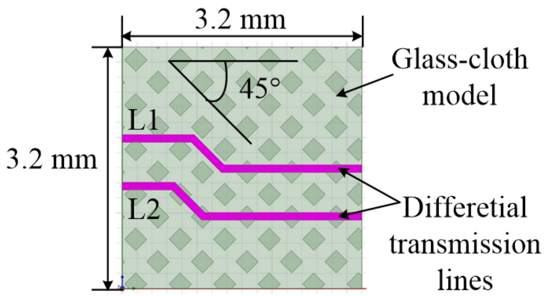

(d) 45° rotation, 45° bend

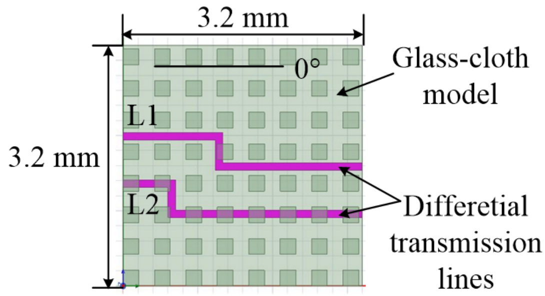

(e) No rotation, 90° bend

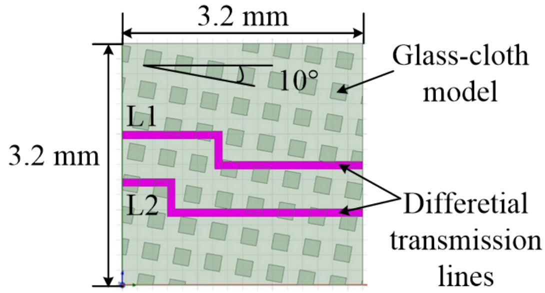

(f) 10° rotation, 90° bend

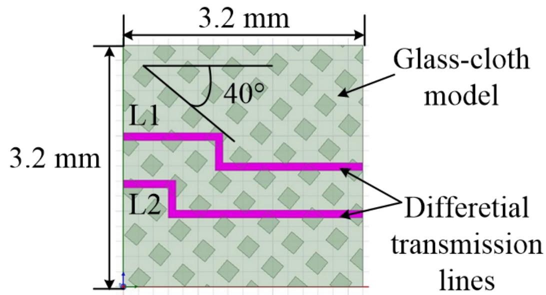

(g) 40° rotation, 90° bend

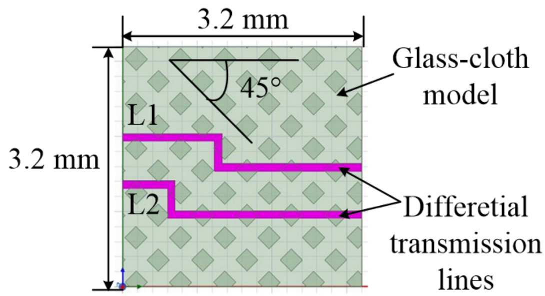

(h) 45° rotation, 90° bend

Figure B.2 Simulation models with different rotation angles and different bend angles evaluated by full-wave simulation.

estimation of the phase delay difference in the differential transmission lines using our simple model (as shown in Section 3.2) for glass-cloth. And it is obtained the same results (the optimum angle between 30° and 40°) as in Section 3.2.

We present the results (using rotation angle 40°) validated by a full-wave simulation

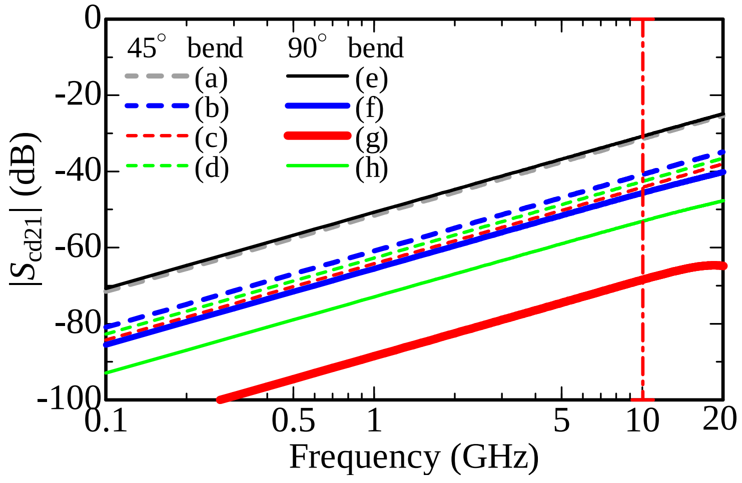

Figure B.3 Differential-to-common mode conversion coefficient.

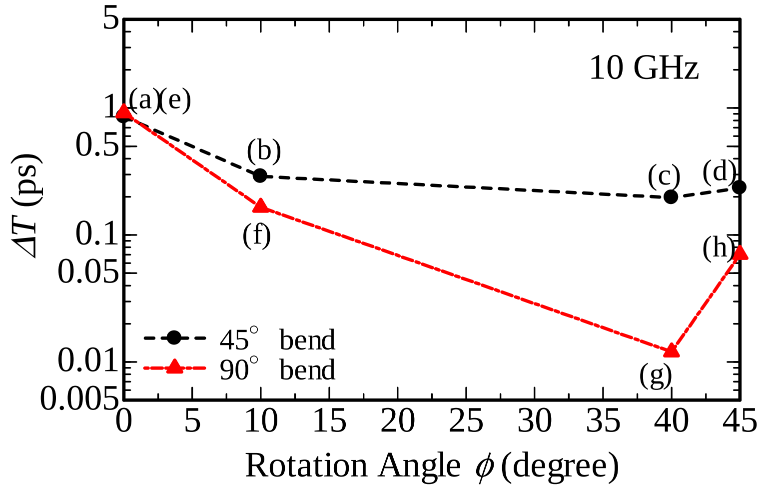

Figure B.4 Rotation angle ϕ dependence of ΔT at 10 GHz.

using a commercial simulator ANSYS HFSS. However, the 45° bend that is usually used in wiring does not always keep the angle of the thread in the glass cloth with the lines at 40°. To the contrary, a 90° bend can always keep the angle with the lines at 40°. Therefore, the bend angles of 45° and 90° were used for comparison. Figs. B.2(a) to (d) show the simulation for 45° bend and Figs. B.2(e) to (h) show the simulation for 90° bend. Also, in (a) and (e) the differential transmission lines are along the thread of the glass cloth, in (b) and (f) the rotation angle is 10°, in (c) and (g) it is 40°, and in (d) and (h) it is 45°.

As shown in the previous Section 3.2, a long line is unnecessary, except for a specific angle in a simulation. Therefore, the dimensions of the test board were set to 3.2 × 3.2 mm^2 to keep the calculation cost down.

Fig. B.3 shows the simulation results of the differential-to-common mode conversion amount $|S_{\mathrm{cd21}}|$ obtained by a full-wave simulation. Since $|S_{\mathrm{cd21}}|$ is generally proportional to frequency, the slopes of Fig. B.3 are constant at 20 dB/dec. regardless of the bend structure. Therefore, let us now focus on 10 GHz. The propagation time difference ΔT is calculated from $|S_{\mathrm{cd21}}|$ using Eq. (3.9) and hence the dependence of ΔT on the rotation angle ϕ at 10 GHz is shown in Fig. B.4.

As shown in Fig. B.4, regardless of the bend structure, ΔT is minimized at the rotation angle ϕ of 40°, which confirms the results in the previous section. When comparing 45° and 90° bends, the 90° bend reduces ΔT because it can keep the angle between the differential transmission lines and the thread of the glass cloth at 40°. As a result, ΔT in simulation (g) is approximately 17 times smaller than that in simulation (c). Thus, it can be suggested that the differential skew can be suppressed.

Appendix C

Crosstalk Suppression Effect When Decrease Number of Periodic Structures

Length l of the proposed periodic structure line decrease to 10 mm is used for evaluation by full-wave simulation (commercial simulator, ANSYS HFSS), and their structural parameters are summarized in Table C.1.

Table C.1 Conventional and periodic structural model parameters.

Item	Conventional	Periodic structure	Unit
w	0.21	-	mm
w_{w}	-	0.24	mm
w_{n}	-	0.13	mm
s	0.15	0.12	mm
Λ	-	1	mm
a	-	0.5	mm
l	10	10	mm
d	0.16	0.13	mm
d_{c}	0.73	0.73	mm

Figure C.1 shows a comparison of crosstalk characteristics between conventional and periodic structures when line length $\mathrm{l} = 10$ mm. As shown in Fig. C.1(a), the NEXT($|S_{\mathrm{dd31}}|$)was reduced by about 5 dB compared to the conventional differential pairs by introducing the periodic structure. And, in Fig. C.1(b), the FEXT($|S_{\mathrm{dd41}}|$)was reduced by 16 dB or more compared to the conventional differential pairs by introducing the periodic structure. As a result, it is found that although the number of the periodic structure was reduced, the suppression effect of crosstalk was not greatly affected compared with the conventional structure.

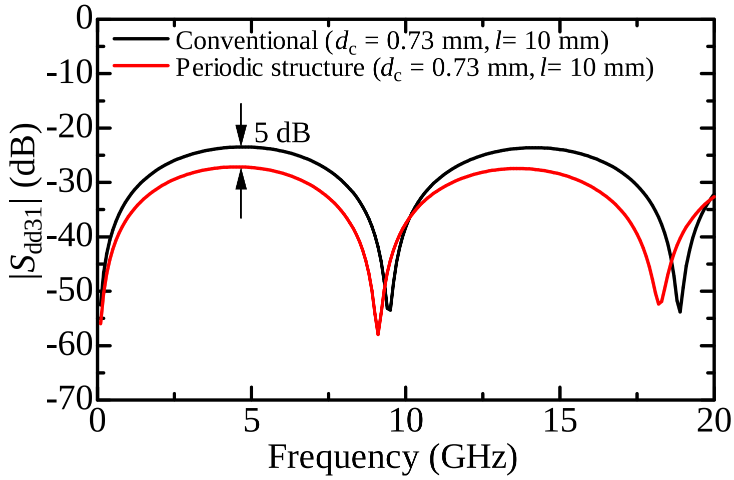

(a) NEXT

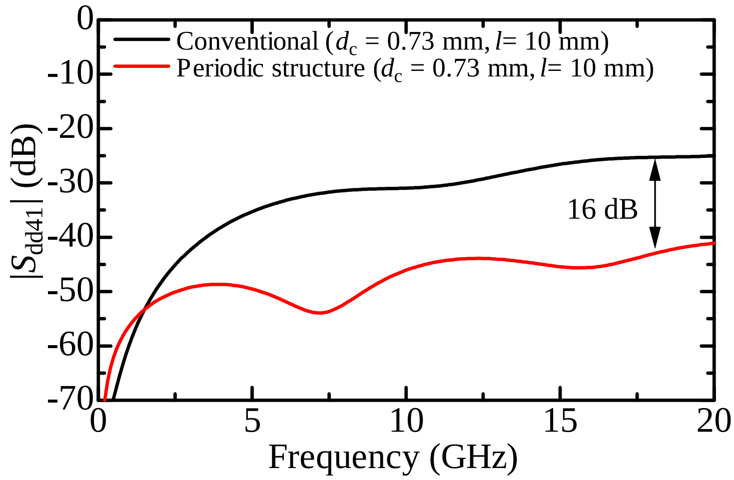

(b) FEXT

Figure C.1 Comparison of crosstalk characteristics between conventional and periodic structures (l =10 mm).

Bibliography

[1] M. S. Sharawi, “Practical issues in high speed PCB design,”IEEE Potentials, vol. 23, no. 2, pp. 24-27, May 2004.

[2] C. R. Paul, Introduction to Electromagnetic Compatibility, 2nd ed. New York: Wiley, 2008.

[3] C. R. Paul, Analysis of Multiconductor Transmission Lines, 2nd ed. NEW York: Wiley, 2009.

[4] J. A. B. Faria, Multiconductor Transmission-Line Structures: Modal Analysis Techniques. New York: John Wiley & Sons, 1993.

[5] C. R. Paul, Analysis of Multiconductor Transmission Lines. New York: John Wiley & Sons, 1994.

[6] T. L. Wu, F. Buesink, and F. Canavero, “Overview of signal integrity and EMC design technologies on PCB: fundamentals and latest progress,”IEEE Trans. Electromagn. Compat., vol. 55, no. 4, pp. 624-638, Aug. 2013.

[7] D. Oh, A. Abbasfar, L. Luo, J.-H. Kim, R. Schmitt, F. Ware, J. Wilson, and C. Yuan, “Pseudo-differential vector signaling for noise reduction in single-ended signaling systems,”presented at the DesignCon 2009, Santa Clara, CA, Feb. 2009.

[8] S. Smith, S. Agili, and V. Balasubramanian, “Theory and measurement of unbalanced differential-mode transmission lines,”presented at the DesignCon 2006, Santa Clara, CA, Feb. 2006.

[9] J. Jeong, I. Hong, and R. Nevels, “The time domain propagator method for lossless multiconductor quasi-TEM lines,”IEEE Trans. Adv. Packag., vol. 32, no. 3, pp. 619-626, Aug. 2009.

[10] A. G. Chiariello, A. Maffucci, G. Miano, F. Villone, and W. Zamboni, “A transmission-line model for full-wave analysis of mixed-mode propagation,”IEEE Trans. Adv. Packag., vol. 31, no. 2, pp. 275-284, May 2008.

[11] H. Ott, Noise Reduction Techniques in Electronic Systems, 2nd ed. New York: Wiley, 1988.

[12] S. Wu, C. Tsai, T. Wu, and T. Itoh, “A novel wideband common-mode suppression filter for Gigahertz differential signals using coupled patterned ground structure,”IEEE Trans. Microw. Theory Tech., vol. 57, no. 4, pp. 848-855, Apr. 2009.

[13] L. B. Gravelle and P. F. Wilson, “EMI/EMC in printed circuit boards-a literature review,”IEEE Trans. Electromagn. Compat., vol. 34, no. 2, pp. 109-116, May 1992.

[14] D. M. Hockanson, J. L. Drewniak, T. H. Hubing, T. P. Van Doren, F. Sha, and M. J. Wilhelm, “Investigation of fundamental EMI source mechanisms driving common-mode radiation from printed circuit boards with attached cables,”IEEE Trans. Electromagn. Compat., vol. 38, no. 4, pp. 557-566, Nov. 1996.

[15] D. A. Hill, D. G. Camell, K. H. Cavcey, and G. H. Koepke, “Radiated emissions and immunity of microstrip transmission lines:theory and reverberation chamber measurements,”IEEE Trans. Electromagn. Compat., vol. 38, no. 2, pp. 165-172, May 1996.

[16] C. R. Paul and D. R. Bush, “Radiated emission from common-mode currents,”in Proc. IEEE Int. Symp. Electromagnetic Compatibility, Atlanta, GA, USA, pp. 197-203, Aug. 1987.

[17] S. H. Hall and H. L. Heck, Advanced Signal Integrity for High-Speed Digital System Design. Hoboken, NJ, USA: Wiley, 2009.

[18] G.-H. Shiue, W.-D. Guo, C.-M. Lin, and R.-B. Wu, “Noise reduction using compensation capacitance for bend discontinuities of differential transmission lines,”IEEE Trans. Adv. Packag., vol. 29, no. 3, pp. 560-569, Aug. 2006.

[19] H. R. Goodarzi, M. Tayarani, and S. Khosravi, “Differential to common mode coupling in microstrip lines; calculation and improvement,”in Proc. 18th Int. Zurich Symp. Electromagn. Compatibil., pp. 293-296, Sep. 2007.

[20] S. Connor, B. Archambeault, and M. Mondal, “The impact of common mode currents on signal integrity and EMI in high-speed differential data links,”in IEEE Int. Symp. Electromagn. Compatibil., pp. 680-684, Aug. 2008.

[21] X. Duan, B. Archambeault, H.-D. Bruens, and C. Schuster, “EM emission of differential signals across connected printed circuit boards in the GHz range,”in Proc. IEEE Int. Symp. Electromagn. Compat., Austin, TX, USA, pp. 50-55, Aug. 2009.

[22] W.-T. Liu, C.-H. Tsai, T.-W. Han, and T.-L. Wu, “An embedded common-mode suppression filter for GHz differential signals using periodic defected ground plane,”IEEE Microw. Wireless Compon. Lett., vol. 18, no. 4, pp. 248-250, Apr. 2008.

[23] J. Naqui, A. Fernandez-Prieto, M. Duran-Sindreu, F. Mesa, J. Martel, F. Medina, and F. Martin, "Common-mode suppression in microstrip differential lines by means of complementary split ring resonators: Theory and applications,"IEEE Trans. Microw. Theory Techn., vol. 60, no. 10, pp. 3023-3034, Oct. 2012.

[24] S. Oh, J. Jeong, and J. Lee, "Wideband common noise suppression filter based on coupled microstrip lines and edge-coupled coplanar waveguides,"Electron. Lett., vol. 51, no. 25, pp. 2123-2124, 2015.

[25] C.-H. Chang, R.-Y. Fang, and C.-L. Wang, "Bended differential transmission line using compensation inductance for common-mode noise suppression,"IEEE Trans. Compon., Packag., Manuf. Technol., vol. 2, no. 9, pp. 1518-1525, Sep. 2012.

[26] M. A. Khorrami, "Noise Reduction of Bended Differential Transmission Lines Using Compensation Capacitance,"in Proc. IEEE Int. Symp. Electromag. Compat., pp.150-155, Aug. 2013.

[27] L.-S. Wu, J.-F. Mao, and W.-Y. Yin, "Slow-wave structure to suppress differential-to-common mode conversion for bend discontinuity of differential signaling,"in Proc. IEEE Elect. Design Adv. Packag. Syst. Symp., pp. 219-222, Taipei, China, Dec. 2012.

[28] D.-B. Lin, C.-P. Huang, and H.-N. Ke, "Using stepped-impedance lines for common-mode noise reduction on bended coupled transmission lines,"IEEE Trans. Compon., Packag., Manuf. Technol., vol. 6, no. 5, pp. 757-766, May 2016.

[29] B.-R. Huang, C.-H. Chang, R.-Y. Fang, and C.-L. Wang, "Commonmode noise reduction using asymmetric coupled line with SMD capacitor,"IEEE Trans. Compon., Packag., Manuf. Technol., vol. 4, no. 6, pp. 1082-1089, Jun. 2014.

[30] C. Gazda, D.V. Ginste, H. Rogier, R.-B. Wu, and D. De Zutter, "A wideband common-mode suppression filter for bend discontinuities in differential signaling using tightly coupled microstrips,"IEEE Trans. Adv. Packag., vol.33, no.4, pp.969-978, Nov. 2010.

[31] C. Gazda, D.V. Ginste, H. Rogier, D. De Zutter, and R.-B. Wu, "Time domain analysis of a wideband common-mode suppression filter for bent interconnects,"Proc. 2011 IEEE 15th Workshop on Signal Propagation on Interconnects (SPI), pp.7-10, May 2011.

[32] C. Gazda, I. Couckuyt, H. Rogier, D.V. Ginste, and T. Dhaene, "Constrained multiobjective optimization of a common-mode suppression filter,"IEEE Trans. Electromagn. Compat., vol.54, no.3, pp.704-707, June 2012.

[33] C. Gazda, H. Rogier, D.V. Ginste, I. Couckuyt, and T. Dhaene, "Time domain analysis of a common-mode suppression filter subjected to a multi-objective optimization,"Proc. EMC Europe 2012, pp.17-21, Sept. 2012.

[34] H. Heck, S. Hall, B. Horine, K. Mallory, T. Wig, "Impact of FR4 dielectric nonuniformity on the performance of multi-Gb/s differential signals,"Proc. Electrical Performance of Electronic Packaging 2003, pp. 243-246, Oct. 2003.

[35] H. Heck, S. Hall, B. Horine, K. Mallory, T. Wig, "Modeling and mitigating AC common mode conversion in Multi-Gb/s differential printed circuit boards,"Electrical Performance of Electronic Packaging, pp. 29-32, Oct. 2004.

[36] J. R. Miller, G. J. Blando, I. Novak, "Additional Trace Losses due to Glass-Weave Periodic Loading,"DesignCon 2010.

[37] G. Romo, C. Nwachukwu, R. Torres-Torres, S.-W. Baek, M. Schauer, "Stack-up and routing optimization by understanding micro-scale PCB effects,"DesignCon 2011.

[38] M. Schauer, G. Romo Luevano, R. Torres-Torres, C. Nwachukwu, S.-W. Baek, "Understanding and mitigation of fiber weave effects in striplines,"DesignCon 2012.

[39] T. Fukumori, H. Nagaoka, D. Mizutani, and M. Tani, "Simulation of differential skew considering fiber kink effects,"Proc. IEEE CPMT Symposium Japan (ICSJ) 2014, IEEE 4th, no. 05-2, pp. 43-46, Kyoto, Japan, Nov. 2014.

[40] T. Fukumori, T. Akahoshi, D. Mizutani, and M. Tani, "Method for Mitigating Weave-Induced Skew in PWBs for High-Speed Signal Transmission,"IEICE Trans. Electron, Vol. J98-C, No. 11, pp. 262-267, 2015. (in Japanese)

[41] P. Pathmanathan, C. M. Jones, S. G. Pytel, D. L. Edgar, P. G. Huray, "Power loss due to periodic structures in high-speed packages and printed circuit boards,"in Proc. of 18th European Microelectronics Packaging Conf., 2011.

[42] R. Torres-Torres, G. Romo, M. Schauer, C. Nwachukwu, S.-W. Baek, "Modeling resonances in transmission lines fabricated over woven fiber substrates,"IEEE Trans. on MTT, v. 61, N 7, p. 2558-2565, 2013.

[43] J. Loyer, R. Kunze, X. Ye, "Fiber weave effect: Practical impact analysis and mitigation strategies,"Proc. DesignCon 2007, no.6-TA2, Santa Clara, California, US, Jan.-Feb. 2007.

[44] T. Ogawa, H. Watanabe, S. Nikaido, "An investigation of differential impedance controlled flexible printed circuit,"Fujikura Technical Journal, No. 114, pp. 32-34, 2010.

[45] Y. T. Zhu, F. C. Xiao, X. Y. Sun, Y. Kayano, Y. Kami, "Investigation on characteristic impedance of differential transmission line in meshed-ground flexible printed circuit,"IEICE Technical Report, EMCJ2016-121, Mar. 2017.

[46] S. Wu, H. Shi, M. Herndon, B. Cornelius, M. Halligan, and J. Fan, “Modeling and analysis of a trace referenced to a meshed ground plane,”in Proc. IEEE Int. Symp. Electromagn. Compat., pp. 137-141, Aug. 2011.

[47] S. K. S. Hsu, Y. C. Pai, and P. C. Hsieh, “A novel flexible printed circuit structure for gigabit data transmission,”in Proc. Electrical Design of Adv. Packag. Sys. Symp., pp.153-156, IEEE, 2012.

[48] D. A. Hill, K. H. Cavcey, and R. T. Johnk, “Crosstalk between microstrip transmission lines,”IEEE Trans. Electromagn. Compat., Vol.36, No.4, pp.314-321, Nov. 1994.

[49] Y. Okawa, F. Xiao, Y. Kami, “Crosstalk Between Two Sets of Differential Signaling,”IEICE General Conference, B-4-55, 2011.3.

[50] D. J. Riley and L. D. Bacon, “On the limitation of the weak-coupling assumption for crosstalk analysis based on quasi-TEM propagation,”IEEE Trans. Electromagn. Compat., vol. 32, no. 1, pp. 28-37, Feb. 1990.

[51] R. B. Wu and F. L. Chao, “Laddering wave in serpentine delay line,”IEEE Trans. Compon. Packag., Manuf. Technol., vol. 18, no. 4, pp. 644-650, Nov. 1995.

[52] J. S. Sohn, J. C. Lee, H. J. Park, and S. I. Cho, “Empirical equations on electrical parameters of coupled microstrip lines for crosstalk estimation in printed circuit board,”IEEE Trans. Adv. Packag., vol. 24, no. 4, pp. 521-527, Nov. 2001.

[53] P. Muthana and H. Kroger, “Behavior of short pulses on tightly coupled microstrip lines and reduction of crosstalk by using overlying dielectric,”IEEE Trans. Adv. Packag., vol. 30, no. 2, pp. 511-520, Aug. 2007.

[54] F. D. Mbairi,W. P. Siebert, and H. Hesselbom, “High-frequency transmission lines crosstalk reduction using spacing rules,”IEEE Trans. Compon. Packag. Technol., vol. 31, no. 3, pp. 601-610, Sep. 2008.

[55] K. Lee, H.-B. Lee, H.-K. Jung, J.-Y. Sim, and H.-J. Park, “A serpentine guard trace to reduce the far-end crosstalk voltage and the crosstalk induced jitter of parallel microstrip lines,”IEEE Trans. Adv. Packag., vol. 31, no. 4, pp. 809-817, Nov. 2008.

[56] R.-B. Sun, C.-Y. Wen, and R.-B. Wu, “A new isolation structure of pogo pins for crosstalk reduction in a test socket,”IEEE Trans.Compon. Packag. Technol., vol. 1, no. 4, pp. 586-594, Apr. 2011.

[57] Y.-S. Li, Y.-L. Xu, D.-C. Yang, J. Li, X.-C. Wei, and E.-P. Li, “A shielding structure for crosstalk reduction in silicon interposer,”IEEE Microw. Wireless Compon. Lett., vol. 26, no. 4, pp. 246-248, Apr. 2016.

[58] S. H. Hall, G.W. Hall, and J. A. McCall, High-Speed Digital System Design: A Handbook of Interconnect Theory and Design Practices. New York, NY, USA: Wiley, 2000.

[59] F. D. Mbairi, W. P. Siebert and H. Hesselbom "On the problem of using guard traces for high frequency differential lines crosstalk reduction,"IEEE Trans. Comp. Packag. Technol., vol. 30, no. 1, pp. 67-74, Mar. 2007.

[60] D. G. Kam, H. Lee, and J. Kim, "Twisted Differential Line Structure on High-Speed Printed Circuit Boards to Reduce Crosstalk and Radiated Emission,"IEEE Trans. Adv. Packag., vol. 27, no. 4, pp. 590-596, Aug. 2004.

[61] S. Kan, Y. Toyota, K. Iokibe, and T. Watanabe, "Suppression of Mode Conversion by Decreasing Path Difference by Using an Asymmetrically Tapered Bend in Differential Transmission Lines,"in proc. EMC'14/Tokyo, pp. 128-132, May 2014.

[62] Y. Toyota, S. Kan, K. Iokibe, "Suppression of Mode Conversion by Using Tightly Coupled Asymmetrically Tapered Bend in Differential Lines,"IEICE Trans. Commun., vol. E98-B, no. 7, pp.1188-1195, Jul. 2015.

[63] C. Wang, K. Iokibe, and Y. Toyota, "Tightly coupled asymmetrically tapered bend in differential transmission lines for high-density mounting,"IEICE technical report, EMCJ2015-39, pp.49-54, Jul. 2015. (in Japanese)

[64] C. Y. Wang, K. Iokibe, Y. Toyota, "Design Methodology of Tightly Coupled Asymmetrically Tapered Bend for High-density Mounting in Differential Transmission Lines,"2016 Asia-Pacific International Symposium on Electromagnetic Compatibility & Signal Integrity and Technical Exhibition (APEMC 2016), Shenzhen, China, pp.463-465, May 2016.

[65] C. Wang, K. Iokibe, and Y. Yoyota, "Optimum rotation angle for mitigating differential skew induced by glass cloth in PCBs,"in Proc. Int. Conf. Electron. Packag. iMAPS All Asia Conf., pp.328-332, Apr. 2018.

[66] C. Wang, K. Iokibe, and Y. Toyota, "Evaluation of differential skew depending on rotation angle in printed circuit board with meshed ground plane,"IEICE technical report, EMCJ2017-109, pp.25-30, March 2018. (in Japanese)

[67] C. Wang, K. Iokibe, and Y. Toyota, "Differential-skew mitigation by rotating meshed ground," in Proc. 2018 IEEE Int. Symp. Electromagn. Compat. and 2018 IEEE Asia-Pacific Symp. Electromagn. Compat., p.31, May 2018.

[68] C. Wang, K. Iokibe, and Y. Toyota, "Mitigation of differential skew by focusing on angle between differential lines and meshed ground,"IEICE Transactions (Japanese Edition) B, vol. J102-B, no. 3, pp.228-236, March 2019. (in Japanese)

[69] H. Takeda, K. Iokibe, Y. Toyota, “Crosstalk Reduction by Introducing Periodic Structure into Dense Differential Pairs,”Proc. 2017 IEEE Asia-Pacific Symp. Electromagn. Compat., p.353, 2017.

[70] H. Takeda, K. Iokibe, Y. Toyota, “Crosstalk Reduction by Introducing Periodic Structure into Differential Pairs,”IEICE Transactions (Japanese Edition) B,Vol.J101-B, No.3, pp.212-219, March 2018. (in Japanese)

[71] J. C. Isaacs and N. A. Strakhov, “Crosstalk in uniformly coupled lossy transmission lines,”Bell Syst. Tech. J., vol. 52, pp. 101-115, 1973.

[72] D. A. Hill, K. H. Cavcey, R. T. Johnk, “Crosstalk Between Microstrip Transmission Lines,”IEEE Trans. Electromag. Compat., vol. 36, no. 4, pp. 314-321, 1994.

[73] W. R. Eisenstadt, Microwave differential circuit design using mixed mode S-parameters. Artech House, 2006.

[74] J. He, C. Hwang, J. Pan, G. -Y. Cho, B. Bae, H. -B. Park, and J. Fan, “Extracting characteristic impedance of a transmission line referenced to a meshed ground plane,” in Proc. 2016 IEEE Int. Symp. Electromagn. Compat., pp.651-656, Sept. 2016.

[75] J. Cho, E. Song, H. Kim, S. Ahn, J. S. Pak, J. Kim, and J. Kim, “Mixed-mode ABCD parameters: Theory and application to signal integrity analysis of PCB-level differential interconnects,” IEEE Trans. Electromag. Compat., vol. 53, no. 3, pp.814-822, Aug. 2011.

[76] J. J. Wu, D. J. Hou, K. Liu, L. Shen, C. A. Tsai, C. J. Wu, D. Tsai, and T.-J. Yang, “Differential microstrip lines with reduced crosstalk and common mode effect based on spoof surface plasmon polaritons,”Optics Express Vol. 22, No.22, pp.26777-26787, Oct. 2014

[77] H. Takeda, K. Iokibe, Y. Toyota, “Crosstalk Reduction by Introducing Periodic Structure into Dense Differential Pairs,”Proc. 2017 IEEE Asia-Pacific Symp. Electromagn. Compat., p.353, 2017.

[78] H. Takeda, K. Iokibe, Y. Toyota, “Crosstalk Reduction by Introducing Periodic Structure into Differential Pairs,”IEICE Transactions (Japanese Edition) B,Vol.J101-B, No.3, pp.212-219, March 2018.

[79] J. C. Isaacs and N. A. Strakhov, “Crosstalk in uniformly coupled lossy transmission lines,”Bell Syst. Tech. J., vol. 52, pp. 101-115, 1973.

[80] D. A. Hill, K. H. Cavcey, and R. T. Johnk, “Crosstalk Between Microstrip Transmission Lines,”IEEE Trans. Electromag. Compat., vol. 36, no. 4, pp. 314-321, 1994

[81] A. Sugiura, and Y. Kami, "Generation and propagation of common mode currents in a balanced two-conductor line,"IEEE Trans. Electromagn. Compat., vol.54, no.2, pp.466-473, Apr. 2012.

[82] F. Grassi, L. Badini, G. Spadacini, and S. A. Pignari, "Crosstalk and mode conversion in adjacent differential lines,"IEEE Trans. Electromag. Compat., vol. 58, no. 3, pp. 877-886, 2016.

[83] F. Grassi, G. Spadacini, and S. A. Pignari, "The concept of weak imbalance and its role in the emissions and immunity of differential lines,"IEEE Trans. Electromagn. Compat., vol. 55, no. 6, pp. 1346-1349, Dec. 2013.

[84] C. R. Paul, "On the superposition of inductive and capacitive coupling in crosstalk prediction models,"IEEE Trans. Electromagn. Compat., vol. 24, no. 3, pp. 335-343, Aug. 1982.

Research Activities

Paper

1. **Chenyu Wang**, Kengo Iokibe, Yoshitaka Toyota, "Mitigation of differential skew by focusing on angle between differential lines and meshed ground," *IEICE Transactions (Japanese Edition) B*, vol. J102-B, no. 3, pp.228-236, March 2019. (in Japanese)

International Conferences

1. **Chenyu Wang**, Kengo Iokibe, Yoshitaka Toyota, "Design methodology of tightly coupled asymmetrically tapered bend for high-density mounting in differential transmission lines," *7th Asia-Pacific International Symposium on Electromagnetic Compatibility (APEMC 2016)*, pp. 463-465, Shenzhen, China, May 2016.

2. **Chenyu Wang**, Kengo Iokibe, Yoshitaka Toyota, "Optimum rotation angle for mitigating differential skew induced by glass cloth in PCBs," *2018 International Conference on Electronics Packaging and iMAPS All Asia Conference (ICEP-IAAC2018)*, pp. 328-332, Mie, Japan, Apr. 2018.

3. **Chenyu Wang**, Kengo Iokibe, Yoshitaka Toyota, "Differential-skew mitigation by rotating meshed ground," *2018 IEEE International Symposium on Electromagnetic Compatibility and 2018 IEEE Asia-Pacific Symposium on Electromagnetic Compatibility (EMC/APEMC)*, p. 31, Singapore, May 2018.

4. **Chenyu Wang**, Kengo Iokibe, Yoshitaka Toyota, "Reduction mechanism of differential-mode crosstalk between adjacent differential pairs with periodic structure," *2019 Joint International Symposium on Electromagnetic Compatibility and Asia-Pacific International Symposium on Electromagnetic Compatibility, Sapporo (EMC Sapporo & APEMC 2019))*, Sapporo, p. 786, Japan, Jun. 2019.

5. **Chenyu Wang**, Hiroaki Takeda, Kengo Iokibe, Yoshitaka Toyota, "Randomly shifted mesh position of meshed ground for high-density mounting in FPCs," *2019 IEEE International Symposium on Electromagnetic Compatibility, Signal and Power Integrity*, 1 page, New Orleans, LA, Jul. 2019.

Technical Report

1. **Chenyu Wang**, Kengo Iokibe, Yoshitaka Toyota, "Tightly coupled asymmetrically tapered bend in differential transmission lines for high-density mounting," *IEICE technical report*, vol. 115, no. 131, EMCJ2015-39, pp. 49-54, Jul. 2015. (in Japanese)

2. **Chenyu Wang**, Kengo Iokibe, Yoshitaka Toyota, "Evaluation of differential skew depending on rotation angle in printed circuit board with meshed ground plane," *IEICE technical report*, vol. 117, no. 510, EMCJ2017-109, pp. 25-30, March 2018. (in Japanese)

Others

1. **Chenyu Wang**, Kengo Iokibe, Yoshitaka Toyota, "Asymmetrically tapered bend for improving transmission characteristics in differential transmission lines," *JIEP Ultrahigh-speed and High-frequency Electronics Packaging Technical Meeting*, vol.15, no.3, pp. 1-6, Nov. 2015. (in Japanese)

2. **Chenyu Wang**, Kengo Iokibe, Yoshitaka Toyota, "Optimal rotation angle of glass cloth for mitigating differential skew induced by glass cloth in PCB," *JIEP Ultrahigh-speed and High-frequency Electronics Packaging Technical Meeting*, vol.17, no.3, pp. 17-20, Dec. 2017. (in Japanese)

3. **Chenyu Wang**, Hiroaki Takeda, Kengo Iokibe, Yoshitaka Toyota, "Reduction mechanism of differential-mode crosstalk between adjacent differential pairs with periodic structure," *The 2019 IEICE General Conference*, B-4-14, p. 234, March 2019. (in Japanese)

Biography

Chenyu Wang was born in Jilin, China, on March 6, 1987. He received an M.S degree in Electronic and Information Systems Engineering from Okayama University, Okayama, Japan, in 2017. He is now working toward a Ph.D. degree in Electronic and Information Systems Engineering. His research interest is electromagnetic compatibility (EMC) and signal integrity (SI) issues in the high-speed transmission system of printed circuit boards (PCBs). Mr. Wang is a member of the Institute of Electronics, Information and Communication Engineers.